2023

Towards a prototype paleo-detector for supernova neutrino and dark matter detection

Emilie Marie LaVoie-Ingram
University of North Florida, emiliemarie000@gmail.com

Towards a Prototype Paleo-Detector for Supernova Neutrino and Dark Matter Detection

Emilie LaVoie-Ingram

University of North Florida, 2023

Towards a Prototype Paleo-Detector for Supernova Neutrino and Dark Matter Detection

Emilie LaVoie-Ingram

B.S., Jacksonville University, 2021

A Thesis

Submitted in Partial Fulfillment of the

Requirements for the Degree of Master of Science

at the

University of North Florida

2023

APPROVAL PAGE

Master's Degree Thesis

Towards a Prototype Paleo-Detector for Supernova Neutrino and Dark Matter Detection

Presented by

Emilie LaVoie-Ingram, B.S.

Master's Advisor

Dr. Chris Kelso

Committee Member

Dr. Maitri Warusawithana

Committee Member

Dr. Jutima Simsiriwong

Committee Member

Dr. Brian Lane

University of North Florida

2023

ACKNOWLEDGEMENTS

Words cannot express my gratitude to my advisor and committee chair Dr. Chris Kelso, as well as my advisor Dr. Greg Wurtz, for their invaluable patience and feedback throughout graduate school. I also could not have undertaken this journey without the support and expertise of my defense committee: Dr. Brian Lane, Dr. Jutima Simsiriwong, and Dr. Maitri Warusawithana. This thesis research would not have been possible without the generous financial support from Dr. Chris Kelso. Additionally, this project was supported by the National Aeronautics & Space Administration through the University of Central Florida's NASA FLORIDA SPACE GRANT CONSORTIUM. I am also grateful to my research group members and cohort members, for their research help and moral support. Thanks should also go to all of the faculty and staff in the MSE program and physics department, who impacted and inspired me, and always offered to help when needed. Special thanks to my family for supporting me throughout my educational journeys, and raising me to be the strong person and student that I am. Lastly, I would be remiss in not mentioning my partner, Abby. Her belief in me has kept my spirits up and motivation high during this process and I truly could not have gotten through it without her. I would also like to thank my dog, Kai, and my cat, Denver, for all of the emotional support and entertainment.

TABLE OF CONTENTS

LIST OF FIGURES

LIST OF TABLES

Using ancient minerals as paleo-detectors is a proposed experimental technique expected to transform supernova neutrino and dark matter detection. In this technique, minerals are processed and closely analyzed for nanometer scale damage track remnants from nuclear recoils caused by supernova neutrinos and possibly dark matter. These damage tracks present the opportunity to directly detect and characterize the core-collapse supernova rate of the Milky Way Galaxy as well as the presence of dark matter. Current literature presents theoretical estimates for these potential tracks, however, there is little research investigating the experimental feasibility of this technique. At the University of North Florida, we have contributed to the field by searching for and analyzing these damage tracks in prototype detectors constructed from selected minerals, including: halite, Muscovite mica, and Phlogopite mica. This research seeks to characterize the applicable backgrounds in these prototype detectors. We have employed non-destructive techniques, including laser confocal and atomic force microscopy to identify and characterize damage tracks in the minerals. Chemical etching and plasma etching of target minerals is used to enhance the detectability of these damage tracks at the expense of altering some of their geometrical attributes. With the use of an etching rate model and automatic track detection via Python, damage track lengths will be reconstructed. Our data is compared to current theoretical predictions to pursue the practical implementation of paleo-detectors as local core-collapse supernova neutrino and dark matter detectors.

Chapter 1

Introduction

1.1 Paleo-Detectors

Paleo-detectors are an experimental technique with the potential to detect core collapse supernova (CC SN) neutrino and dark matter interactions with atomic nuclei in ancient minerals [5, 15, 16, 17, 18, 19, 20]. These minerals are analyzed for interactions in the form of nanometer scale line defects within the crystal lattice, called nuclear recoil damage tracks [5, 15, 16, 17, 18, 19, 20]. A damage track is created when an incoming particle collides with an atomic nucleus in the crystal lattice, causing that nucleus to recoil [5, 21]. The recoiling of the nucleus ionizes the lattice by displacing charges, and depending on the thermal, electric, and mechanical properties of the target mineral, damage tracks can be preserved for upwards of billions of years [5, 21]. Minerals capable of preserving these tracks are called Solid State Nuclear Track Detectors (SSNTDs) [22, 23, 24, 25].

SSNTDs are mostly used to search for fission and α-recoil tracks caused by radioactive decay. Damage tracks from radioactive decay originate when spontaneous fis-

sion in the target mineral causes an unstable heavy nucleus, most abundantly Uranium-238, to split into two daughter nuclides, which propel in opposite directions from one another in a random orientation in the crystal lattice [17, 21]. The propulsion of nuclides through the crystal results in a cylindrical defect with a radius of a few picometers [17, 21]. Similarly, α-recoil tracks originate when an α-particle is spontaneously emitted from an unstable nucleus, causing the same effects of ionization. Nuclear recoil tracks were first discovered in the 1950's when researchers exposed Muscovite mica to ions produced by the spontaneous fission of heavy elements via nuclear irradiation [26]. This discovery prompted extensive research into how these tracks form, what minerals they are formed in, and whether we can use the density of these tracks to date rocks [21, 26, 27, 28, 29, 30, 31]. As the field gained traction, scientists realized that any energetic heavy ion could produce these small crystal defects, including natural radioactive decay chains [26]. Researchers quickly found that fission track dating, and later α-recoil dating, of minerals is extremely accurate, and is still an active field of study [1] [26, 32, 33, 34]. The ideas and techniques within the fission track field initiated projects of different motivations, like searching for magnetic monopoles, cosmic ray interactions in ancient mica, and neutron dosimetry [23, 31, 35, 36]. Most studies focused on detecting tracks other than fission and alpha-recoil tracks initiated between 1960-1990 often ended due to poor resolution of readout technologies or inadequate etching techniques [23, 31, 35, 36]. As the motivations laid dormant for a few decades,

[1] Fission track and α-recoil track dating will be further discussed in Section 3.3.2.

the evolution of technology and new scientific ideas have prompted study into the upcoming paleo-detector technique.

Like spontaneous radioactive decay, SN neutrinos and dark matter can also induce damage tracks in ancient minerals. These particles can interact with an atomic nuclei present in the crystal lattice, causing a nuclear recoil of a similar energy range to that of the radioactive decay resulting in similar damage track geometries. The length of the damage track is dependent on the energy of the collision. The incoming SN neutrinos and dark matter particles have a spectrum of energies rather than a single energy typical of radioactive decay [5, 15, 16, 17, 18, 19, 20]. So rather than searching for damage tracks of a specific length, we are searching for a predicted spectrum of track lengths. Current literature presents theoretical estimates for CC SNe and dark matter nuclear recoil detection, but to date there is little research investigating the experimental feasibility of this technique. However, over the last couple of years, research groups around the world have initiated, or are planning to initiate, projects using the paleo-detector technique, with a variety of minerals and readout technologies [17].

The goal of these studies, much like ours, is to establish and develop readout techniques to detect the damage tracks induced by nuclear recoils of all backgrounds [17]. A team at the SLAC National Accelerator Laboratory (SLAC) recently became interested in using ancient minerals for dark matter and neutrino detection, specifically using the readout technologies of electron beam tomography, coherent X-ray imaging, and atomic force microscopy [17]. So far the team is still exploring the sensitivity and

potential of these techniques by irradiating Muscovite mica and Silicon, and chemically etching to reveal tracks before using the various readout technologies [17]. At the Japan Agency for Marine-Earth Science and Technology (JAMSTEC), a team is aimed at detecting nuclear recoil damage tracks with electron microscopy, as an alternative to the proposed helium ion microscopy readout method by Refs. [5, 16] [17]. In addition, the researchers are using atomic force microscopy to detect damage tracks in neutron irradiated Muscovite mica etched with Hydrofluoric Acid (HF), using the pathway set decades ago by References [36, 37] [17]. At Toho and Nagoya University, a group is working with a nano imaging tracker, which is capable of detecting nanometric scale tracks from dark matter-induced nuclear recoils [17]. The tracks are measured with an optical-based system and have been successful at detecting fission tracks and α-recoil tracks in Muscovite mica [17]. At the Karlsruhe Institute of Technology and Heidelberg University, a joint project is focused on detecting nuclear recoil damage tracks present in salt minerals, using etching and optical microscopy [17]. The research group has access to a wide variety of nanoscale readout technologies, and once data is collected it will be compared to theoretical simulations [17]. At Queen's University of Kingston Ontario, a team is analyzing samples of irradiated olivine and galena, which will be readout using High-Resolution Transmission Electron Microscopy (HRTEM) [17]. There is also a research group called PALEOCCENE, that is comprised of around 20 scientists at 7 different institutions, that is focused on detecting low energy nuclear recoils with color center [17]. Color centers allow for optical readout with fluorescence

microscopy and selective plane illumination microscopy, and the group is currently focused on gamma radiated CaF_2 crystals [17]. Finally, in Maryland, a team of scientists are searching for dark matter signals in geological quartz and diamond, using super-resolution Nitrogen-Vacancy strain spectroscopy and scanning X-ray diffraction microscopy [17].

All of these current and potential research projects demonstrate the capability of the paleo-detector technique and the wide range of methodology used to try to detect neutrino- and dark matter-induced tracks. Our current research seeks to set a foundation for future experimental paleo-detector studies, focusing on identifying and characterizing tracks, comparing against theoretical studies, and determining the relevance of our chosen methodology going forward.

1.1.1 Galactic Supernova Neutrino Detection

Supernovae are important research topics in astrophysics and cosmology that can lead to a greater understanding of galaxy and local star formation rates. Only a few SNe have been observed in the local group, a collection of about 40 galaxies - including our own - that span nearly 100 million light years in diameter [6, 13, 38, 39]. Although we have observed many extragalactic SNe, allowing for what we call a *cosmic SN rate* to be observed, there is no direct measurement of the Milky Way SN rate [5, 15, 16, 17, 18, 19, 20]. Recently, paleo-detectors have been a proposed method of detecting neutrino-induced nuclear recoils from core collapse (CC) SNe within our

galaxy [5, 15, 16, 17, 18, 19, 20]. Supernovae are an abundant source of neutrinos, and by using paleo-detectors we can search for remnants of nuclear recoils caused by these bursts of neutrinos [5, 15, 16, 17, 18, 19, 20]. Detecting tracks induced by local CC SNe can both constrain the CC SNe rate that current literature suggests to be around a few SNe per century [38, 39, 40], and also potentially detect a starburst period in the Milky Way within the time frame of mineral preservation ($\sim$ 1 Gyr) [5, 15, 16, 17, 18, 19, 20]. Close by SNe have also been linked to mass extinction events, contributing another motivation behind the search for the Milky Way's SNe rate [5, 15, 16, 17, 18, 19, 20].

1.1.2 Weakly Interacting Massive Particle Dark Matter Detection

Nearly a century after the gravitational evidence of dark matter came to light, it still remains one of the biggest mysteries of our universe [41]. Weakly Interacting Massive Particles (WIMPs) are one of the leading theories of the dark matter particle, and decades worth of challenging direct detection research has gone into searching for the existence of the dark matter WIMP [5, 15, 16, 17, 18, 19, 20]. Paleo-detectors are a potential alternative technique to these experiments. Instead of attempting to detect nuclear recoils in real time like liquid noble gas experiments and cryogenic bolometric detectors, we can search for nuclear recoil traces in minerals over millions of years [5, 15, 16, 17, 18, 19, 20]. The detection of WIMP-induced nuclear recoils would establish the particle nature of dark matter, resulting in a confirmation of our current understanding of the structure of the universe. While the origin of a single damage

track cannot be identified in most cases, statistical statements about the population and spectra of damage tracks can be used characterize backgrounds, and possibly any dark matter induced signals above all backgrounds (including those caused by local CC SNe) in the mineral.

1.2 Backgrounds

Damage tracks caused by CC SNe neutrinos and dark matter can theoretically be measured after proper materials processing. However, remnants from CC SN neutrinos and dark matter interactions are not the only kinds of damage tracks left in these ancient minerals. There are a number of phenomena other than CC SNe neutrinos and dark matter that can produce damage tracks in target minerals. These background tracks from different sources must be characterized and are typically indistinguishable from one another with the exception of a few characteristics [24]. Natural defects present in the crystals do not resemble damage tracks induced by neutrinos or dark matter and thus their contribution will be negligible[2] [5].

The backgrounds in paleo-detectors are similar to backgrounds in current day direct detection experiments, yet vary in importance due to the exposure time, observable track lengths, and exposure time integration [19]. Paleo-detectors use long exposure times ($\leq \mathcal{O}(10^9)$ yr) and small target masses ($\leq \mathcal{O}(1)$ kg), whereas conventional di-

[2] Additional information regarding differentiating natural crystal defects from tracks with be discussed in the Results section.

rection detection experiments use short exposure times ($\leq O(10)$ yr) and large target masses ($\leq O(10^4)$ kg) [19]. In addition, in paleo-detectors the observables are track lengths between 1-500 nanometers, whereas in direction detection experiments one would observe the ionization charge, scintillation light, or the heat (phonons) produced by the nuclear recoil interaction [19]. Lastly, paleo-detectors measure recoils integrated over a large time period, without specific knowledge of when a recoil happened (to a certain precision), whereas direction detection experiments have very precise timing information as it captures a recoil as it happens [19].

1.2.1 Radioactive Decay

Natural minerals are often contaminated with small amounts of radioactive elements, which as they decay will give rise to damage tracks within the length of relevance for paleo-detector research [5, 16, 42]. Minerals formed in Earth's crust near the surface typically have a large uranium-238 (^{238}U) and thorium-232 concentration, but the most relevant radioactive influence is uranium [5, 16, 42]. The damage tracks from the individual β-, γ-, and α-decays are not observable, however the daughter nuclei recoils from the α-decays have energies between 10 - 100 KeV, which give rise to tracks similar to those induced by CC SNe neutrinos [5, 16, 42]. The typical decays of ^{238}U lead to a complete decay chain consisting of eight α-decays, that produced eight observable daughter nuclei recoils. Theoretically these observable decay tracks will lead to a kind of spatial connectedness that is distinguishable, however this can be dependent on

uranium concentration, sample size, track orientation, and etching conditions [5]. Although α-recoil tracks will be produced throughout the decay chain of ^{238}U into stable lead (Pb), the first decay chain (^{238}U$\rightarrow^{234}$Th $+\alpha$) will produce a non-negligible background of events at a specific energy of 72 keV (corresponding to a specific track length depending on the target mineral) [5, 16, 42]. In addition to α-recoil tracks, larger tracks produced by the spontaneous fission of unstable uranium into barium and krypton will also be within our measurable range.

1.2.2 Neutron Induced Backgrounds

Fast radiogenic neutrons can present damage tracks within the observable, relevant track length range [5, 42]. The dominate sources are produced by ^{238}U decay and (α, n)-reactions of α-particles. Reference [5] provides open source code mapping the neutron spectrum from both sources, using a program called JANIS [43]. JANIS is a computer software developed to manipulate and visualize nuclear data [43]. The fast neutrons present in target minerals will lose most of their energy due to the scattering from nuclei, and thus this background will vary significantly based on the chemical composition of the mineral. For minerals containing hydrogen, this background is significantly reduced as a hydrogen nuclei has approximately the same mass as a neutron, and thus in the elastic collision the fast neutron will lose most of its energy [5]. This makes hydrogen an efficient moderator of fast neutrons [5].

1.2.3 Cosmic Ray Induced Backgrounds

Fast neutrons can also arise from cosmic ray muons interacting with nuclei near or in the target mineral [5, 42]. The neutron flux caused by the cosmic ray background significantly varies with the depth of mineral extraction, from $\phi_n = O(100)cm^{-2}Gyr^{-1}$ at 5 km deep to $\phi_n = O(10)cm^{-2}Gyr^{-1}$ for 7 km deep [5]. For minerals obtained from depths larger than approximately 6 km, this specific background will be negligible [5]. Cosmic rays themselves can also give rise to direct damage tracks in minerals [5, 35]. These tracks are not caused by a recoiling nucleus, instead a charged particle penetrates the crystal and ionizes the lattice across a large length, sometimes reaching tens of centimeters, and follows a symmetric path unique to the crystal structure of the target mineral [35]. These direct tracks are easy to distinguish from nuclear recoil tracks due to their length, symmetry, and connectedness. In addition to fast neutrons, cosmic muon decay chains emit neutrinos, affecting the neutrino-induced background [5].

1.2.4 Neutrino Induced Backgrounds

Neutrinos produced by our Sun give rise to nuclear recoils creating the potential for background signals [5, 42]. Neutrinos are also produced in both primary and secondary collisions of cosmic rays with our atmosphere. These are referred to as atmospheric neutrinos, and nuclear recoils induced by atmospheric neutrinos will produce a background of damage tracks in the relevant energy range for our study. The sum total of all neutrinos produced in supernovae over the entire history of the Universe also presents

another background for our search. This specific contribution is called the Diffuse SN Neutrino Background (DSNB), and the relevant track lengths induced by this background vary per specific mineral because of differences in nuclei mass and is presented in Ref. [5, 42].

1.2.5 Background Uncertainties

In addition to background signals present in these minerals, the unknown thermal and sometimes geographical past of the mineral can present ambiguity in research. Depending on the characteristics of the target mineral, and the incoming particle's charge, mass, and energy, nuclear recoil damage can appear as a variety of forms, including mechanical stress in the crystal lattice, electron density fluctuations, local amorphization, and vacancy defects [17]. These crystal defects, as well as the nanometer-scale damage tracks we are interested in detecting, can be erased in a process of re-crystallization called "self-annealing" [17]. In the case of SSNTDs, these crystal defects are preserved in the lattice due to the specific chemical composition and temperature of the target crystal, allowing the self-annealing process to take timescales on the order of millions to billions of years [17]. Knowing the geological and geothermal history of the mineral is helpful in mapping theoretical track length spectra for background signals, but not necessary.

Chapter 2

Mineral Optimization

Although backgrounds can make paleo-detector research very difficult, the physical source of these backgrounds leads to certain minerals presenting more favorable properties as paleo-detectors. SSNTD minerals capable of being paleo-detector materials are constrained by a few boundary conditions induced by the applicable backgrounds. One of the largest sources of backgrounds is radioactive decay of uranium-238 (^{238}U) [5, 15, 16, 42]. To suppress this background, it is essential to use minerals with as little ^{238}U concentration as possible. We can estimate the concentration of ^{238}U in Earth's crust to be on the order of parts per million (ppm), which is unfortunately too high of contamination to be used in this study [5]. However, rocks found in Earth's mantle and seawater, like ultra-basic rocks (UBRs) and marine evaporates (MEs), have much lower concentrations of ^{238}U, and are estimated in prior theoretical studies to be around 0.01 parts per billion (ppb) [5, 15, 16, 42]. Neutron-induced backgrounds can reduced by using minerals containing hydrogen, as hydrogen has proved to be an effective suppressant of fast neutrons since the neutrons lose a significant portion of collision energy due to similarity in mass [5, 15, 16, 42]. The effect of fast neutrons induced by muon decay

can be reduced by mining minerals deep enough in Earth's crust, ideally greater than 6 km [5, 15, 16, 42]. Choosing minerals with heavy target nuclei are most applicable for visibility of tracks due to WIMPs with masses greater than 10 GeV; however for low-mass WIMPs, the lighter the nuclei, the greater the damage track length and thus, the better visibility [5, 15, 16, 42]. Nuclei with large nuclear spin provide the best chance for detecting dark matter if the primary interaction is spin-dependent. For CC SNe detection, target nuclei with masses between C and Si provide a balance between detectable damage track lengths and lengths different enough from backgrounds induced by solar neutrinos [5, 15, 16, 42]. As discussed in the previous section, ME minerals also have the potential of re-crystallizing, which due to the increase of plasticity in the mineral, can erase previously recorded tracks [5]. This could be good for suppressing backgrounds, but this process can also erase tracks from CC SNe neutrinos and dark matter.

There are several minerals used as particle detectors in a variety of scientific fields. Recently, there have been additional minerals proposed to be paleo-detectors, including but not limited to nchwaningite [$Mn_2\ SiO_3\ (OH_2)\ H_2O$], halite [Na Cl], epsomite [$Mg\ SO_4\ 7\ (H_2O)$], and olivine [$(Me, Fe)_2\ SiO_4$] [5, 15, 16, 17, 42]. All of these minerals have been chosen because they can be found in marine evaporates and ultra basic rocks. We followed the guidance of these theoretical studies, and additionally literature already present for related fields, when determining what minerals to use as track detectors. However, for the sake of time and cost, less consideration was placed

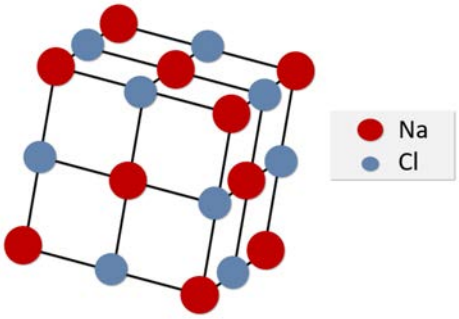

Fig. 2.1: Crystal structure of halite (NaCl) [1].

on the specific age and geographical location of these minerals and more so on obtaining enough mineral to conduct an accurate chemical and kinetic etching study.

2.1 Halite

The first mineral we experimented with is a marine evaporate: halite, or ”rock salt”. Halite crystallizes in a face centered cubic crystal lattice (space group Fm3m), with a lattice constant of $a = 0.564$ nm (Fig. 2.1) [1]. Cubic cleavage is observed in halite, where the crystal will break into smaller cubic pieces. One can cleave halite with a rock hammer. Our sample of halite was extracted in Ontario, Canada. It is unknown what specific mine supplied the sample, however, is it likely it came from the Sifto Salt Mine (Goderich Mine), in Goderich, Huron County, Ontario, Canada - the largest salt mine in the world [44, 45]. This mine is located nearly 2,000 feet under Lake Huron [45].

Halite was theoretically proposed as a track detector because it can be found in marine evaporate deposits and thus has significantly less radioactive decay than miner-

als traditionally found in Earth's crust [5, 15, 16, 17]. Halite formed from evaporated seawater, leading to relatively low concentrations of radioactive isotopes (0.01 ppb), which can in turn suppress the radiogenic neutron background in the target mineral [17]. There are a couple of new experiments using halite as a paleo-detector target mineral (discussed in Section 1.1), but overall the literature on using halite as a track detector is relatively limited. We hope to take this unique opportunity to characterize and report on the effectiveness of halite as a nuclear recoil track detector.

2.2 Muscovite Mica

Another mineral of focus in this research is Muscovite mica [$KAl_2\ AlSi_3\ O_{10}\ (OH)_2$]. Muscovite mica crystallizes in a dioctahedral, monoclinic structure, with lattice parameters of $a = 0.533$ nm, $b = 0.923$ nm, and $c = 1.022$ nm (Fig. 2.2) [2, 46]. Mica is a 2-D material, and is made up of tetrahedral-octahedral-tetrahedral (T-O-T) layers [2]. The perfect basal cleavage is due to the weak interlayer potassium bonds, present in all types of mica (Fig. 2.2). These interlayer bonds are dominated by van der Waals and Coulomb forces, and the theoretical bond energies of layered materials like mica can be studied using Density Functional Theory [47]. Reference [47] calculated the theoretical interlayer bonding energies of Muscovite to be between -0.48 and $-0.25\ J/m^2$, which is similar to graphite [48]. We can use the same methods to cleave mica that one would use to cleave graphite - with a razor blade or scotch tape [46]. The Muscovite mica obtained for this research came from the Asheville Mica Company, in Newport

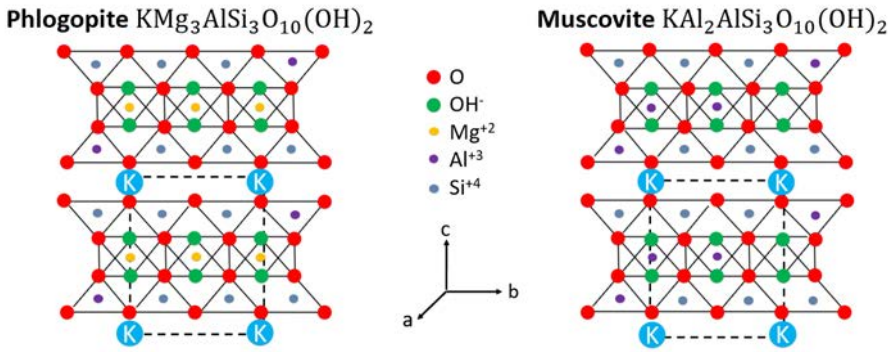

Fig. 2.2: Monoclinic, layered crystal structures of Muscovite mica and Phlogopite mica (unit cell outlined in dotted lines) [2, 3].

News, VA. The mica was confirmed to be fully natural, with no thermal, mechanical, or chemical processing before shipping. The mica was mined between depths of 250 - 1000 feet underground. We have experimented with both crude mica and block mica. Crude mica is mica exactly as it is extracted from the mine, whereas block mica has been sorted and graded based on the quality and cleanliness of mica samples. Crude mica often has many inclusions of heavy elements present, mainly iron oxides, like magnetite [Fe_3O_4], and hematite[Fe_2O_3] [49]. Fig. 2.3 displays images of our crude Muscovite mica samples, containing what looks to be black magnetite or rutile [TiO_2] inclusions, and red hematite inclusions.

As one of the most widely used SSNTDs, Muscovite mica is notably one of the most suitable mineral detectors due to it's atmospheric stability, perfect basal cleavage, transmissive sheets, and - potentially - low concentrations of U and Th on the order of ppb [17]. Micas are considered ultra basic rocks, and thus the uranium content

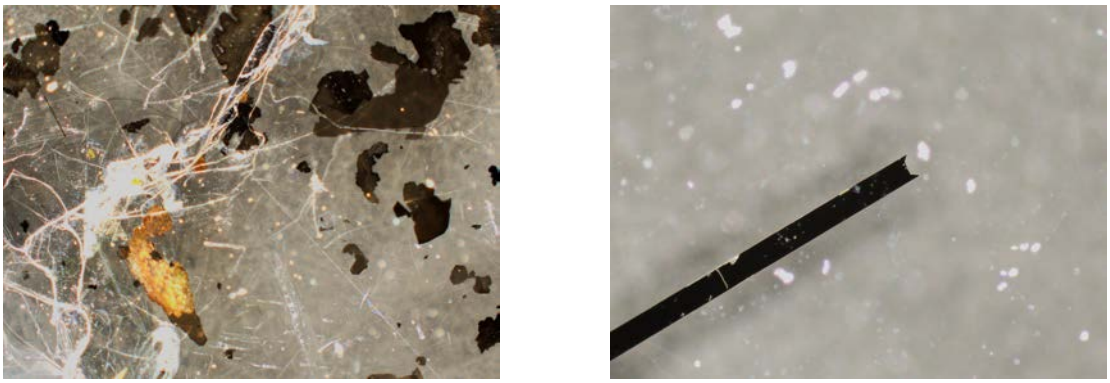

(a) **(b)**

Fig. 2.3: Optical image of crude Muscovite mica with (a) hematite, rutile, and/or magnetite inclusions, and (b) a sharp, rectangular inclusion of magnetite following the crystal planes. Imaged with the Keyence VK-X1000 laser confocal microscope at MSERF.

estimated for this research is based on an estimate of 0.01 ppb from Ref. [5]. Muscovite mica was chosen for our research due to these qualities but also due to it's exhaustive history as a fission track detector. Fission tracks were first discovered in Muscovite mica, and since this discovery, copious amounts of experiments have been performed with the mineral. The immense amount of literature present for Muscovite mica as a mineral detector allows for a more accurate analysis into background signals, feasible etching techniques and readout technologies.

2.3 Phlogopite Mica

Similar to Muscovite in quality and feasibility as a mineral track detector is a type of dark mica called Phlogopite [$KMg_3\ AlSi_3\ O_{10}\ (OH)_2$]. Phlogopite also crystallizes in monoclinic form, but it is trioctahedral, in T-O-T layers, with lattice parameters of $a = 0.531$ nm, $b = 0.919$ nm, and $c = 1.015$ nm (Fig. 2.2) [3]. The mineral's interlayer potassium bonds allow perfect basal cleavage, like Muscovite. It is less transmissive than Muscovite, thus why it is referred to as "dark mica". Reference [47] calculated the theoretical interlayer bonding energies of Phlogopite to be between -0.43 and -0.23 J/m^2. Phlogopite can be cleaved in the same method as Muscovite, with a razor blade or scotch tape. We obtained our samples of Phlogopite from the same mine that provided us Muscovite mica, and we assume the same radioactive content present as Muscovite mica.

Phlogopite has been theoretically studied as a track detector by Refs. [5, 15, 16, 17, 42]. Similar to Muscovite mica, Phlogopite mica has a history as an, α-recoil and fission track detector [30, 50, 51, 52, 53]. The most important difference between Phlogopite mica and Muscovite mica is hydrogen content, and furthermore the influence that hydrogen content has on the neutron background present in target minerals (see Section 1.2.2). Phlogopite mica has 0.22 % more hydrogen per weight than Muscovite mica. Although this percentage is small, this can still have a significant effect on the neutron background present in ancient minerals. Muscovite theoretically will suppress this background more because of the increased hydrogen content, and we see this

reflected in experimental studies comparing Muscovite and Phlogopite mica as track detectors [30, 50]. Phlogopite mica on average has a higher density of nuclear recoil damage tracks present, and if using optical microscopy, will be easier to find across the mineral [30]. Our samples of Phlogopite are relatively new, and is the mineral least experimented on throughout this research. Part of the future work of this project could entail an in-depth comparison between Muscovite and Phlogopite as paleo-detector minerals, and testing past experiments reporting track density differences between the two kinds of mica. The difference in transparency between Phlogopite and Muscovite will also impact their optical properties while imaging. Based on initial observations with a standard reflected light microscope and with a laser confocal microscope, it is suggested that Phlogopite has a much higher rate of scattering off the surface due to its gold-like color and higher density of surface defects like air pockets, flakes, and water trapped under the topmost layers of the sheet. An image of one of our Phlogopite samples alongside a sample of Muscovite is shown in Fig. 2.4.

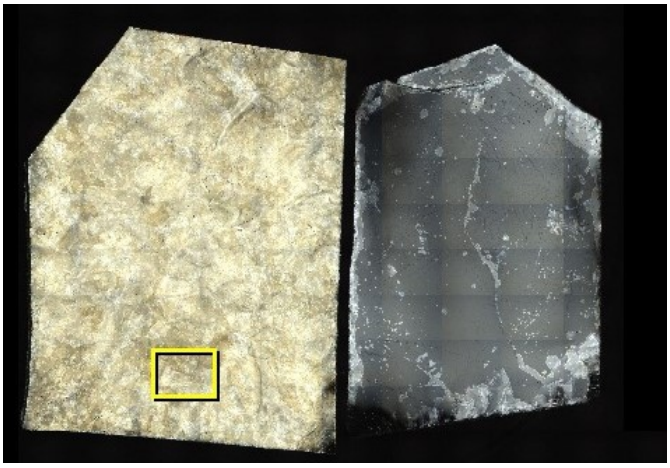

Fig. 2.4: Optical image of (left) Phlogopite mica and (right) Muscovite mica, taken with the Keyence VK-X1000 laser confocal microscope at MSERF.

Chapter 3

Methodology

Perhaps the most important step in this research is the identification of damage tracks. There are multiple steps to reveal, measure, and reconstruct tracks before any analysis into track origin can begin.

3.1 Revealing Tracks

To access the randomly oriented, nanometer-scale tracks, one must cleave the target crystal first, taking into account of the directionality of the cleave and the type of cleavage. Nuclear recoil damage tracks are often not observable to us with ordinary microscopic techniques due to the sub-nanometer diameter of the cylindrical tracks. To reveal these tracks after cleaving, various etching techniques can be used.

3.1.1 Chemical Etching

In nuclear recoil damage track studies, and many other scientific fields, chemical etching is often used to enhance the size of surface defects on crystals (tracks), going from an order of nanometers to an order of micrometers, which is visible optically. Chem-

ical etching of halite can be done in a solution of ferric chloride ($FeCl_3^+$) and glacial acetic acid (CH_3COOH), briefly, for a few seconds [54]. NaCl and $FeCl_3^+$ react to form $NaCl_2^-$ and $FeCl_2^+$ and thus the ions in halite will preferentially want to dissolve into the ferric chloride and glacial acetic acid mixture [54]. Halite is water soluble, so it is important that the mineral samples are kept clear of humid conditions and contact with water. Samples can be cleaned in pure isopropanol.

The conventional technique to reveal tracks in Muscovite mica is by etching in a concentrated solution of hydrofluoric acid [14]. Although an effective etchant, hydrofluoric acid is an incredibly dangerous acid, and thus for our research we chose to test an alternative route that has been studied: aqueous solutions of sodium hydroxide (NaOH) [25, 55, 56]. Micas, being made up of primarily SiO_2 and Al_2O_3, will slowly dissolve in caustic (sodium hydroxide) solution in the form of silicate and aluminate ions [57]. The solution will try to reach equilibrium with the mineral, depending on the concentrations of silicate and aluminate to balance the concentration of NaOH in aqueous solution [57]. This equilibrium will highly depend on the pH, temperature, and composition of the solution [57]. Samples can further by cleaned with deionized water in an ultrasonic bath, or with isopropanol, for a few seconds. Phlogopite was not etched chemically as part of this research, however the mineral can usually be etched with the same chemicals as Muscovite under different temperature and/or etching time.

3.1.2 Plasma Etching

In addition to chemical etching, we can also kinetically etch minerals with Argon plasma. Plasma etching can be done one of three ways: isotropic plasma etching, anisotropic sputtering, and reactive ion etching. Plasma etching can be an alternative technique to chemical etching, providing a clean, fast, controllable method of etching that rarely affects the bulk properties of the substrate (at the right etching conditions) [14]. The plasma etching of SSNTDs has, to our knowledge, only been done once (Muscovite mica - Reference [14]) and is lightly studied. The application of plasma etching with our micas and halite samples would be one of the first of its kind, and we report on the effectiveness of the technique moving forward.

In a plasma etching or cleaning system, a radio-frequency (RF) voltage is applied to two parallel plate electrodes in a vacuum chamber that will then emit a discharge current flow [58]. Plasma can be induced when this RF discharge ionizes the gas in the chamber, causing the gas to become a partially ionized state made up of equal parts electrons and positive ions and will emit a characteristic glow [58]. The glow from argon plasma induced in our experiments can be seen in Figure 3.1. The ionized gas particles will incessantly collide with one another and the substrate surface present in the chamber [58]. The kinetically-driven plasma etching process induces both elastic and inelastic collisions. Elastic collisions involve only the transfer of energy, but inelastic collisions can annihilate and create particles within the plasma gas [58]. In ionized gas, there exists four main types of particles: electrons, non-excited or excited atoms,

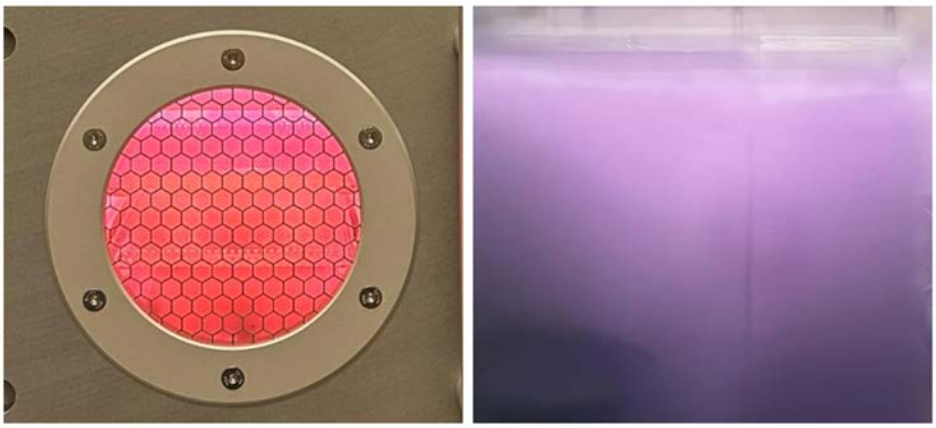

Fig. 3.1: Characteristic glow emitting from argon plasma, at a power of (left) 100 Watts in the Diener Pico plasma cleaner and (right) 20 W in the Lesker ProLine sputter system.

diatomic or polyatomic molecules, and positive atomic or molecular ions [58]. In a plasma cleaning system, the cleaning or etching is isotropic (neglecting effects due to the substrate properties). It essentially bathes the substrate in plasma, with no induced directionality. In a reactive ion etcher or sputter system, however, there is a bias voltage applied to the ions, driving them at a certain angle to the substrate surface [58]. In addition, reactive ion etching also uses a chemically reactive plasma, inducing both kinetic (plasma) etching and chemical etching on the substrate [58]. In the case of applied bias voltage, one could manipulate the etching rates and properties.

Isotropic plasma etching, the main method of kinetic etching in this research, was done with the Diener Pico plasma cleaner in Lab 50/1522. The Diener Pico system reaches a maximum power of 100 Watts, and usually operates at a pressure of approx-

imately 0.2 mbar. It ionizes either pure argon, oxygen, or CF_4 gas using a 13.56 MHz radio-frequency discharge. In our experiments only argon plasma was used, following previous literature [14]. Supplementary experiments were also done with the Lesker ProLine PVD75 sputter system, and the Trion Sirus T2 reactive ion etcher (also in Lab 50/1522), but these methods of plasma etching were not considered applicable to us at this stage. However, future work of this project should test the capability of these two systems and the effectiveness on etching our paleo-detector target minerals. More information about our standard operating procedure for the Diener Pico plasma cleaner can be found in Appendix Section A.

3.2 Measuring Tracks

The damage track readout method depends on the electrical, optical, and surface properties of the target material. The detection and measurement of nuclear recoil damage in crystals has been demonstrated with a wide variety of microscopic techniques, including transmission electron microscopy (TEM), scanning electron microscopy (SEM), atomic force microscopy (AFM), X-ray microscopy, laser confocal microscopy, and optical microscopy [17]. Here at the University of North Florida, we have tested a few of these techniques and determined the feasibility of them going forward.

3.2.1 Laser Confocal Microscopy

The readout tool of focus in this research is the Keyence VK-X1000 laser confocal microscope (LCM), located at the Materials Science and Engineering Research Facility (MSERF) here at UNF. The LCM was chosen for its high resolution and high throughput, and ability to map three-dimensional height information across sample surfaces. With the LCM, one can image $\sim 7.3 \times 10^3$ μm^2 in a matter of seconds. Optical microscopy has been the primary readout method in fission track studies over the last few decades. In the past, however, the capability of this technique has been limited due to the lack of three-dimensional (height) data. One could only measure the track length captured on the surface of the cleave with traditional reflected light microscope. With transmitted light microscopes, one could gain information about the total track length and angle, because along with seeing the track captured on the cleave surface one can also see the tracks confined in the mineral (Fig. 3.2). Both of these optical methods still require the mineral to be etched beforehand, as the resolution is typically on the order of hundreds of nanometers and thus the microscopes are not capable of detecting most unetched tracks.

All imaged tracks in this research were identified and measured with the LCM. In addition to the microscope itself, Keyence also provides a software, Multi-File Analyzer, that allows users to manipulate, plot, and process the raw data output files from the Keyence. This software was frequently used as part of the data and image processing of this research. More information about the operation, use, and resolution of the

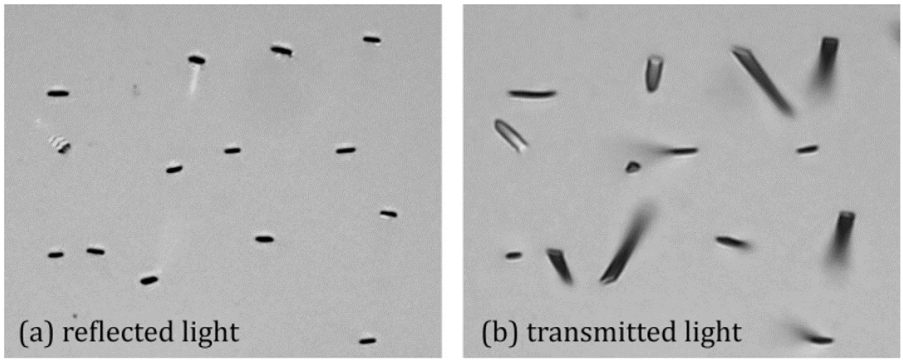

Fig. 3.2: Images showing the same sample surface of etched apatite, and how track imaging changes with (a) reflected and (b) transmitted light microscopes, from Reference [4].

Keyence VK-X1000 laser confocal microscope can be found in Appendix Section A.5.

3.2.2 Atomic Force Microscopy

Atomic Force Microscopy (AFM) is a powerful tool with with nanometer-scale resolution and wide applications in materials characterization. An AFM uses a vibrating probe to explore surface topography, using the interaction forces (primarily van der Waals) between the probe tip and sample surfaces to map three-dimensional data [9]. Atomic force microscopy has an extensive history of being a track readout technology. As a contrary to optical microscopes, the AFM is commonly used to measured tracks due to its superior nanometer scale resolution [17, 36, 37]. Many of the first experiments exploring nuclear recoils tracks much smaller than ^{238}U fission tracks were inspired by the promising resolution of the AFM. However, AFM is low throughput,

and extremely sensitive to surface roughness. Imaging a fraction of a sample 1 cm^2 in size would take many hours, whereas a LCM can image within minutes. The use of AFM in this research is also limited due to the roughness of our chemically and kinetically etched samples. We present AFM as a way to sensitively characterize unetched surfaces of minerals, and in some select cases, etched surfaces. We use ”tapping” AFM (AM-AFM) to image the surfaces of our samples. In addition to the AFM, software compatible with raw AFM output files were used to visualize, plot, and process data, specifically WSxM [59] and Gwyddion [60]. More information about how an AFM works and our standard operating procedure can be found in Appendix Section A.

3.2.3 Additional Methods and Limitations

Aspirations for the future of paleo-detector research often entails using readout technologies that are efficient for larger samples sizes and involve reading bulk volumes of crystal without the need for etching. This process would preserve the exact length of tracks and ideally would not be dependent on track orientation (which is a limitation of chemical etching). References [5, 15, 16, 17, 18, 19, 20] proposed two additional methods that could be used to measure tracks in paleo-detector minerals: small angle x-ray scattering (SAXs) and helium ion beam microscopy (HIM). SAXs tomography, specifically at synchrotron source facilities, would potentially allow a three-dimensional readout of samples with a spatial resolution down to approximately $\sigma_x \sim 15$ nm and would require minimal sample preparation [5]. It is unknown at this point whether it is pos-

sible to reconstruct damage tracks from ions using this technology, but damage tracks have been *observed* using SAXs along the direction of the track [5, 61]. Future work of paleo-detector studies will hopefully include testing the limits of SAXs and discovering a high throughput readout methodology that would allow for a straightforward reconstruction of unetched track lengths. HIM is another proposed method that would have similar resolution to electron microscopy [19]. Electron microscopy (EM) was not used in this study because of the insulating properties of our mineral detectors. We would need to cut a very thin (tens of microns) sample or coat with a conductive layer, both of which are likely to damage sample surfaces and/or completely erase the nuclear recoil tracks. HIM however could be an alternative method that would cause less sample damage than EM and is capable of subsurface imaging to depths of hundreds of nanometers [19].

With two-dimensional readout methods such as AFM, LCM, and EM, the use of a focused ion beam of either neon or gallium ions could be used for sample preparation methods [19]. Sample surfaces can first be imaged with a high-resolution readout technology, then using a FIB, one could sputter away layer after layer of material, creating a piece-wise volumetric readout of track density [19]. However, this could prove difficult with insulating samples due to charge build up.

As paleo-detector studies increasingly become a field of focus, the sensitivity and success of readout methods will be better understood. The first step in this process of determination, and what we and other researchers around the world have studied and

planned to study, is the effectiveness of the well known etching and optical readout technique used in fission track studies. Using a well-studied method would allow us to first see if detecting tracks among many different signals is even possible in our target minerals. Characterizing and fully understanding our target minerals and the influence of track background and track formation in the mineral, is an important part of the research that will preface high throughput, powerful readout methods of track detection.

3.3 Track Reconstruction

Automatic Track Detection in Python

Once tracks have been imaged, track lengths must then be accurately measured. These track lengths can be reconstructed using a variety of computational techniques. To reduce the time spent detecting, measuring, and reconstructing the immense amount of data collected during these experiments, we have developed an automatic etch pit detection and measurement code in Python (this script can be found on GitHub). This code was used to automatically detect tracks present in images, and use the height information to calculate track dimensions. The user-given data for the code includes a black and white laser image, a .csv file containing the height information per pixel, and the magnification of the image. All images and height information can be exported directly from the Keyence VK-X1000 Multi-File Analysis software. Before the height information was measured, a plane subtraction using two-dimensional linear regression

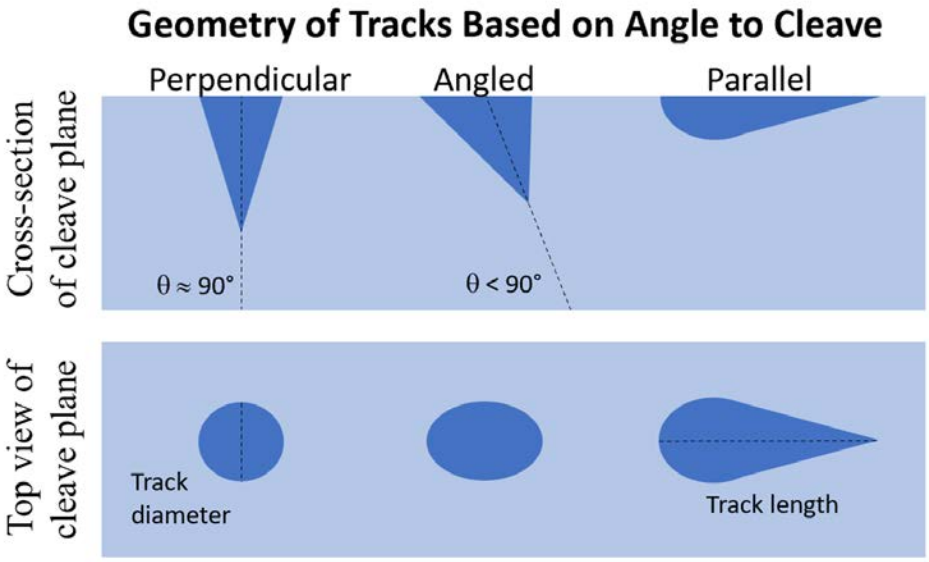

Fig. 3.3: Diagram showing how geometry of a track etch pit will vary depending on the angle of the track to the cleave plane of a mineral.

was applied to the data. This regression removes any tilt from the height information due to an uneven sample or sample stage, and allows for a more accurate detection of etch pit depth.

The backbone of the automatic etch pit detection code runs on the OpenCV package for Python, specifically the SimpleBlobDetector function [62]. A blob is a clump of connected pixels in an image that share a common property, and in our case that property would be the grayscale value of the pixel (or height information per pixel) [62]. To reduce the effect of background frequencies, contamination or dirt on the surface, and surface defects that differ significantly in size to tracks, a Gaussian blur (or a low-pass frequency filter) is applied to the image before blob detection. This image blurring

significantly reduces incorrect blob detection from small variations in pixel contrast (small height variations on the surface) due to either instrument noise, general surface etching, and other unwanted surface effects. This reduction in noise can be visualized in Appendix Section B, Fig. B.1.

Once blobs (etch pits) are detected in an image, the code will produce a histogram of blob depths and blob diameters, a coordinate-numbered blob map, and a statistical profile of each image in .csv format. The statistical profile output of an image contains the date and time the image was collected, minimum and maximum height and pixel values, the real-space dimensions of an image, the magnification and resolution of the image, the detected blobs and their coordinates and sizes, and any additional image information that is helpful. The measured depth (or height, if a bump) along with the geometry of the etch pit will allow the user to determine whether the etch pit is track-induced. Tracks in images can be detected based on a variety of user-determined thresholds including color (contrast), circularity, convexity, inertia ratio, and area of the blob [62]. The ability to filter based on blob shape is a powerful tool that will aid in the evolution of the automatic track detection code. Track shapes will directly depend on the angle to the cleave surface. The schematic diagram in figure 3.3 shows how track shapes vary from a cross-sectional to top point of view. Eventually this code could become powerful enough to detect and sort tracks based on angle to the surface.

One way we can do this mathematically is by computing an aspect ratio between measured track depth and diameter:

$$\beta = \frac{d}{L}, \tag{3.1}$$

where β is the aspect ratio, d is the track depth, and L is the track diameter [14]. A visualization of these values in terms of etch pit geometry and angle to the cleave can be seen in Figure 3.4. If tracks are approximately the same length, the mean aspect ratio will *increase* as the angle of the track to the cleave surface *decreases*. This means that the more parallel a track is to the cleave plane, the higher the aspect ratio. In addition to a dependence on angle, for tracks at approximately equal angles to the cleave surface, the mean aspect ratio will *increase* as track length *increases*. For our purposes, an aspect ratio closer to zero will allude to the *diameter* of an etch pit to be approximately the track length of the nuclear recoil. On the contrary, an aspect ratio of or above 1 reveals that the track would be at a high angle to the cleave surface, and thus the etched depth of a track would in fact be a *minimum* track length (assuming the cleave captured a only a partial track). Partial track lengths can add a bit of ambiguity in measurement, but to minimize this error one can compare two etched matching cleaves, and those etch pits that mirror each other will represent opposite ends of a track, and those that are spontaneous will represent tracks lying nearly in the cleave plane [36, 37].

Also within the statistical profile output of the script, roughness parameters are calculated per image area. Specifically the arithmetic mean height, root mean squared roughness, and skewness. The roughness of a surface usually describes a mathematical relationship between the peaks and valleys present on a surface or line profile.

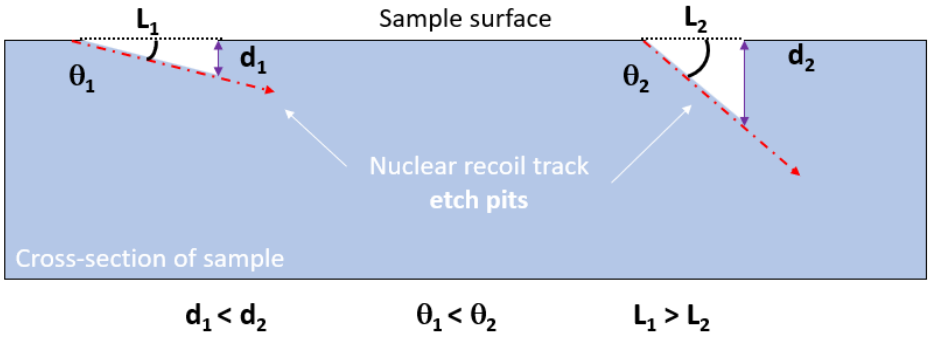

Fig. 3.4: Visualization of track etch pit dimensions with respect to intersection angle, where θ is the angle of the track to cleave surface, L is the diameter (long-axis) of the etch pit, and d is the etch pit depth.

Arithmetic mean height, R_a, is the most universally used parameter and gives a decent general description of the height variations within an area [11]. R_a is not sensitive to small changes in profile. It is expected that as etching time increases, the roughness of the sample area will also decrease due to general etching of the surface and preferential etching within spontaneous and preexisting defects. The mathematical definition is as follows:

$$R_a = \frac{1}{n}\sum_{i=1}^{n} |y_i|, \tag{3.2}$$

where n is the total number of height data points given, and y is the measured height at a point i [11]. The units of R_a are the the same units as each input height y.

Root mean squared roughness, R_q, (also known as RMS) represents the standard deviation of the distribution of surface heights [11]. It is more sensitive to small profile

changes. The mathematical definition of RMS is as follows:

$$R_q = \sqrt{\frac{1}{n}\sum_{i=1}^{n} y_i^2}, \tag{3.3}$$

where n is again the total number of height points and y is the measured height at point i [11]. The units of R_q are the the same units as each input height y.

The last roughness parameter included in the statistical output profile is skewness, R_{sk}, which measures the symmetry of a profile about the mean line, which is calculated by RMS [11]. R_{sk} is sensitive to occasional deep valleys and high peaks, which can be beneficial when comparing images with more or less track densities as not every etched track signal in a height image will be obvious by the eye [11]. Skewness will be positive if there are many peaks and not many valleys in an image, and negative when there or more or very deep valleys present. The parameter is also useful to distinguish between two profiles that may have the same R_a and R_q but have different shapes present (like different geometries of tracks)[11]. A good visualization is provided in Appendix B Fig. B.3. The mathematical definition of skewness is as follows:

$$R_{sk} = \frac{1}{NR_q^3}(\sum_{i=1}^{N} Y_i^3), \tag{3.4}$$

where R_q is the RMS, N is the total number of height points given, Y is the measured height at each point i. Skewness is unitless.

3.3.1 Etching Rate Calculation

Once tracks have been detected and measured, the next step is to develop a mathematical etching rate model to convert the size of etched tracks back to the original, undetectable length before etching. Typically two etch rates are measured: parallel to the surface, and normal to the surface. To establish a chemical etch rate, one usually measures the depths and radii of etch pits over etching time [37, 63, 64]. Chemical etching of Muscovite and Phlogopite mica is known to be anisotropic because of the layered nature of the crystals, and although limited, a study suggests this pattern is consistent amongst plasma etching as well [14, 37, 63, 64]. Plasma etch rates are often difficult to determine due to backscattering, unknown ion fluxes, and fluctuations in chamber pressure and power. Due to this ambiguity, we expect the plasma etching rates to not be consistent across every etching, so we will approximate an average etch rate across the same experimental parameters. Averaging the etch rate will not compromise our track length studies as we are more focused on a density of tracks within a certain measured range of lengths, and we take into account measurement error. The etch rates will be calculated as a change of depth over time and a change of radius over time (nm/min).

3.3.2 Mineral Dating

The primary method of detecting a mineral's age is fission track dating. In fission track dating (FTD) one measures the track densities of ^{238}U spontaneous fission in the mineral sample itself, and then the track density of induced ^{235}U fission usually as a result of

thermal neutrons [17, 65]. The induced tracks can be measured either by annealing the mineral sample before neutron irradiation, or using an external detector pressed to an open cleave of sample, often Muscovite mica [28, 65]. It is often recommended in FTD studies to induce these ^{235}U tracks, as the thermal history of the mineral is often unknown, thus the concentration of spontaneous ^{238}U fission *can* be unreliable for an absolute age calculation. In addition to the mineral itself creating limitations, the use of neutron irradiation can create ambiguity because the true thermal neutron fluence is difficult to determine [65]. There have been advancements in reducing uncertainty in neutron irradiation but it creates a dependency on equally difficult methods.

Another less widely used method of mineral dating is *α-recoil dating* [17]. In this technique, the density of damage tracks left by recoils of daughter nuclei in α-decays in the ^{238}U, ^{232}Th, ^{235}U, and ^{147}Sm decay chains are measured [17, 30, 66]. These tracks are on the order of 30 nanometers and 45 nanometers, unetched, in micas and halite respectively [17]. This technique relies on a detailed analysis of background influence in minerals, as well as a proper etching rate, in order to isolate the specific tracks from these decay chains. There have been different mathematical expressions developed to relate the age of the mineral to the density of alpha-recoil tracks. Reference [67] gives:

$$\rho_\alpha = N_v[C(U)\lambda(U) + C(Th)\lambda(Th)]R_\alpha T, \tag{3.5}$$

where ρ_α is the density of alpha-recoil tracks per unit area, N_v is the number of atoms per volume of target mineral, $C(U)$ and $C(T)$ are the fractions of uranium and

thorium in the mineral respectively, $\lambda(U)$ and $\lambda(Th)$ are the decay constants of uranium and thorium respectively, R_α is the range of alpha-recoil tracks, and T is the age of the mineral, assuming the age is $\ll 1/\lambda$. A more recent study by Reference [68] introduces a new equation:

$$\rho_\alpha = \sum_{i=1} [exp(\lambda_{\alpha i} T) - 1](N_v C_i R_{\alpha i} n_i), \tag{3.6}$$

where ρ_α is the density of alpha-recoil tracks per unit area, N_v is the number of atoms per volume of target mineral, C_i is the fraction of atoms representing element i, $\lambda_{\alpha i}$ is the decay constant of the ith element concerned, $R_{\alpha i}$ is the range of alpha-recoil tracks concerning series i, n_i is the etching efficiency due to element i, and T is the age of the mineral. This alternative equation was introduced because the earlier equation produced by Ref. [67] did not account for unequal etching efficiencies, inadequate alpha-recoil range calculations, unequal alpha-recoil range calculations varying per element, varying alpha-recoil densities over etching time, and static track positions with respect to parent isotopes [32].

For our research purposes, it is important that the *exposure time* for a target mineral is estimated. The exposure time of track preservation is not necessarily always the mineral age, due to the unknown thermal history of the mineral (discussed in Section 1.2). We do not have access to neutron irradiation or gamma spectroscopy technology here at UNF, but we can use the alternative alpha-recoil method of mineral dating to get an approximate exposure time. In addition, we are mostly interested in the specific

^{238}U to ^{234}Th decay chain for background estimation, so to capture a decent estimation of exposure time we will use Equation 3.5, however we will use more accurate theoretical estimates of alpha-recoil track ranges produced by Reference [32] and verfied by Reference [5]. Although we are only using an estimate, success of future paleodetector studies will partially rely on knowing the exact exposure time and mineral age. Knowing the mineral age as it compared to track exposure time could reveal important information about the thermal history of the mineral, which in turn could allude to phenomena like track shortening or erasure [32, 38].

3.3.3 Theoretical Track Length Estimates

The measured track lengths within the target mineral can be used as a proxy for the energy of the nuclear recoil and can then be compared to a *theoretical track length spectrum* that is unique depending on the specific mineral and influence of background signals in that mineral [5, 15, 16, 17]. One can then potentially distinguish CC SN neutrino and WIMP dark matter signal from background [17]. To do this, we used the mathematical models and framework first produced by Reference [5][1] and all following works, and adapted the code to fit our own replicated and new simulations produced in the computer program Stopping and Range of Ions in Matter (SRIM) [69].

The first step is to establish a theoretical signal from neutrinos - which will include the CC SN neutrino signal we are interested in detecting. Although neutrinos play

[1] Note that all mathematical models detailed in this section were produced by Reference [5], and serve as a detailed explanation in how our theoretical track length spectra are derived for each mineral.

an important role in the explosion of supernovae, the neutrino spectra emitted from this explosion is not well understood [5, 16, 19]. The only experimental data we have stems from the one SN observed by neutrino detectors in our history - SN 1987A (occurred in the Large Magellanic Cloud) - and furthermore the collection of emission events following the supernova that were observed by various telescopes around the world [5]. Following these experimental observations, researchers have been able to fit simulation data to experimental data, and deduce that neutrino spectra can be well-fitted by a pinched Fermi-Dirac distribution:

$$\left(\frac{dn}{dE}\right)_{\nu i} = E_{\nu}^{tot}\frac{(1+\alpha)^{1+\alpha}}{\Gamma(1+\alpha)}\frac{E^{\alpha}}{\langle E_{\nu}\rangle^{2+\alpha}}e^{[-(1+\alpha)\frac{E}{E_{\nu}}]}, \tag{3.7}$$

where E_{ν}^{tot} is the energy radiated in the neutrino species ν_i, $\langle E_{\nu}\rangle$ is the average neutrino energy (approximately the core temperature of the SN), and α is the spectral shape parameter[2] [5]. The relevant neutrino flux that will dictate the influence of the background can be computed by summing the neutrino spectra for all neutrino flavors:

$$\left(\frac{dn}{dE_{\nu}}\right) = \left(\frac{dn}{dE}\right)_{\nu_e} + \left(\frac{dn}{dE}\right)_{\nu_{\bar{e}}} + 4\left(\frac{dn}{dE}\right)_{\nu_x}, \tag{3.8}$$

following data produced by References [13] in Table 3.1 [5]. The dominant source of nuclear recoils from neutrinos arise from neutral current interactions[3], which are

[2] A spectral analysis of backgrounds in paleo-detectors was conducted by Reference [20] and work elaborated in Reference [5] follows this study as well.

[3] Neutral current interactions are a type of neutrino interaction with nuclei, which transfers energy and momentum to the nucleus [70]. In the neutral current interaction, which occurs through the exchange of a Z_0 boson, the neutrino remains a neutrino and is present in the final state [70]. In this case a recoil of the target nuclei can be detected [70].

ν	E_ν^{tot} **[erg]**	$\langle E_\nu \rangle$ **[MeV]**	α
ν_e	6×10^{52}	13.3	3.0
$\nu_{\bar{e}}$	4.3×10^{52}	14.6	3.3
ν_x	2×10^{52}	15	3.0

Table 3.1: Neutrino spectra parameters for electron neutrinos (ν_e), anti-electron neutrinos ($\bar{\nu}_e$), and $\nu_x \equiv (\nu_\mu, \bar{\nu}_\mu, \nu_\tau, \bar{\nu}_\tau)$ for numerical calculations of Eq. 3.7 from Ref. [13].

flavor-blind, thus summing over all spectra and considering interaction between them is an accurate estimation [5]. In addition, because there interactions are flavor-blind, neutrino oscillations can also be negligible [5].

A time-averaged neutrino spectrum for galactic core-collapse supernovae at Earth can be obtained by integrating over the probability density $f(R_E)$, describing the likelihood a CC SN would occur a distance R_E from Earth:

$$\left(\frac{d\psi}{dE_\nu}\right)^{gal} = \dot{N}_{CC}^{gal} \frac{dn}{DE_\nu} \int_0^\infty dR_E \, \frac{f(R_E)}{4\pi R_E^2}, \tag{3.9}$$

where $\dot{N}_{CC}^{gal}$ is the galactic CC SN rate [5]. The integral of R_E should theoretically be finite over the dimensions of our galaxy, but instead Reference [5] includes a probability density $f(R_E)$ that takes into account only CC SNe in the galactic disk of the Milky Way galaxy. The spatial distribution of CC SNe, ρ, can be modeled by a double exponential function that considers the height about the galactic mid-plane and

the galactocentric radius:

$$\rho \propto e^{-R/R_d}\, e^{-|z|/H}, \tag{3.10}$$

where R is the radius and z is the height, with disk parameters of R_d and H [5]. The galactocentric radius and height about the galactic mid-plane will change over exposure time of the mineral due to the motion of the Earth and Sun in our galaxy, but this positional change only minimally affects the estimated neutrino flux, therefore it can be neglected [5]. In Appendix Section B, Figure B.2 shows a schematic diagram of these galactic coordinates with respect to the Sun, from Reference [10].

Figure 3.5 displays the estimated neutrino flux by Reference [5] compared with the estimated Diffuse SN Background (DSNB) following the work of Reference [6]. This CC SNe neutrino flux estimate is roughly 100 times that of the DSNB flux - leading to the DSNB to be a relatively negligible background signal in paleo-detectors studies [5]. It is assumed here that the galactic CC SN rate is approximately $\dot{N}_{CC}^{gal} = 2.3 \times 10^{-2}\ yr^{-1}$, predicted by Reference [71] [5]. The CC SNe rate was estimated in Reference [71] based on the observed rates of SNe in the local Universe, determined by the Lick Observatory Supernova Search. The estimate took into account 726 supernovae across the local universe, and are consistent with the SNe rates of other published studies [71]. It is important to note, however, that this rate is something we aim to *refine* by directly detecting the nuclear recoils induced by galactic CC SNe neutrinos. Due to only one human-observed SN in neutrinos within our local group of galaxies (1987A),

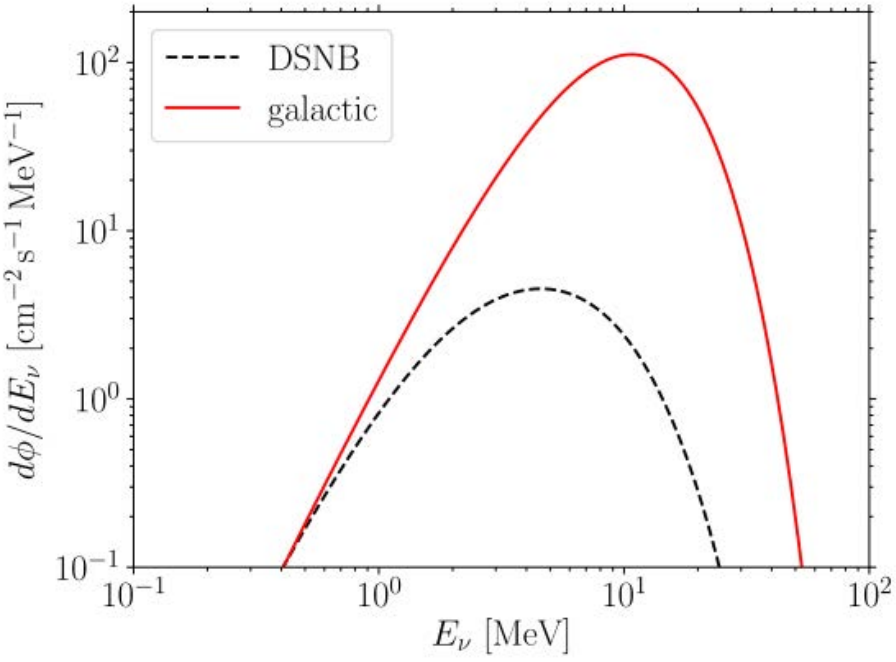

Fig. 3.5: Estimated neutrino flux $\frac{d\phi}{dE_\nu}$ (red line) from galactic CC SNe at Earth, compared with the estimated DSNB neutrino flux (black dotted line), from Refs. [5, 6]. Here, the galactic CC SN rate is assumed to be $\dot{N}_{CC}^{gal} = 2.3 \times 10^{-2}\ yr^{-1}$ [5].

this rate is not something we can directly detect, and prior to the proposal of the paleodetector technique, this rate could only be approximated based on SN rates of the local Universe.

The most important step in developing mathematical models to predict background spectra is the connection between the observable - the nuclear recoil damage tracks of 1-1000 nanometers - and the theoretical flux of background signals. Neutrinos of energies less than or on the order of hundreds of MeV will give rise to nuclear recoil damage tracks [5]. The *differential recoil spectrum* per unit target mass can then be calculated based on the energy of the incoming neutrino:

$$\left(\frac{dR}{dE_R}\right)_T = \frac{1}{m_T} \int_{E_\nu^{min}} dE_\nu \frac{d\sigma}{dE_R} \frac{d\phi}{dE_\nu}, \tag{3.11}$$

where E_R is the recoil energy, m_T is the mass of target nuclei T, $\frac{d\sigma}{dE\nu}$ is the differential neutral current interaction cross section[4], and $E_\nu^{min} = \sqrt{M_T E_R/2}$ is the minimum neutrino energy required to induce a nuclear recoil [5]. The recoil spectrum in Eq. 3.11 can be converted into a *track length spectrum* by summing the stopping power dE_R/dx_T over all target nuclei T in a mineral:

$$\left(\frac{dR}{dx}\right) = \sum_T \xi_T \frac{dE_R}{dx_T} \left(\frac{dR}{dE_R}\right)_T, \tag{3.12}$$

where x_T is the track length of the recoil with target nuclei T, ξ_T is the mass fraction of

[4] The differential neutral current interaction cross section is computed in more detail in Ref. [5]. The cross section is dependent on the Fermi coupling constant and the Helm nuclear form factor, which is a function of interaction angle, the number of nucleons in the target mineral, momentum transfer, and nuclear radius [5].

T [5]. The stopping power of nuclei in a target mineral can be simulated with SRIM [5, 69]. We simulated our own stopping powers using SRIM, first replicating the mineral track legnth spectra in Refs. [5, 15, 16, 19, 20] to ensure accuracy of our simulations. SRIM is a computer program built to calculate the stopping and range of ions (up to 2 GeV/amu) into matter using a quantum mechanical treatment of ion-atom collisions (assuming a moving atom as an "ion", and all target atoms as "atoms") [69]. The user only needs to input the target mineral by using the precise chemical composition, and designate the energy range of incoming ions. For this research, we used an energy range of 10 eV to 10 MeV. The track length of a recoiling nucleus can be calculated as:

$$x_T(E_R) = \int_0^{E_R} dE \left|\frac{dE}{dx_T}\right|^{-1}, \tag{3.13}$$

where E_R is the energy of the recoiling nucleus [5].

A similar mathematical approach to finding a neutrino flux can then be used to find the track length spectrum for WIMP dark matter particles. From Reference [19], the differential recoil spectrum for a WIMP with mass m_T is given by:

$$\left(\frac{dR}{dE_R}\right)_T = \frac{2\rho_\chi}{m_\chi} \int d^3v \; v \; f(\mathbf{v}, t) \; \frac{d\sigma_T}{dq^2}(q^2, v), \tag{3.14}$$

where E_R is the recoil energy, ρ_χ is the local WIMP mass density, $f(\mathbf{v}, t)$ is the WIMP velocity distribution. and $d\sigma_T/dq^2$ is the differential WIMP-nucleus scattering cross section with $q^2 = 2m_T E_R$ momentum transfer [19]. The differential scattering cross section[5] can be approximated as a zero-momentum, spin-independent cross section

[5] A more in-depth breakdown of the cross section derivation, velocity distribution simplification, and estimation of mass density can be found in [19].

$\sigma_p^{SI} = 10^{-45}$ cm^2 [19]. The track length spectrum for WIMP DM-induced nuclear recoils is the same in structure as Eq. 3.12, with differing recoil spectra given by Eq. 3.11 and 3.14 respectively.

The signal of ^{238}U $\rightarrow$ ^{234}Th+α decay, one of the more dominant signals in target minerals, is approximated based on the age (or more accurately, exposure time) of the target mineral. For minerals with exposure time short compared to the half-life of ^{238}U and long compared to the half-life of ^{234}U, the number of single-α events per unit target mass is well approximated by:

$$n_{1\alpha}^{238} = 10^9 \mathrm{kg}^{-1} \left(\frac{C^{238}}{0.01 \mathrm{ppb}} \right), \tag{3.15}$$

where ^{238}C is the concentration of uranium-238 in the target mineral [5, 19]. However, because we do not have an age estimate prior to analyzing our target minerals, the number of events per mineral age (exposure time) t is given by:

$$N_{1\alpha}^{238}(t) = N_{238}^0 \, \frac{\lambda_{238}}{\lambda_{234} - \lambda_{238}} \, (e^{-\lambda_{238} t} - e^{-\lambda_{234} t}), \tag{3.16}$$

where λ_{238} (λ_{234}) is the decay constant of ^{238}U (^{234}U), and N_{238}^0 is the number of ^{238}U atoms per unit target mass [5, 19]. Similarly, we can approximate the amount of spontaneous nuclear fission events in the mineral per unit target mass and mineral age (exposure time) from uranium-238 concentration by:

$$n_{SF}^{238} = \frac{N_{238}^0}{M_T} \, (1 - e^{-\lambda_{238} t}) \, \frac{T_{1/2}^{238}}{T_{1/2}^{238}}, \tag{3.17}$$

with $T_{1/2}^{238}$ ($T_{1/2}^{238}$) related to the decay constant of ^{238}U (^{234}U) by $\lambda = ln(2)/T_{1/2}$ [5, 19]. All recoil spectra of background signals can be plotted together as an interaction rate function dependent on mineral mass, exposure time, and track length. The interaction rate of all applicable signals and backgrounds can be integrated over the measured track lengths and multiplied by the mass and age of the sample, which would yield constant values corresponding to the specific amount of tracks produced by a given background. Those values can then be fit and compared to experimental data. Theoretical track length spectra calculations and plots are created in Python, following the work of Refs. [5, 15, 16, 18, 19, 20].

Chapter 4

Results and Discussion

4.1 Halite Track Detector

To characterize etched and track-defected surfaces of halite crystals, we first must characterize the unetched surface and any naturally occurring crystal defects that will still be present after etching. The unetched surface of halite was analyzed with both the Keyence VK-X1000 laser confocal microscope (LCM) and the atomic force microscope (AFM). Under the AFM and LCM, steps were observed, signifying the fracture of different crystal planes when cleaving. These steps are crystallographic in nature and can be pictured in Figure 4.1. Before etching any halite samples, the unetched sample was imaged under the LCM.

We expect our sample of halite to have a particularly high density of tracks, coming mostly from radioactive decay and neutron-induced tracks. Due to this, tracks should be relatively easy to find if the etching conditions are correct. The first etching experiment conducted with halite was a solution of ferric chloride powder mixed with glacial acetic acid, at a ratio of 4 grams of ferric chloride powder with 1 liter of glacial

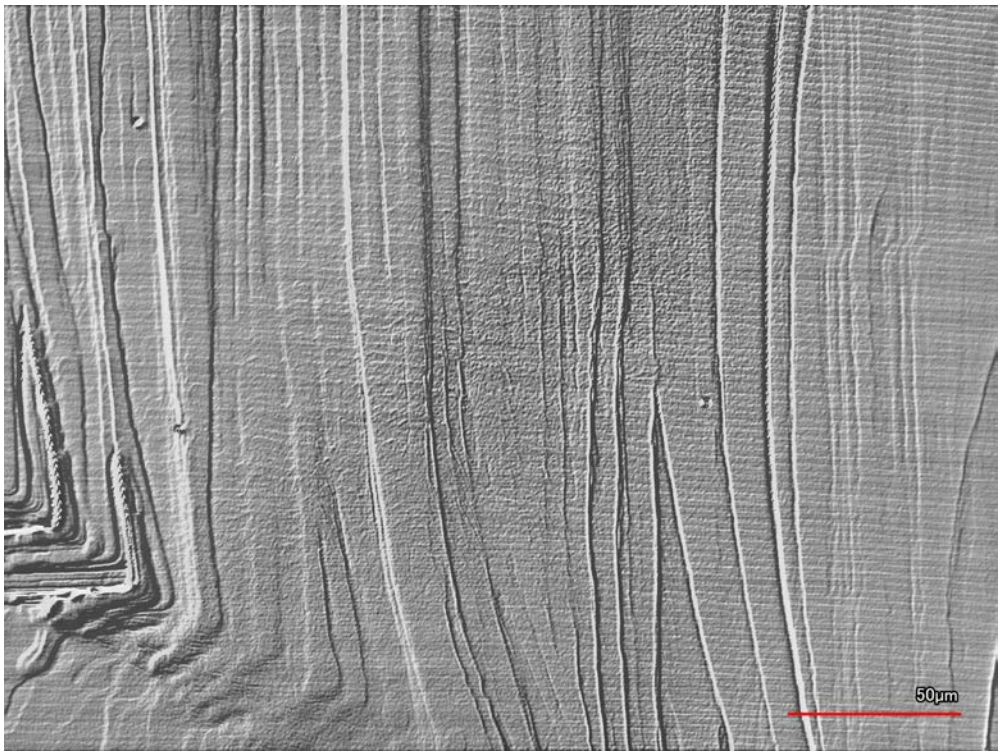

Fig. 4.1: The unetched surface of halite imaged with the Keyence VK-X1000 at MSERF, at a magnification of 50x (C-Laser DIC image, see Appendix Section A.5).

acetic acid. Experimentally, this equated to 0.0072 grams of ferric chloride powder mixed with 1.5 milliliters of acid. Samples of halite were freshly cleaved with a rock hammer and after etching, the samples were rinsed in acetone for a few seconds and left to air dry. In total five samples were etched at times of 15 seconds, 30 seconds, 45 seconds, 1 minute, and 2 minutes. The 45 second etch sample had a matching cleave that was left unetched. All samples were first analyzed under a standard optical microscope, and etched samples became less transmissive than unetched halite samples, verifying that the samples did indeed etch and the decrease in transmission is then due an increased surface roughness, which increases the overall scattering of light on the surface. We then took the samples to MSERF and imaged them under the LCM.

Theoretically, detecting tracks in halite will ultimately be more difficult than detecting tracks in minerals like mica simply because of the lack of scientific study on the mineral as a track detector. Under the LCM, the chemically etched surfaces of halite did not appear to reveal any pits other than natural crystallographic pits due to the general erosion of the surface (Fig. 4.2). It was hypothesized that the etchant was attacking the surface too severely, causing the general etching rate to be so high that any traces of tracks were eroded before they could properly be revealed. The experiment was repeated numerous times, lowering the etching time, but there were ultimately no tracks revealed with this method.

We decided to try an alternative route - argon plasma etching of halite with the Deiner Pico plasma cleaner. There has yet to be any published research on the effects of

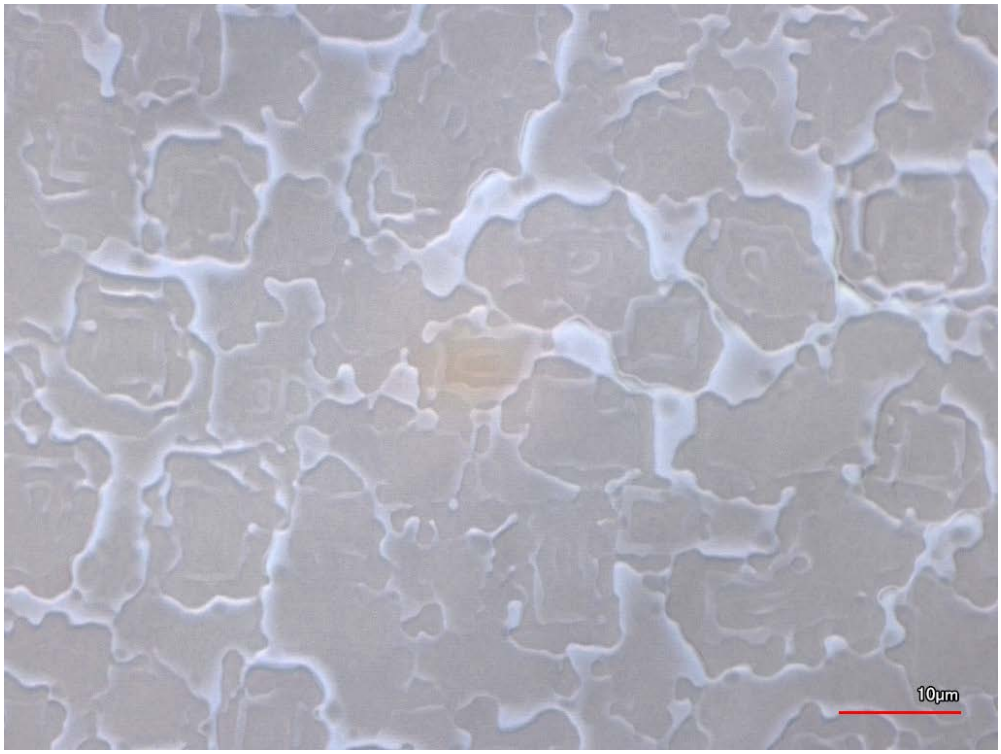

Fig. 4.2: Laser image of chemically etched halite surface showing crystallographic etch pits arising from the general surface etching of the mineral. Imaged with the Keyence VK-X1000 at MSERF. The brown spot in the middle of the image is slight burning of the sample from the laser.

dry etching halite, nonetheless revealing nuclear recoil tracks. Unsure of whether this method would work, we tried the general experiment parameters for plasma etching mica (discussed more in Section 4.2) to see if the results were different than the outcome of chemical etching. We plasma etched halite at a power of 100 Watts, a pressure of 0.2 mbar, and for a time of 10 minutes, and did not clean the sample afterwards. We refrained from cleaning to keep a controlled experiment, as there is no prior literature that uses dry etching on natural halite, and we wanted to prevent any surface altering due to cleaning methods. In addition, plasma will eradicate any organic material on the surface of the mineral. Mostly larger debris, like shards on the surface, might remain after etching. The sample was immediately taken to MSERF for imaging under the LCM, along with a matching cleave that was left unetched. A high density of etch pits and bumps were observed scattered across the surface (Fig. 4.3).

The root mean square roughness of the unetched halite cleave is approximately 2 nm, whereas the plasma etched cleave roughness if approximately 45 nm. The argon plasma, at this power level and etching time, significantly eroded the surface. The larger, comet-like shapes in Fig. 4.3(a) are long, narrow pits accompanied by a large bump nearly the same length of the pit. It is likely that these bumps are caused by the redeposition of matter back onto the sample surface. Ref. [14] hypothesizes that highly defected areas of samples, like those containing a high density of tracks, will not only have randomly deposited hillocks of particles back onto the surface, but track etch pits themselves will often be accompanied by redeposition bumps on the sides of the

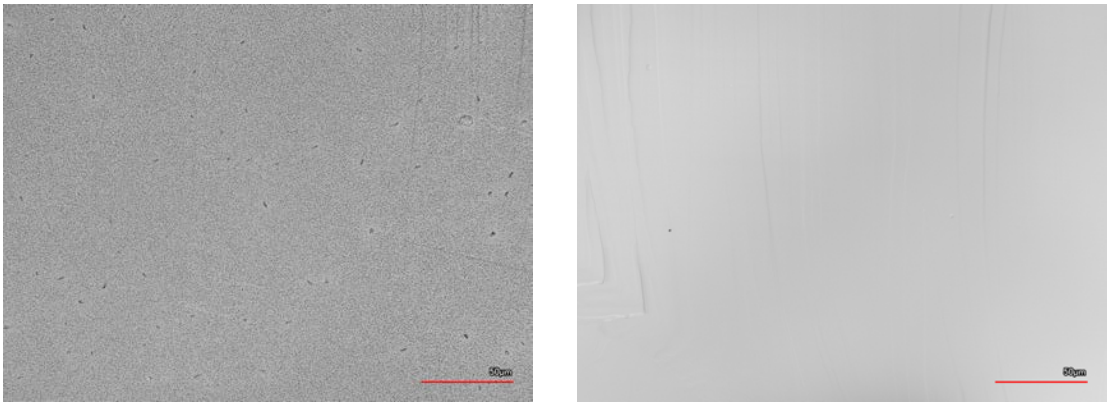

(a) **(b)**

Fig. 4.3: (a) Laser image of plasma etched halite (100 W/0.2 mbar/10 minutes) and (b) laser image of the matching cleave of unetched halite. Imaged with the Keyence VK-X1000 at MSERF at a magnification of 50x.

track pit. With this information, it is possible that the long, angled pits in Fig. 4.3(a) are nuclear recoil track etch pits, however at this point results were inconclusive, as the experiment has yet to be replicated. The very high density of small shapes in the background are believed to be collection of etch pits arising from natural crystal defects, and also etch pits due to the general surface etching of halite, and potentially etch pits from smaller and angled tracks. For this specific experiment, the plasma power and/or etching time were too high to only preferentially reveal crystal defects in a manner that would reveal tracks, but the results were promising. There has yet to be a study analyzing the dry etching of halite with argon plasma, and in addition, this is a entirely new method of revealing nuclear recoil damage tracks present in the mineral. The promising results of this experiment initiated a series of new experiments using different

power levels, etch times, and pressure of plasma etching, and also incorporated sample cleaning afterwards.

Using power levels of 20 W, 50 W, and 100 W, samples of freshly cleaved halite were plasma etched for 5 minutes each at 0.2 mbar, and afterwards cleaned in acetone. The samples were then taken to MSERF for imaging under the LCM. Interestingly, these plasma etched halite surfaces showed the same exact crystallographic pits that appeared after chemically etching the mineral (Fig. 4.4 compared to Fig. 4.2). We soon realized that our earlier hypothesis of chemical etching with a ferric chloride solution - that the etchant itself was corroding the surface too severely to see tracks - was incorrect. It was the acetone cleaning that further eroded the surface after etching.

These results initially puzzled us, because halite is practically insoluble in acetone, with a solubility of 3.2×10^{-5} wt % at 18 °C, compared to a solubility of 26.41 wt % at 20 °C in water [72]. There was not a straight forward answer as to why the surface of halite was showing such significant etching after the rinse. However, after further investigation into the solubility of NaCl, etching halite on a humid day, or even just an abundance of moisture in the atmosphere can result in the wet etching of halite with water and even different etch pit geometries [73, 74]. It could have been anything from a humid environment in the lab, or the water molecules in the air during the short walk outside from Building 50 to Building 4, where MSERF is located, that caused this additional etching of the samples. Although careful consideration was taken to enclose the samples in Petri dishes and store in an enclosed box, the high sol-

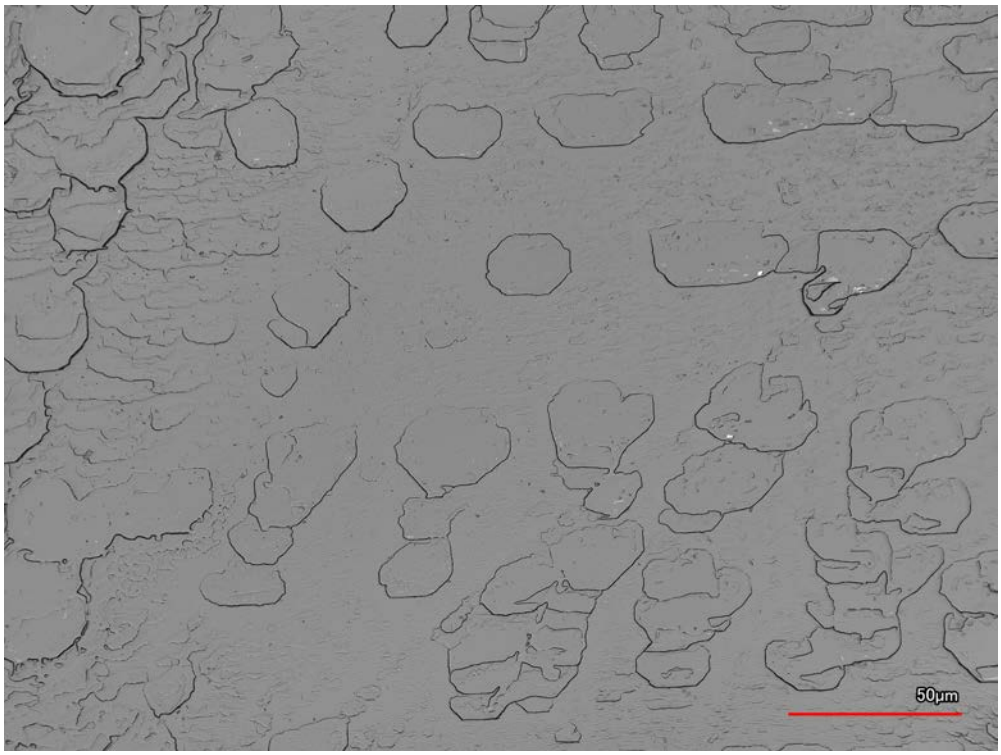

Fig. 4.4: Laser image of argon plasma etched halite (20 W/0.2 mbar/5 minutes), cleaned with acetone. Imaged with the Keyence VK-X1000 at MSERF with a magnification of 50x.

ubility of Na Cl in water, coupled with the increase of this value as temperature rises, results in a very sensitive environment [72, 73]. In addition to atmospheric effects, the solubility of halite in acetone increases if the acetone is mixed in part with water [73]. Although the acetone we used was listed as having greater than 99.5% purity, it is possible that even a minute percentage of water could have etched the mineral. In future experiments, halite was cleaned with isopropanol after etching and secured in a Petri dish wrapped in Parafilm to help minimize effects from humidity.

To further verify that the sample etching was inconclusive due to additional etching from either acetone, water, or a mixture of both, we plasma etched these samples again (at the same conditions) but did not clean with acetone afterwards. The plasma etching did reveal new etch pits (Fig. 4.5) very similar to those induced by tracks in the first run by general surface sputtering (pictured in Fig. 4.3). After the effectiveness of plasma etching was verified, new samples of halite were freshly cleaved, and etched for 20 W, 50 W, and 100 W, each at 0.2 mbar for 5 minutes, and afterwards cleaned with isopropanol. The samples etched at 50 W and 100 W had too defected of a surface to adequately reveal tracks. The 20 W sample was clean and smooth enough to image the sample surface, and the decreased power and/or etch time did result in significantly less general surface etching, and instead preferentially etched only defected areas. Images of these etch pits can be found in Figure 4.6. The density of etch pits on this new sample of halite averages at approximately $5.8 \times 10^3 cm^{-2}$. As expected, at a lower etching time and lower plasma power level, less etch pits are revealed, compared

to the higher density of (possible) tracks in Fig. 4.3. The extremely high magnitude of surface erosion present in Fig. 4.5 further implies that plasma etching halite at a low power level will preferentially attack weakened regions on the surface. Although the plasma etching conditions of Fig. 4.5 and Fig. 4.6 are the same, the acetone (or water) etch in Fig. 4.5 has already weakened nearly all of the surface area on the sample, and the lower bond energies present in these weakened areas will overall cause more plasma etching to occur, explaining the rough surface. In Fig. 4.6 you can see that aside from the spontaneous etch pits, the surface is left relatively untouched.

Up until this point, we can see the effects of plasma etching halite, but the etch pits revealed that were not considered natural crystal defects were small enough that with the resolution of the LCM, the geometry of the pits could not be determined. We know that with plasma or chemical etching, the shapes of tracks should vary between circular (normal to cleave surface) and comet-shaped (lying within the plane of the cleave), and randomly scattered on the surface, with random orientations. Differentiating between tracks and natural crystal defects in halite can be aided with a thorough literature review. Although plasma etched halite and associated etch pits arising from natural crystal defects has not been studied before, there has been study into these etch pits as they arise with chemical etching [74, 75]. In addition, work by Reference [14] noted that the dimensions and geometry of crystal defects enlarged by argon plasma etching should be relatively conserved in Muscovite mica. It is assumed that this would be the case for any crystal, as plasma etching is a kinetically driven process. In addition,

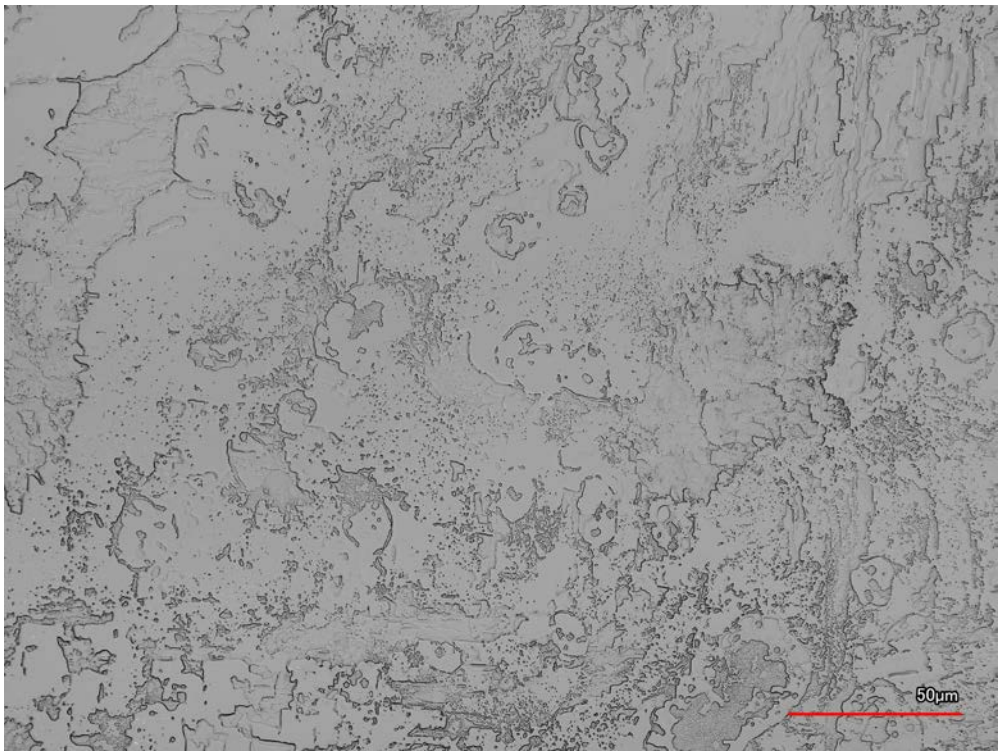

Fig. 4.5: Laser image of halite cleaned with acetone, then plasma etched at 20 W/0.2 mbar/5 minutes. Imaged with the Keyence VK-X1000 at MSERF at a magnification of 50x.

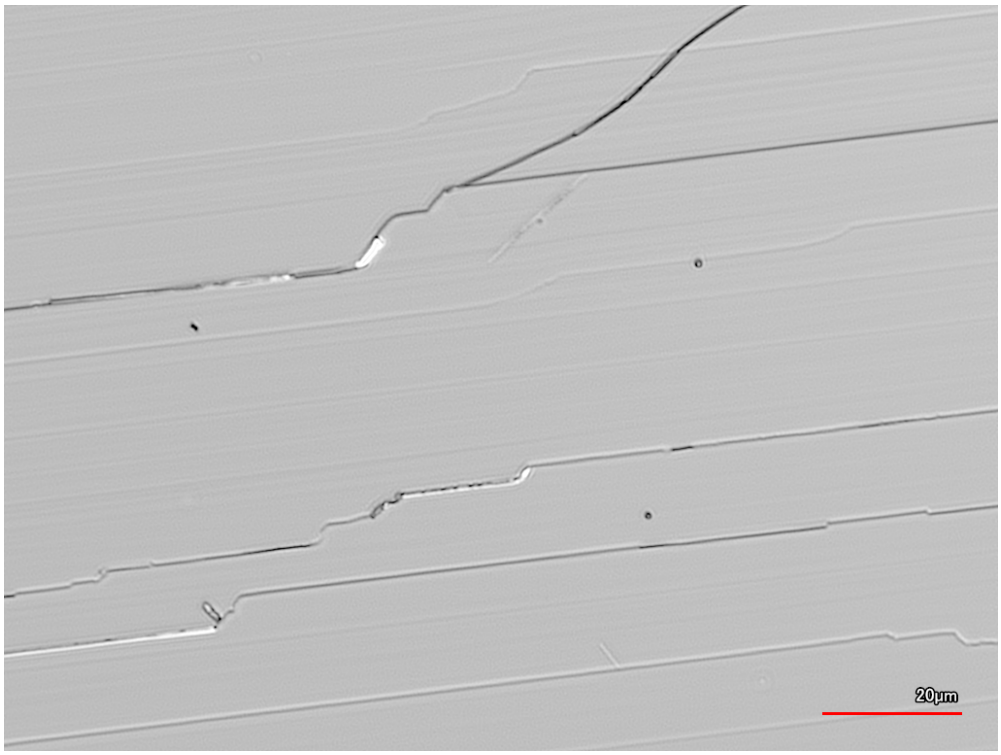

Fig. 4.6: Laser image of argon plasma etched halite (20 W/0.2 mbar/5 minutes). Sample was cleaned with isopropanol after etching. Imaged with the Keyence VK-X1000 at MSERF with a magnification of 20x.

plasma cleaner etching is isotropic, and argon is essentially nonreactive. Point defects in halite will usually appear as square or rectangular etch pits that are easily distinguishable from tracks (at the proper resolution) [74, 75]. Appendix B Figure B.4 shows square and rectangular pits in halite after plasma etching with argon, arising from either the general etching of the surface, or in some cases, remnants of fluid inclusions formerly present in the crystal lattice [76]. This phenomena was observed amongst many samples, alongside tracks or isolated. Dislocation etch pits in halite are easily identifiable because they are pyramidal in shape with a square base [77]. Dislocations are planar defects, thus the etch pits arising from localized points of low potential energy will not only be symmetric amongst the crystal structure, but also follow a clear trail that can easily be identified with the help of a matching cleave [74, 77, 78]. An image of square pyramidal dislocation etch pits in halite can be seen in Figure 4.7. Tracks will appear as comet-shaped, damaged regions of samples that can not arise from any natural, crystallographic defect, and will be relatively straightforward to identify.

We continued to replicate experiments using argon plasma etching at 100 W, 0.2 mbar, and 10 minute etching parameters, and this was the closest we have gotten to reveal track-like structure in halite. Cleaning before and after plasma etching to remove debris from the surface. Debris on the sample surface before etching can not only cause increase etching and redeposition (scattering of more debris), but debris can also fuse onto the sample surface if bombarded at a high enough energy. Using the appropriate cleaning, we began to see the same comet-shaped structures appear in different samples

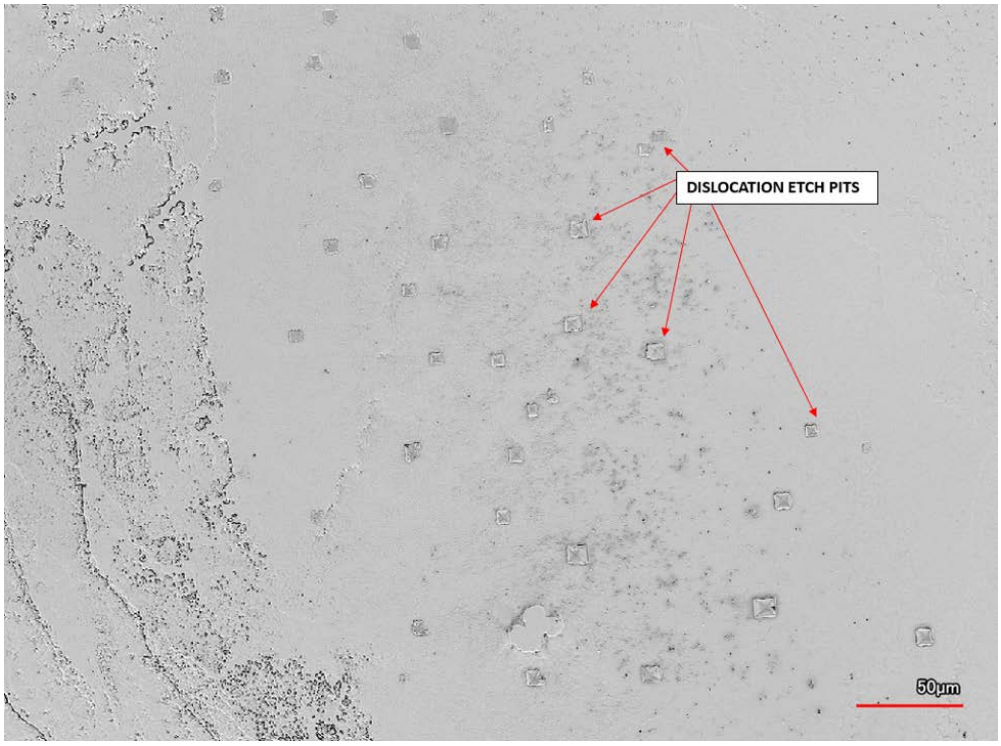

Fig. 4.7: Dislocation etch pits revealed in halite after plasma etching with argon at 100 W/0.2 mbar/10 minutes and cleaning with isopropanol. Imaged with the Keyence VK-X1000 at MSERF, at a magnification of 20x and zoom of 75%.

etched under the same conditions as Fig. 4.3.

After further investigation and imaging of the etch pit dimensions, density, and geometry, we believe that these unique etch pits pictured cannot be due to any other defect other than nuclear recoil tracks. Figure 4.8 shows many images of tracks revealed in plasma etched halite, with Fig. 4.8(a) providing a diagram of how to differentiate between different pits and bumps detected. These track pits vary in length, due to different energies of nuclear recoils and different angles of intersection to the cleave surface. In addition, these tracks are revealed at a very high density of $\sim 6.8 \times 10^6$ cm^{-2}, as expected for our halite samples. Track pits that appear as small circular pits (Fig. 4.8(a), in red) represent tracks of very small track lengths (tens of nanometers, unetched), and also tracks that are nearly normal to the cleave plane. Track pits that are long and narrow (Fig. 4.8(a), in yellow) represent tracks almost parallel to the cleave plane. Lastly, the comet-shaped tracks 4.8(a), in blue) represent those tracks captured at an angle to the cleave (e.g., 45°to cleave surface). In Figure 4.9(a) the long narrow tracks are portrayed as linear or oval-shaped bumps on the surface, whereas the other tracks - those small and those comet-shaped, appear as pits. These long bumps were originally thought to be purely bumps on the surface due to redeposition, but skepticism arose because there was not an explanation for the highly linear nature of what should be random deposits. However, after closer analysis, we realize that these are in fact tracks, but they are sandwiched between two linear redeposition bumps synonymous with the length and direction of the track (Fig. 4.9(c)). This not only explains the

highly linear nature of deposition bumps on the surface, but also explains the double-lined pits imaged frequently across samples (Fig. 4.9(c). This phenomena is due to the resolution of the LCM and the height of redeposition bumps on the sides of these tracks. The Keyence VK-X1000 raster scans across the surface of minerals, and at each pixel (actual length between pixels depends on magnification) it averages an intensity signal from the laser. If the track width is smaller than the resolution in the XY plane, then we will not actually detect a pit. We will get an average value between the two redeposition bumps, resulting in the phenomena pictured in Fig. 4.9(a). In addition, plasma etching will never be purely isotropic across the sample due to the simple probabilistic nature of kinetic etching. If some in-plane tracks were etched more than others, we would see some appear as purely bumps (too much redeposition to distinguish bump from pit) or in some cases we can resolve the track, which is exactly the case. Due to this readout limitation, the diameter of these in-plane tracks cannot be accurately measured. However, for tracks lying in plane, only the track length is of interest, and the track length can still be accurately measured in this manner.

A diagram representing track geometry on the surface based on angle is shown in Figure 3.3, and actual profiles of tracks at different angles to the surface are displayed in Appendix Section B, Figures B.5, B.6, and B.7. These different geometries are also visualized in a depth map in Figure 4.9. Tracks are randomly oriented and scattered in a 3-D crystal, but when we cleave this crystal, we are only capturing a 2-D representation of tracks as they lie in the plane. Most of the time, these are partial track lengths.

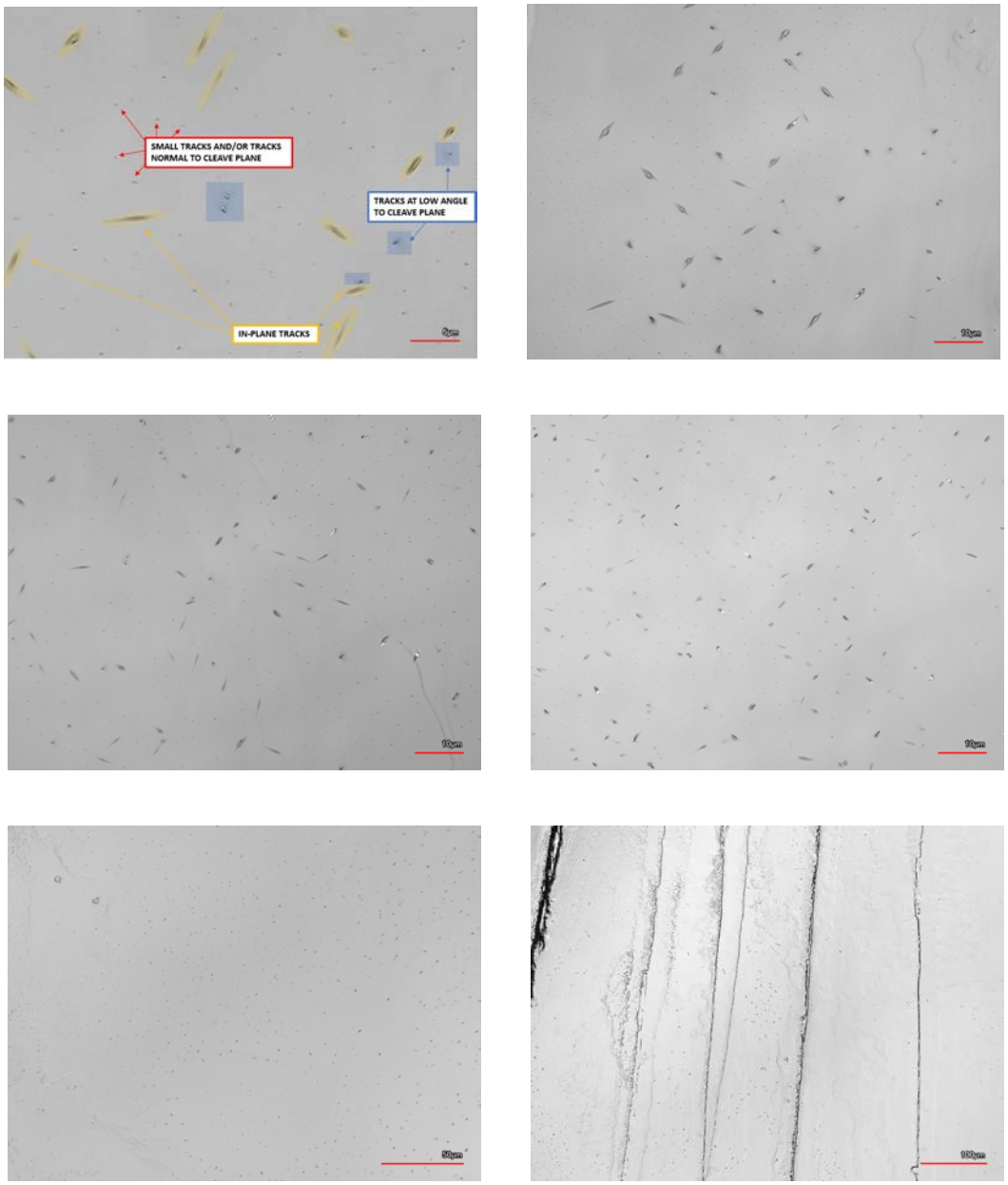

Fig. 4.8: Schematic diagram (top left) and various images of nuclear recoil tracks in halite, etched with argon plasma at 100 W/0.2 mbar/10 minutes. Imaged with the Keyence VK-X1000 at MSERF.

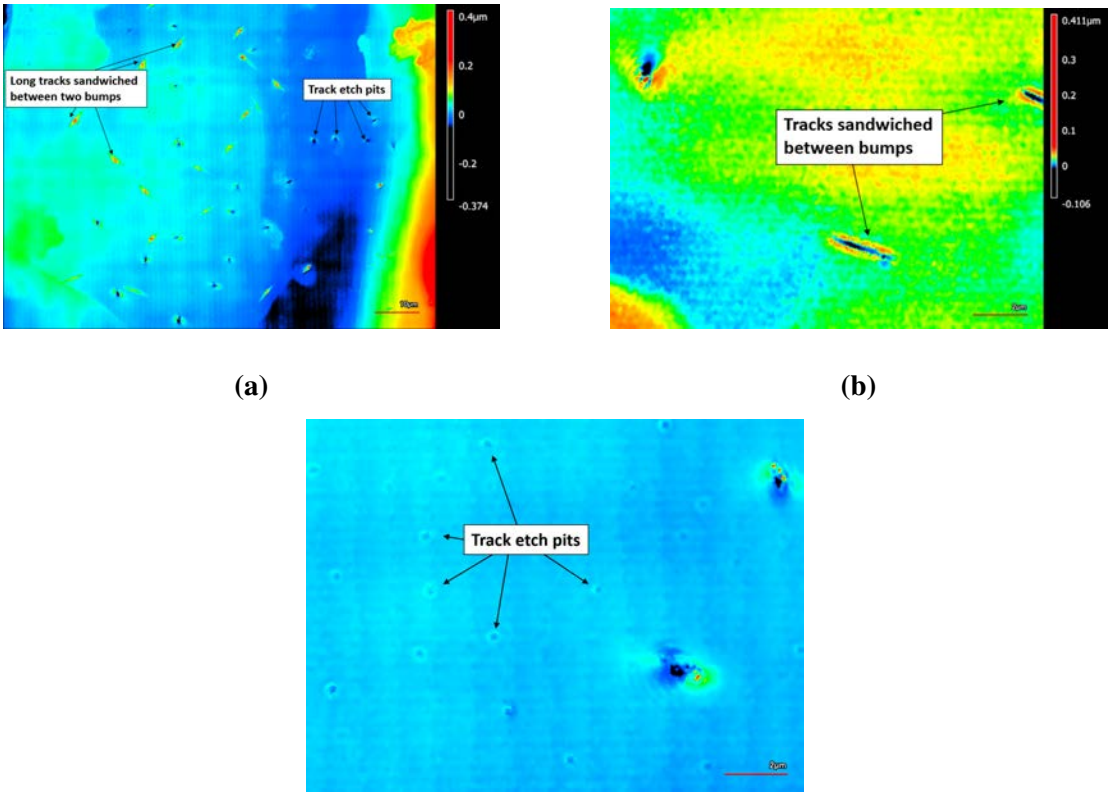

(a) **(b)**

(c)

Fig. 4.9: Depth maps showing tracks appearing in plasma etched halite (100 W/0.2 mbar/10 minutes). Imaged with the Keyence VK-X1000 at MSERF at a magnification of 150x.

Because of the ambiguity introduced due to track angle to the surface (disregarding in-plane tracks), the measured length of a track is then instead the *minimum* length of the track. For very small pits (Fig. 4.9(b)), we can use an aspect ratio (diameter versus depth) to determine whether these tracks lie closer to parallel to the plane, or normal to the plane. The aspect ratios for comet-shaped, large tracks in halite (Fig. 4.9(a)) range between 0.015 - 0.215 and the mean aspect ratio is approximately ~0.055. Whereas the mean aspect ratios for very small tracks (Fig. 4.9(b)) range between 0.00607 - 0.241, with the mean aspect ratio being ~0.04. Based on Ref. [14], we consider an aspect ratio of less than 0.05 to be parallel enough with the cleave that the visible length of the track can be considered accurate. This aspect ratio threshold checks that the depth of the pit is 5% or less of the etch pit diameter. This standard can be changed as more experimental data is collected and limitations of our readout method are better understood. An aspect ratio greater than this value implies the track is too angled to get an accurate read on the true length, and it is instead considered a partial track. The aspect ratios between all measured tracks are plotted in Fig. 4.10. Most of our measured tracks fall underneath our threshold of 0.05. The tracks we will use to compare against theoretical spectra will only include those under the aspect ratio threshold.

All measured *etched* track lengths detected in halite are plotted in Figure 4.11. The next step is to calculate an etching rate for plasma etched halite, and convert these track lengths to approximately their original value. To measure the etch rate of halite, we monitored the depth of preexisting pits and the height of crystal plane edges over

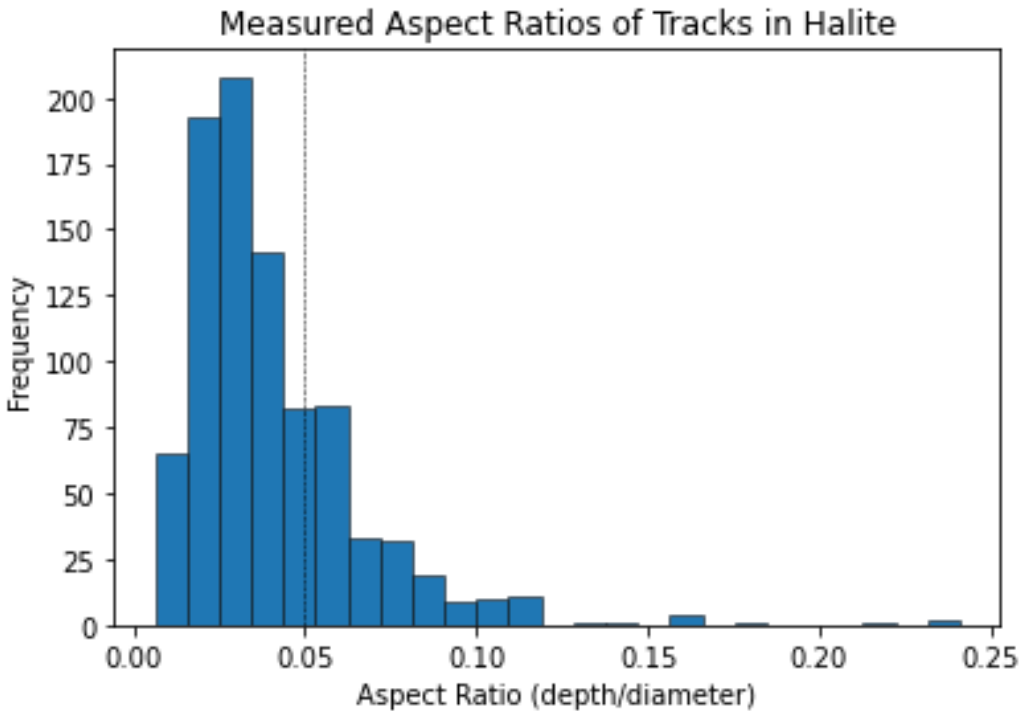

Fig. 4.10: Aspect ratio of measured tracks in plasma etched halite.

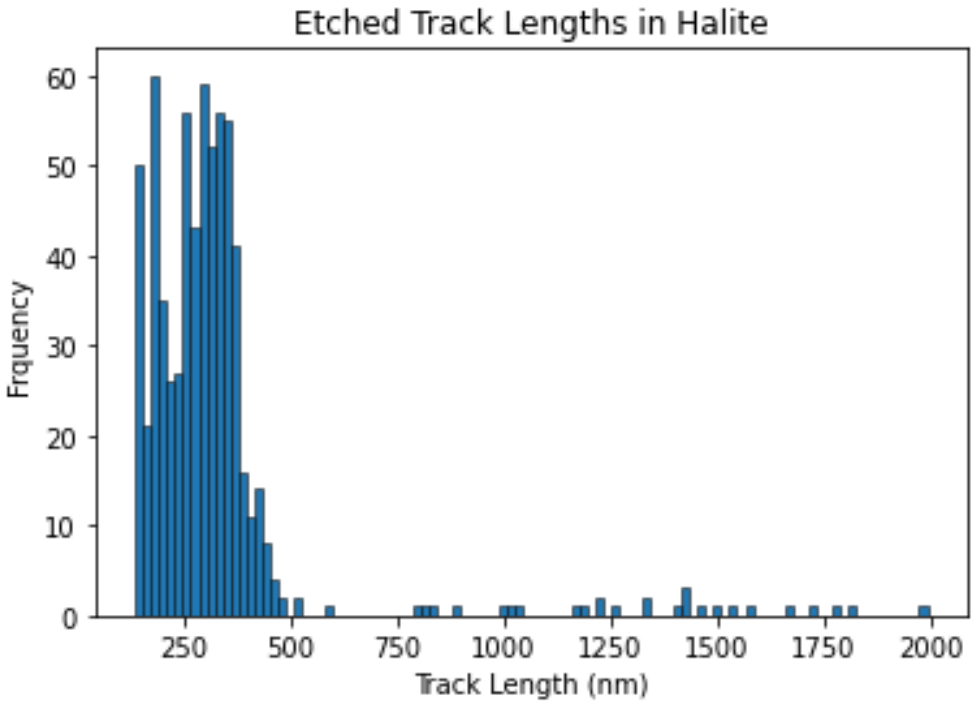

Fig. 4.11: Histogram of all etched tracks measured in halite, under the aspect ratio threshold of 0.5.

etching time, imaging the surface before and after etching. Plasma etching, being a kinetic-based process, will not be as homogeneous as chemical etching. We calculated an average etch rate of 14.47 nm/min in defected regions of halite surfaces. It is important to note that preferential etching will not only occur in defected areas of the surface but also within the defects themselves. This average etching rate also does not take into consideration the general etching rate of the surface. However, this may be negligible, as the root mean squared roughness of the *non-defected surface area* before and after etching was calculated to be approximately 2 nm and 3 nm respectively, implying that plasma attacks pristine crystal surfaces of halite very little at this power and pressure.

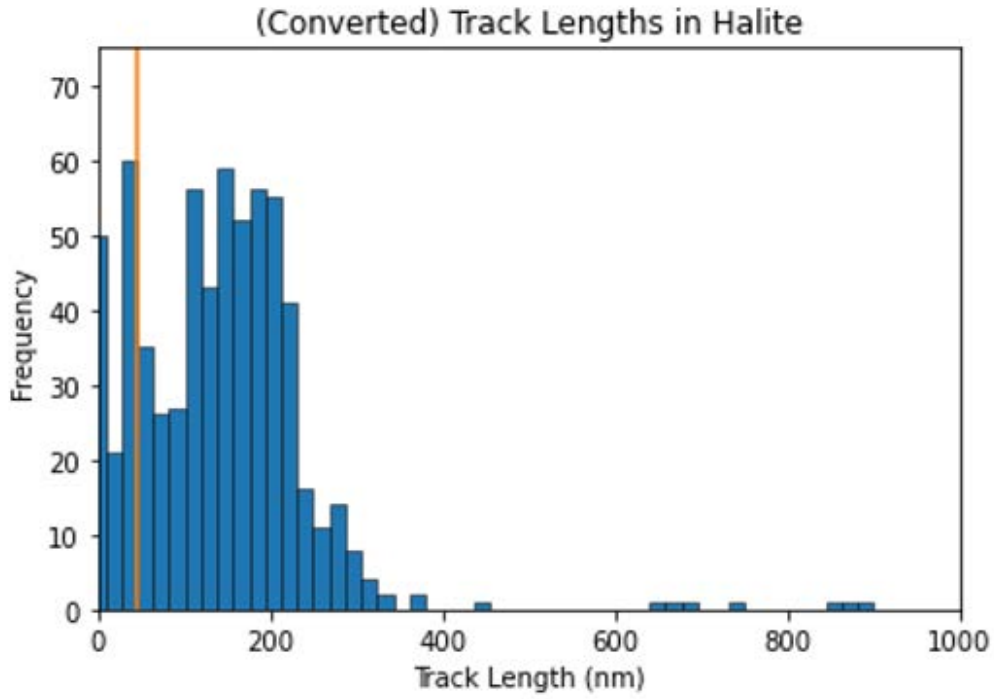

Fig. 4.12: Histogram of track lengths measured in halite (converted to approximately their original value with an average etch rate of 14.47 nm/min). Orange line represents characteristic track length of $U^2 38 \rightarrow Th + \alpha$ decay.

Converting our etched track lengths to approximately original track lengths using our measured etching rate, and only taking into account tracks of lengths 1 - 1000 nanometers, yields the signal displayed in Figure 4.12. The density of tracks lying within the plane, measured under 1000 nm, is $\sim 4.26 \times 10^6$ cm^{-2}. Now that we have collected and reconstructed track lengths in halite, the next step is to develop the theoretical track length spectrum for the mineral and fit the distribution to experimental data.

The theoretical track length spectrum of halite is computed based on chemical

composition, predicted background signal flux, and estimated uranium content of 0.01 ppb for a marine evaporate. This spectrum can be seen in Figure 4.13. The interaction rate is a function of track length, mass of the target mineral (in kg), and the exposure time, or mineral age, (in Myr). It is important to note that we do not truly know the magnitude of these background signals until we collect experimental data specific to a target mineral. Additionally, as visualized in Fig. 4.13, the neutron and Th-α peak are *theoretically* the most dominate of the backgrounds. Thus we can consider those to be dominating the *behavior* of experimentally collected track length distributions. Due to these unknown factors, the next step is to *fit* our theoretical spectrum to our experimentally measured data and overall determine the efficiency of track measurement in halite as well as a characterization of backgrounds existing in the mineral. To do this, we can create a mathematical model of theoretical background signals that shows the behavior shown in experimental data collection, and determine the goodness of the fit between the actual experimental data. This theoretical fit will eventually lead to a determination of background components of the mineral.

There are a variety of unknown variables that we will need to solve for before integrating over the theoretical spectrum and directly comparing track counts. We first can plot the neutron and Th-α signals on a linear scale to see how their functions will dominate experimental track collection (Fig. 4.14). In Figure 4.14 there is an underlying exponential form attributed to the neutron background, with an overlaid Gaussian distribution that we have modeled to represent the Th-α peak. The neutron background,

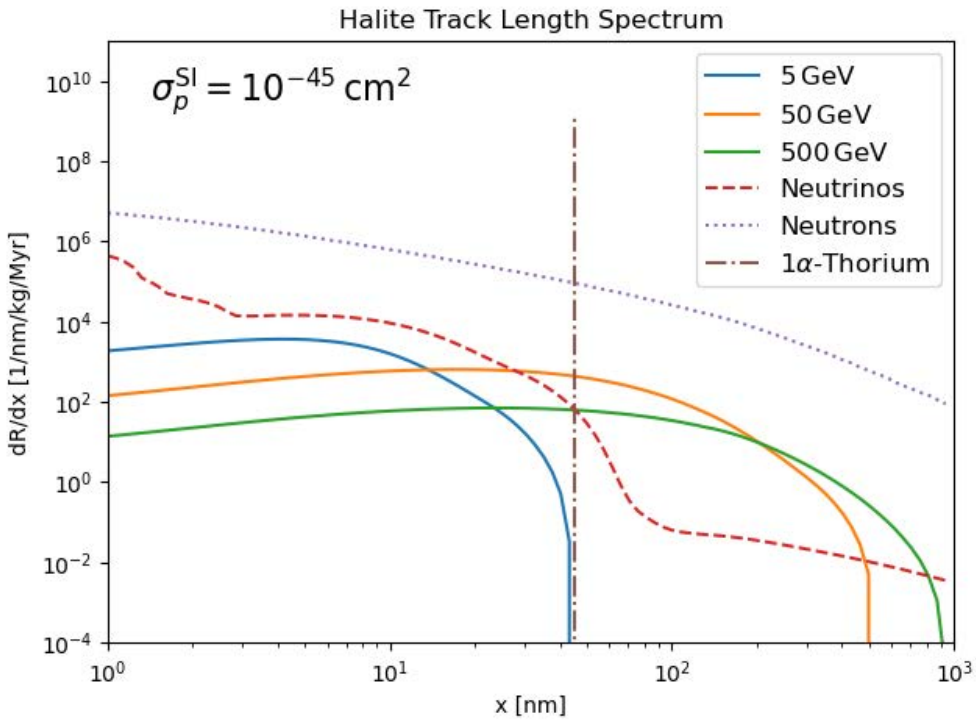

Fig. 4.13: Plot of the theoretical track length spectrum of halite, represented as an interaction rate dependent on track length (nm), target mass (kg), and exposure time (Myr). Blue, orange, and green solid lines are dark matter of masses of 5, 50, and 500 GeV. Red dashed line is all background and target neutrino signals (including CC SNe). Purple dotted line is the spontaneous nuclear fission background from the surrounding radioactive environment. Brown dotted-dashed line is the characteristic 72 keV decays of ^{238}U $\rightarrow$ ^{234}Th+α at a track length of ~45 nm.

taking an exponential form, has an unknown *amplitude* and unknown *rate of decay* (β). We know that at track lengths *greater* than the Th-α characteristic track length of ~ 45 nanometers, the neutron background will dominate over all other backgrounds. We can then use the tail of experimentally measured data (Fig. 4.12 at tracks lengths greater than $\sim$ 200 nm) to determine approximately what the *amplitude* of the neutron background is. In addition, we have chosen a Gaussian form to represent the Th-α peak versus a peak at a singular track length (as visualized in Fig. 4.13) because theoretical predictions have not taken into account slight variations of this characteristic track length due to partial annealing, partial track length measurement, channeling, unequal etching rates, error in etching rate calculations, and any other effects. There are three unknowns attributed to the Th-α Gaussian distribution: the *width* (σ), the *amplitude*, and the location of the peak (x_0). Lastly, there is an overall magnitude to the combined neutron and thorium backgrounds that will be another missing variable in our mathematical model.

Experimental data, in Figure 4.12 shows an exponential-type growth of track signal as we approach smaller track lengths, until we hit roughly 200 nanometers. We also see a peak in track signal around 45 nanometers, which is highly likely to be attributed to the Th-α peak predicted in theoretical studies (Fig. 4.13). Theoretical data, in Figure 4.14, predicts an overall increase in track signal as we approach smaller track lengths, with a large peak attributed to the uranium decay chain. Comparing the two, we find the experimental track length spectrum (Fig. 4.12) shows a behavior broadly similar

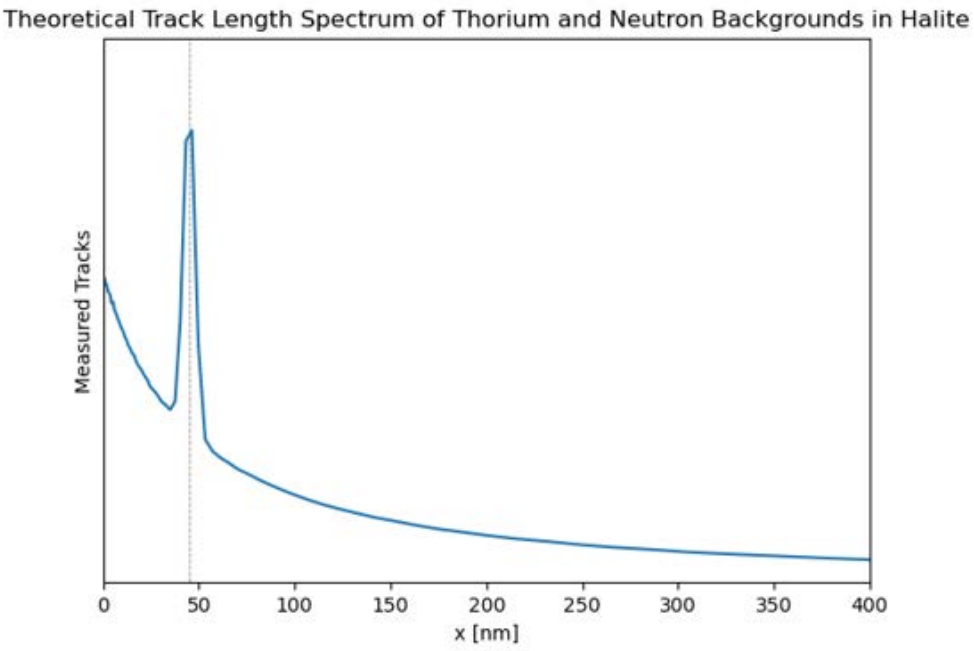

Fig. 4.14: Linear plot of the neutron and Th-α peak background signal, with an unknown amplitude.

to theoretical predictions, but has some sort of track signal suppression at track lengths smaller than $\sim$ 200 nanometers. We assume the phenomena happening at tracks lengths less than $\sim$ 200 nanometers can be attributed to a variety of experimental efficiencies. These efficiencies could include limitations from resolution of our readout technology, limitations from the optical properties of halite, errors in etching rate measurement and conversion, limitations of the automatic track detection code, and more. These efficiencies exist at all measured track lengths, however they **dominate** at track lengths less than $\sim$ 200 nanometers. We can add an *efficiency equation* to our mathematical model to represent this suppression of track signal seen in experimental data. The efficiency equation can be best represented as a Sigmoid function, with the slope of such a function being an additional fit parameter .

We can then tie together all of our discussed functions and create a mathematical model that represents the dominating neutron and Th-α backgrounds, along with an efficiency function:

$$\frac{1}{1+e^{-c(x-d)}} \times A\left[Be^{-\frac{1}{2}\left(\frac{x-x_0}{\sigma}\right)^2} + e^{-\beta x}\right] nm^{-1}kg^{-1}Myr^{-1}, \tag{4.1}$$

where c is the slope of the efficiency function, d is the position of 50% efficiency on the x-axis, A is the overall normalization of the thorium and neutron backgrounds, B is the amplitude of the Th-α peak, σ is the width of the Th-α peak, x_0 is the position of the Th-α peak on the spectrum (what track length it is centered on), and β is the rate of decay of the exponential neutron background. Plotting this mathematical model with our best qualitative variable fit results in the graph behavior seen in Figure 4.15. As you

can see in Figure 4.15, the mathematical model we have developed is showing a similar behavior to our experimentally collected spectrum. The next step is to determine the best fit variables for our mathematical model.

All of these variables can be fit to match our experimental spectrum by essentially iterating through many different combinations until we find the best fit. The best fit can be determined by a goodness of fit test - we are specifically using the chi-squared goodness of fit test. The process of deriving these variables involves first iterating over a range of values for each variable, integrating over the mathematical model (theoretical track length spectrum) for every given variable combination, and then comparing the track count at each length range with the experimental track count at the same length range. We cannot directly compare track counts (experimental data) to an interaction rate (theoretical data), therefore integrating over the theoretical track length spectrum and allows us to plot theoretical track counts as a histogram. The integration bounds are determined by the binned track length ranges in experimental data, in Figure 4.12. The chi-squared test allows us to determine the *goodness* of the fit between our mathematical model and experimental data using the following equation:

$$\chi^2 = \sum_{i=1}^{N} \frac{(\text{Theoretical Track Count}_i \; - \; \text{Experimental Track Count}_i)^2}{\text{Uncertainty}_i^2}, \tag{4.2}$$

where χ is the chi-square test statistic, N is the total number of bins, and *uncertainty* is the uncertainty of the experimental counts. As this is a counting experiment of a rate process we use Poisson's error bars of the measured counts. The variable combination where χ^2 is at a global minimum represents the **best fit for our mathematical model**.

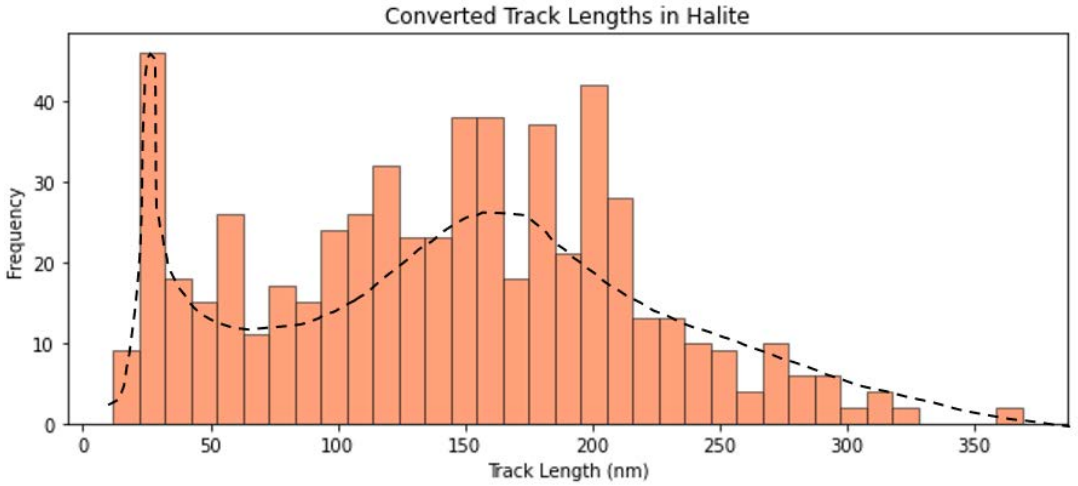

(a)

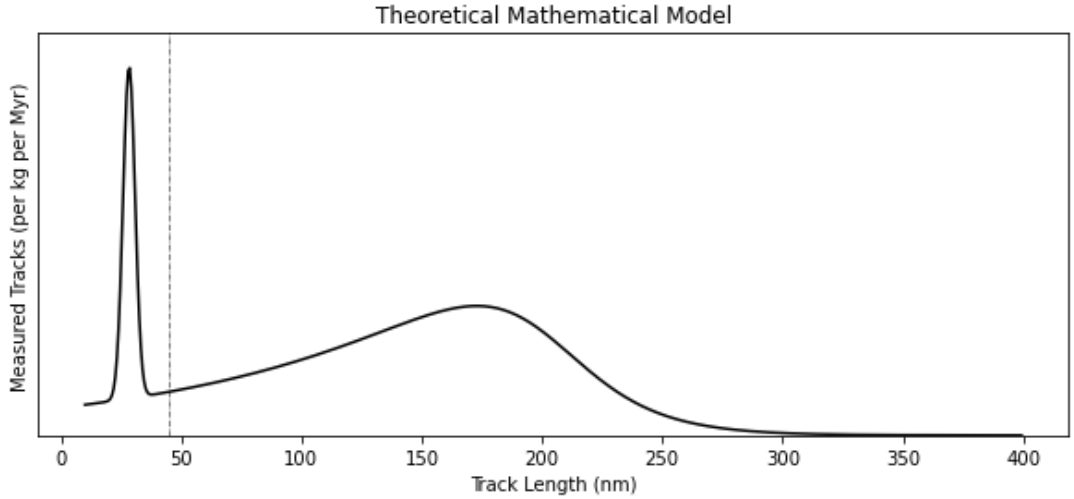

(b)

Fig. 4.15: Plot of (a) experimentally collected track lengths in a histogram, and (b) qualitative representation of the mathematical model in Eq. 4.1

There are additional steps needed between integration and the calculation of the chi-squared test statistic to prepare the theoretical track counts to be fit against experimental data. The first is to convert the theoretical spectrum to be a function of target sample area (surface density), and not mass (volume density). Because we are only measuring tracks in a single plane of halite, we can never truly know the volume density of tracks without using a volumetric readout technology. However, we can estimate this if we assume that track density and length distribution is uniform throughout the crystal. The theoretical spectrum is a function of target mineral mass, and we can use the mass density of halite (0.00216 kg/cm^3) to convert the units of kg into cm^{-3}. Once the units are converted, we can take the cube root of the measured track count per volume, and then square it to get an approximate track count per area. We opted not to manipulate experimental data in any way not necessary to preserve as much information as we can about the mineral.

The interaction rate of our theoretical track length spectra is also a function of exposure time (or mineral age, in the absence of thermal annealing). The ^{234}Th+α decays have a set energy of 72 keV, corresponding to a track length of approximately 45.37 nm in halite [5]. We have detected track lengths between 1-1000 nanometers, therefore some fraction of these tracks are induced by ^{234}Th+α decays, however we do not know the true density of these tracks because the signal at this track length is suppressed by the efficiency function (Eq. 4.1), and further some ratio of tracks within this length range will be attributed to the neutron background. The amplitude values

derived as part of our mathematical fitting should approximate how many alpha-recoil tracks are present in our sample and furthermore what we have theoretically not been able to detect due to our efficiency function. Once our mathematic model is fit, we can estimate an exposure time.

Due to the enormous amount of computations needed to derive the missing variables from our mathematical models, we will be computing them through Python. The specific script used to iterate through variable combinations can be found on my GitHub page. Our script iterates through a range of variable possibilities for all seven variables at once, resulting in $\sim 10^7$ different chi-square test statistic calculations, corresponding to all of the different combinations of variables. The minimum chi-square test statistic amongst all of these calculations will then produce our best fitting variable combination and allow for the progression of data analysis. Ideally, the chi-square test statistic should be equal to or less than the degrees of freedom in the model. In our case, the degrees of freedom is determined by the overall number of bins (track length ranges) we are comparing data in, minus the number of unknown variables. The results in a degree of freedom of 28 in our studies. Therefore, our chi-square test statistic should aim to be around or less than this value. After we have derived our minimum chi-square test statistic, the value will test us what the p-value is for the fit. The p-value is a measure of probability. Assuming our theoretical model in Eq. 4.1 represents the true physics of the nuclear recoil track backgrounds, the p-value is the probability that we would measured a chi-square test statistic as large or larger than what we have found. For

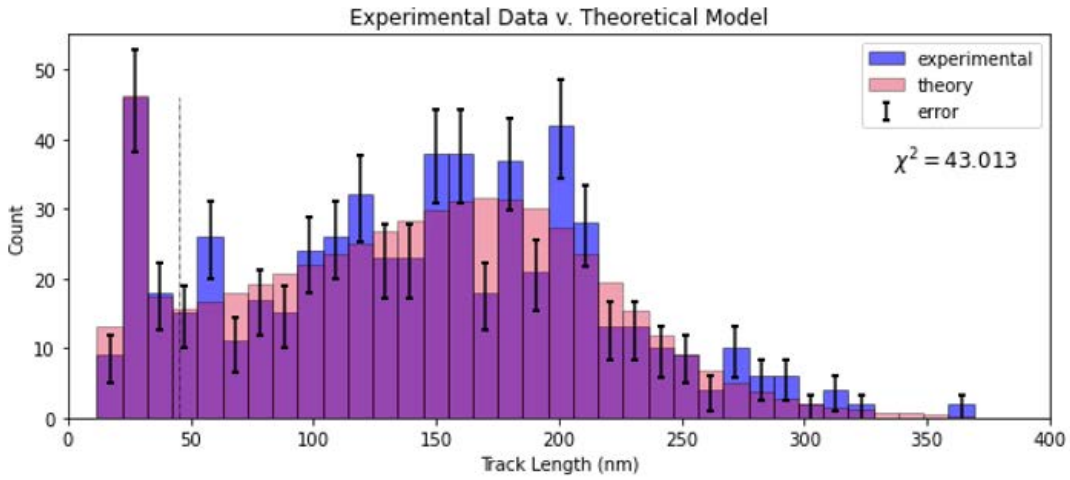

Fig. 4.16: Experimental data (blue) overlaid with our theoretical mathematical model (pink) with variables determined by the minimum chi-square test statistic derived, 43.013. Error bars are computed based on Poisson's fluctuations.

example, a chi-square test statistic that equals the degrees of freedom in our model (28) equates to a p-value of 0.4644. This means that we would have a 46.44% probability of measuring a chi-square of this value or greater. This would imply that our theoretical model is a good fit to our experimental data. A chi-square less than this value would increase our probability and increase the goodness of the fit.

After computing upwards of 12×10^6 variable combinations, the lowest chi-square test statistic we were able to derive is 43.013, corresponding to a p-value of ~3.5%. The theoretical track counts compared to the experimentally collected track counts can be seen overlaid in Figure 4.16. Visually, the functions in Fig. 4.16 are starting to approach a good fit. A chi-square around 40 is a decent fit to data, although in the future, with more experimental data collected, the variables can be tweaked and

thus the chi-square value can continue to decrease and improve our fit. For our research this is the best fit we could derive, but it should not represent the final fit. The variables derived from this chi-square fit substituted into Eq. 4.1 are as follows:

$$\frac{1}{1+e^{-0.055(x-200)}} \times (6.18 \times 10^5)\left[(2.55 \times 10^6)e^{-\frac{1}{2}\left(\frac{x-28}{2.5}\right)^2} + e^{-0.0449x}\right] nm^{-1}kg^{-1}Myr^{-1}. \tag{4.3}$$

An estimate of an exposure time for the mineral is quite sensitive to the efficiency function. This means that even a slight change in the neutron background could significantly change the fit of our mathematical model. As of right now there is a lot of uncertainty in this efficiency function - which directly impacts the alpha-recoil track density needed to derive an exposure time. To minimize this uncertainty, future work could determine an accurate age of our sample through alternative methods - like nuclear irradiation - and use this age to constrain the efficiency function within a known range. This constraint in the efficiency function would significantly narrow down the possibilities for other variables, ideally giving us a better overall fit to the data. Due to time constraints this is not an analysis we can afford as part of this thesis research, but determining the next steps in the future work is still valuable. We can understand the behavior of our data, and how to relate it to theoretical work. Yet there needs to be extensive study into the mathematical modeling portion of this research to refine our variables. Once these variables are within good estimation, then experimental data can be directly compared to theoretical track counts in halite. Theoretical models pub-

lished by Refs. [5, 15, 16, 18, 19, 20] can be elaborated on to better understand the background influence in paleo-detector minerals.

4.2 Muscovite Mica Track Detector

The unetched surface of mica was imaged and analyzed with the AFM and LCM prior to any etching experiments. Across pristine areas of the sample, no surface defects were measured and the average RMS roughness was 0.17 nm, aligning well with studies analyzing natural unetched mica [14, 36, 37, 46]. Before any individual sample of mica was etched, it was first surveyed under the LCM (and ocassionally the AFM) to ensure a proper analysis of features appearing after etching the sample.

We first attempted to etch Muscovite mica with an aqueous solution of sodium hydroxide (NaOH). Following previous experiments, we used a 6 mol aqueous NaOH solution maintained at 70 °C ± 1 °C [25, 56]. The temperature of the solution was maintained using a heated water bath. Mica samples were cleaved with scotch tape, then immediately placed in the hot solution, and etched for 45 minutes, 1 hour and 2 hours. Afterwards, samples were cleaned with deionized water in an ultrasonic water bath for a minute. There were no tracks or etch pits observed in the mica samples under the Keyence VK-X1000 laser confocal microscope. Some samples showed evidence of possible NaOH crystal precipitation on the surface, but otherwise there were no significant changes to the mica surface. This experiment was repeated numerous times with new solutions of aqueous NaOH and tracks were not revealed either time. There

are additional studies that use a boiling aqueous NaOH solution to reveal tracks in Muscovite mica over 24 - 48 hours, but unfortunately we did not have the required observation protocol or equipment to conduct such an experiment [25, 56].

To avoid the use of hydroflouric acid etching, we then considered alternative routes of etching mica, like dry etching. Reference [14] details an experiment that reveals alpha-recoil tracks with an AFM by means of RF-discharge argon plasma etching. The revealed tracks are consistently oval- and comet-like in shape, with dimensions listed in Table 4.1 [14]. Track densities of $10^5 - 10^7$ cm^{-2} were found across samples of mica [14]. Following Ref. [14], we used the Deiner Pico plasma cleaning system (located in Lab 50/1522) to sputter etch our Muscovite mica samples with argon plasma. Although a kinetically-driven and theoretically isotropic process of etching, at the proper power and pressure, the ions will preferentially etch low-energy localities - or in other words, crystal defects - on the sample surface. At too high of a power, the plasma will erode the surface too significantly to see defects. The plasma cleaner uses a radio frequency discharge of 13.56 MHz to ionize argon gas, up to a maximum power of 100 W. At first we attempted to replicate Ref. [14]'s results by using a equivalent power and pressure of 20 W and 50 mTorr in our experiment, but the plasma cleaner system is not equipped to handle such low pressures. Instead, we chose to set our power to 50 W and pressure to 150 mTorr (0.2 mbar). We followed the study's etching time of 10 minutes in our experiment.

The initial plasma etched sample was imaged under the AFM and LCM, and did

α-recoil Track Measurements in Muscovite Mica		
Depth (nm)	**Short-axis (μm)**	**Long-axis (μm)**
20-50	0.7-2.0	1.2-2.7

Table 4.1: Alpha-recoil track dimensions measured using plasma etched mica from Ref. [14]. In Ref. [14], Muscovite mica was etched at 20 W and 50 mTorr (0.0667 mbar) for 10 minutes.

not reveal any etch pits. It is likely that the power of the argon plasma was too low, coupled with the higher pressure, to etch the surface enough to reveal tracks. The R_q of our unetched mica is 0.17 nm, whereas the R_q of 50 W/0.2 mbar/10 min. plasma etched mica is 0.38 nm. Roughness was measured with the AFM and Gwyddion software. Ref. [14] reports a before and after etching root mean square roughness of 0.15 nm and 7 nm (also measured with an AFM). Noting this difference, we increased plasma power in future experiments.

In the next plasma etching experiment, the plasma power was increased to 100 W, and the pressure and time were kept at 0.2 mbar and 10 minutes. The samples were first observed optically under a standard light microscope, and very faint features could be observed on the surface, but nothing could be conclusive until we imaged the features with a high resolution laser microscopy. The samples were taken to MSERF to image under the LCM, and etch pits were indeed revealed.

The success of the 100 W plasma experiment initiated many more replicated

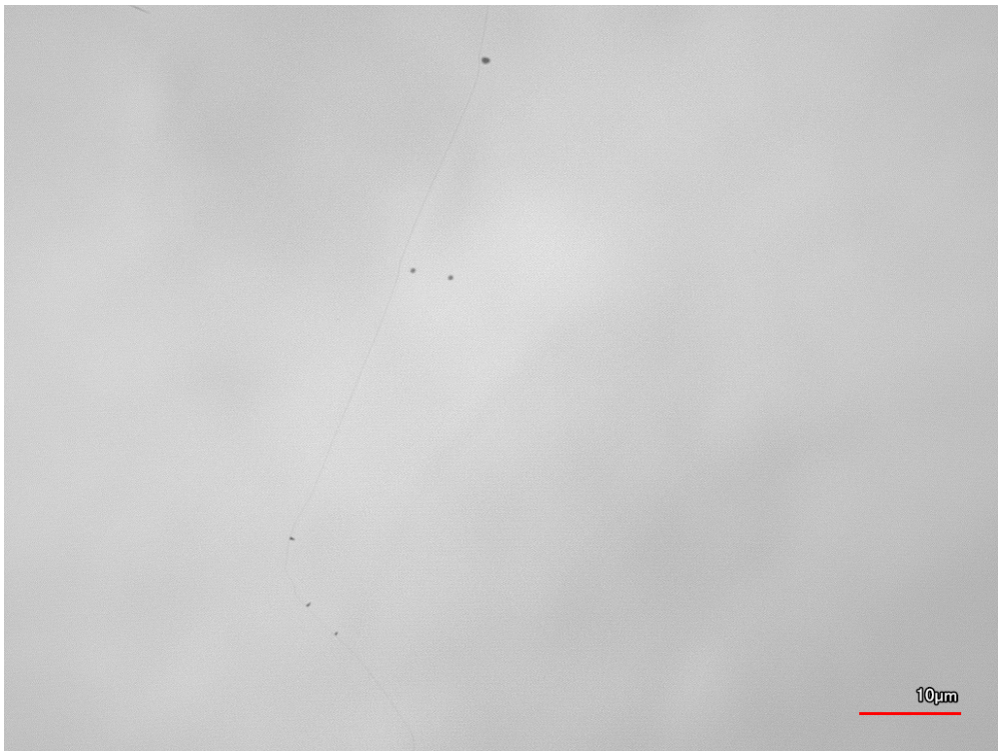

Fig. 4.17: Etch pits appearing on and near a chunk of atomic steps on Muscovite mica. Sample was etched at 100 W/0.2 mbar/20 min. with argon plasma using the Deiner Pico plasma cleaner system.

experiments using Muscovite mica, at various etching times. All images of areas with etch pits were taken at a 150x magnification, and after weeks of imaging all data was compiled for all mica samples. The next step was to verify that any or all etch pits are nuclear recoil tracks. In Ref. [14], is it not clearly stated, but it is implied that the tracks identified are only tracks lying within the cleave plane of mica, explaining the consistent comet-like shape and dimensions observed[1]. In addition to consistent geometry, the mean aspect ratio of tracks identified in Reference [14] was ~0.022. This value is incredibly close to in-plane tracks identified in halite, therefore we can compute the aspect ratios for etch pits identified in Muscovite mica to gain more information about etch pit/track orientation.

Etch pits arising from natural crystal defects in mica can be isolated and removed from collection with a careful review of previous literature studying these defects through chemical etching. Point defects in mica, being only the size of missing atoms in the crystal lattice, will likely not even be within our resolvable range with the LCM. Etch pits arising from dislocations, the most common defect-induced etch pits that will arise in mica, will be difficult to distinguish from tracks at our current resolution with the LCM [78, 79]. However, there are a few characteristics that can make this possible. Screw dislocations, one of the most common dislocations in mica, will initiate at the end of an atomic step [79]. In addition, dislocation etch pits can be

[1] The author of Reference [14] was contacted to further clarify the observations and conclusions noted in the study, but so far we have not gotten a response.

identified with the double etching technique, as under low stress dislocation etch pits will move on the surface of the crystal [77, 78]. Movement of etch pits was observed on the surface of mica - although this occurrence was rare and only observed twice in the dozens of images analyzed, both moving pits were located nearly on an atomic step. There were instances of etch pits on or very close to natural crystal surface defects, like atomic steps or microcracks (an example is shown in Fig. 4.17). It is likely these etch pits arise from natural crystal defects, like dislocations or vacancies that are in itself spawning the atomic step fracture during cleaving, therefore any etch pits lying on preexisting defects were not included in the counting of track etch pits. Any pit-like structures existing before etching within the dimension range of interest were noted and not counted in the study, as the sample was surveyed before any etching. Any etch pits that were on or near atomic steps or cracks were not counted in our track density, to ensure the improper identification of a nuclear recoil damage track as these pits will be within the length range we are detecting. Furthermore, all images included in the track count were etched and imaged in multiple rotations, and only spontaneous, isolated etch pits were counted.

The spontaneous etch pits (pits that arise randomly, and not due to or near visible preexisting defects) observed are circular and oval in nature, and fall within the dimensions noted in Ref. [14]. We assume these etch pits are indeed tracks, as they do not fit the profile of natural crystal defects and were not visible prior to etching. Ideally tracks used in analysis will lie within or at low angles to the cleave plane of

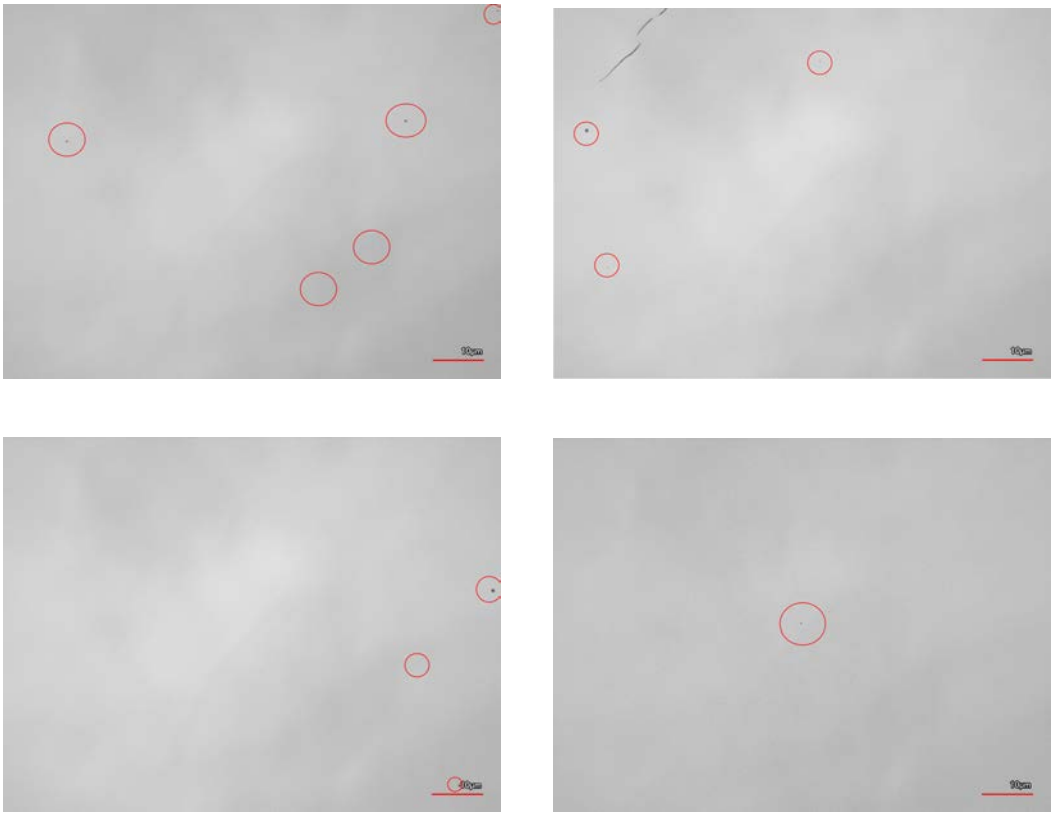

Fig. 4.18: Various laser images of nuclear recoil track etch pits detected on plasma etched Muscovite mica, circled in red. Imaged with the Keyence VK-X1000 at MSERF at 150x magnification.

mica based on aspect ratio calculations. The mean aspect ratios for identified pits in Muscovite mica ranged from 0.017 - 0.22, with a mean aspect ratio of ~0.1. This mean value is higher than the results published by Reference [14] (0.022 average for in-plane tracks), therefore if we are identifying nuclear recoil damage tracks, they most likely range at different orientations and angles to the cleave surface. It is also important to note that we have revealed only a small amount of tracks in Muscovite, just under 20 tracks in total. This is not due to lack of scanned surface area. Compiling all research on etched Muscovite mica, we have scanned approximately $3.9 \times 10^6 \mu m^2$ of etched surfaces. Many plasma etching experiments either did not reveal any etch pits, or etch pits we could detect were too close to natural crystal defects on the surface that a clear origin of the pit could not be established - therefore not counted in etching. It is likely that over longer etching time and higher etching powers, more tracks would be revealed. We established some experiments testing this hypothesis, but there is much future work to be done with Muscovite mica.

We consider the long-axis of the oval shaped pits, and the diameter of more circular shaped pits, the track lengths - a collection of full and partial. These track lengths were detected and measured with the automatic track detection code (discussed in Section 3.3) and converted to micrometers/nanometers using the pixel resolution dependent on the image magnification. In Figure 4.19, the track lengths were compiled into a histogram (the area counted for track distribution was approximately 1.2×10^5 μm^2, and we assume the same distribution of track size and density across the sample). The den-

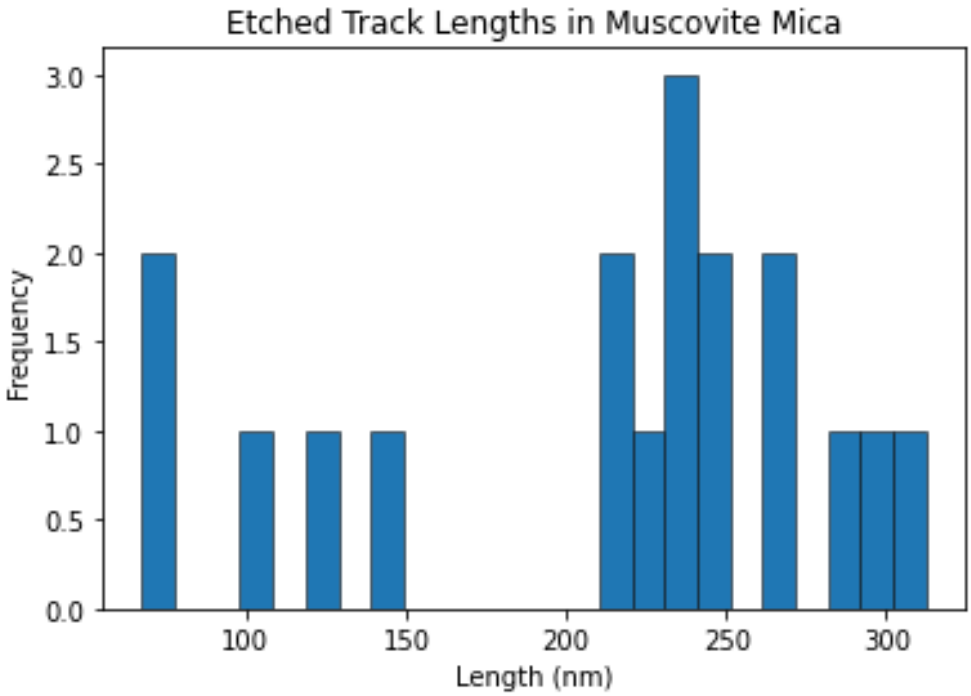

Fig. 4.19: Track lengths detected in 100 W/0.2 mbar argon plasma etched Muscovite mica.

sity of tracks per counted image, which in area was approximately 7.07×10^3 μm^2, ranged from no tracks within an image, to as high as 10^7 cm^{-2}, with an average of approximately 2.5×10^5 cm^{-2} across all surveyed areas. The average root mean squared roughness of 100 W/0.2 mbar argon plasma etched Muscovite mica is 3.14 nm, which is much greater than the roughness measured at 50 W/0.2 mbar plasma etched mica, and closer to the roughness reported in Ref. [14]. Images of some nuclear recoil track etch pits discovered on our Muscovite mica samples can be seen in Figure 4.18.

To further replicate the experiment in Reference [14], we searched for nuclear recoil tracks in plasma etched mica under the AFM. No tracks were revealed, but this

could be due to the sporadic and low density of etch pits amongst our samples. In addition to plasma etching Muscovite mica with the plasma cleaner system, we also attempted to sputter etch and reactive ion etch Muscovite mica. With the Lesker ProLine PVD75 sputter system (Lab 50/1522), we etched Muscovite mica at 20 W/20 mTorr/10 minutes, at the closest pressure we could get to following the 20 W/50 mTorr/10 minute experiment set by Ref. [14]. This experiment revealed no etch pits. We also etched a sample at 50 W/15 mTorr/10 minutes, and no etch pits were revealed. With the Trion Sirus T2 reactive ion etcher (Lab 50/1522), we etched Muscovite mica at 20 W/50 mTorr/10 minutes, following the experimental parameters of Ref. [14]. It is implied that Reference [14] used a sputter etching plasma system, and reactive ion etching should produce the same results, as the bias voltage and ionization power is consistent with the sputter system and the argon gas used is nonreactive to our samples. No etch pits were revealed. Reactive ion etching traditionally gives a much more powerful etch than standard plasma etching, but this etching is directional and will preferentially etch normal to the surface because of the bias voltage involved. This is the case for sputter etching as well.

Once tracks are revealed and measured, we then need to study the etching process of Muscovite mica to reconstruct the original track lengths. To do this, we imaged and measured preexisting defects, such as atomic steps, cracks, and pits, over etching time keeping the power and pressure constant throughout the process. Height information was obtained with the Keyence VK-X1000. After multiple sessions of etching and

Argon Plasma Etch Rates for Muscovite Mica	
$E_{\perp}$ (nm/min)	**$E_{\parallel}$ (nm/min)**
1.5 - 4.4	5.9 – 8.5

Table 4.2: Calculated plasma etch rates for Muscovite mica. $E_{\parallel}$ is the etching rate along the basal plane and $E_{\perp}$ is the etching rate normal to the basal plane. Etch rates were measured and averaged across different samples etched under the same plasma parameters, thus giving the ranges shown in the table.

imaging, we have determined the range of etch rates listed in Table 4.2. Similar to the etching behavior of Muscovite mica in hydrofluoric acid, the etching of mica with plasma is not isotropic [14, 64]. On average, the etch rate along the basal plane of mica is slightly more than the etch rate normal to the plane. Using an average etch rate of 7.27 nm/min along the plane.

Based on our experiments, the smallest track length detected with plasma etched Muscovite mica is approximately 60 nanometers. In order to conduct an analysis of Muscovite mica as a paleo-detector and compare against theoretical predictions, we need to measure tracks through the entire 1-1000 nanometer range. It is important to note that the track length range we provide only serves as a representation of this specific plasma etching method and readout technology. Measurement tools with higher resolution will be more successful at detecting etched tracks in the range of tens of nanometers, as well as more efficient plasma etching conditions revealing tracks of

a lower length. In addition, we have not collected enough nuclear recoil tracks in Muscovite mica to make any kind of conclusion. However, we can still produce a theoretical track length spectrum for Muscovite mica to aid in the future work of this project and make some assumptions about its performance as a paleo-detector.

The theoretical track length spectrum for Muscovite mica is shown in Figure 4.20. The plot models the different background signals that we expect to see in Muscovite mica as an interaction rate, dependent on track length, exposure time, and target mineral mass. The characteristic ^{238}Th α-recoil tracks resulting from the 72 keV decay of ^{238}U to ^{234} are approximately 31 nanometers in Muscovite mica, unetched [5, 15, 16, 17, 18, 19, 20]. These tracks are likely the most dominant source of tracks in most target minerals, but in our case, we have not detected any tracks with lengths less than 60 nanometers. Although this does not present an issue when differentiating dark matter and neutrino signal from background signal, because we would need to neglect this background in order to do so, these α-recoil tracks aid in estimating an exposure time, which greatly contributes to an accurate track analysis.

It is not entirely clear why revealing tracks with plasma etching differs so significantly between Muscovite mica and halite. It could possibly be due to an effect present in micas called *channeling*. This effect essentially limits the range and path of high energy nuclear recoil tracks based on the angle to the mica sheet [80, 81, 82]. Channeling will limit track lengths that are at low angles to the mica sheet (basal plane), and will allow longer ranges of tracks whose angles are close to perpendicular to the

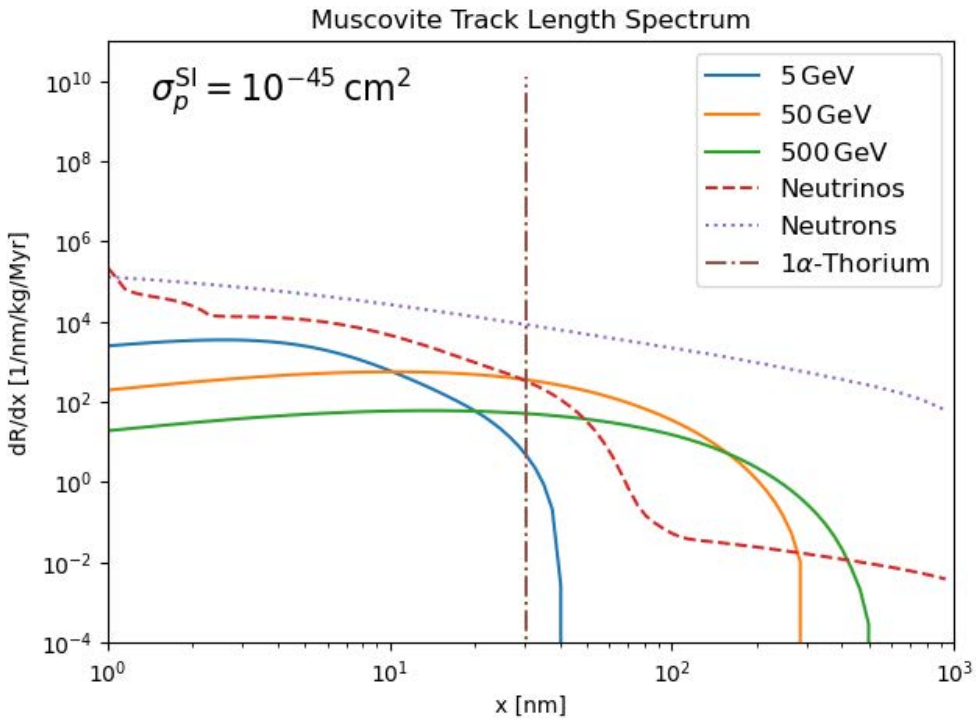

Fig. 4.20: Plot of the theoretical track length spectrum of Muscovite mica, represented as an interaction rate dependent on track length (nm), target mass (kg), and exposure time (Myr). Blue, orange, and green solid lines are dark matter of masses of 5, 50, and 500 GeV. Red dashed line is all background and target neutrino signals (including CC SNe). Purple dotted line is the spontaneous nuclear fission background from the surrounding radioactive environment. Brown dotted-dashed line is the characteristic 72 keV decays of ^{238}U $\rightarrow$ ^{234}Th $+\alpha$ at a track length of $\sim$31 nm.

sheet [80]. In addition, due to the layered nature of mica and the weak interlayer bond energies, nuclear recoils can be re-directed or ”channeled” along a certain crystal plane [81]. The effect of channeling in mica is more prominent for tracks with low angles to the cleave surface, thus the channeling of the tracks redirects them to be more parallel with the basal plane, which would support how Ref. [14] only detected in-plane tracks in plasma etched mica [81]. The result would then be a less random density of track angles, and instead a preferential density of tracks lying within the plane. However, this effect does not necessary inhibit tracks from intersecting normal to the cleave plane. In fact, nuclear recoils will lose less of their energy at this particular angle [80, 81]. At our current stage of research, we are unable to determine whether the tracks detected in mica are only tracks lying within the cleave plane, or a collection of angles - preferentially close to normal or parallel to the cleave. In addition, assuming the pits detected are in fact tracks, we are only seeing tracks of a relatively large length ($>$ 60 nm). It is possible that there are additional track pits being etched on the surface of our samples, but are too shallow to detect with the LCM. It is promising that etch pits are formed on plasma etched Muscovite mica - considering this is an understudied method of etching the track detector - but it is reasonable that it will take time to find the best plasma etching conditions. Lastly, it could not necessarily be the etching or measuring conditions as much as it could just be a lack of exposure time, or mineral age. We do not have accurate information about the age of the mica deposit our samples came from, therefore there is a chance that our samples are simply lacking in exposure time which

would result in a low track density like we've observed.

For future experiments that detect α-recoil tracks in Muscovite mica, and have the ability to determine mineral exposure time, the next step would be to repeat the same process of mathematical fitting as taken for the halite track detector.

4.3 Phlogopite Mica Track Detector

Phlogopite mica is the final mineral we experimented on. We only obtained samples of Phlogopite recently and thus so we have not conducted chemical etching experiments on the mineral. However, Phlogopite can be etched with the same chemicals as Muscovite mica, but often it takes less etching time to reveal tracks [51, 52]. The unetched surface of Phlogopite mica was analyzed with the LCM and showed much of the same characteristics of Muscovite mica, as expected. On an observational level, the cleaving of Phlogopite mica with a razor blade or scotch tape was easier than Muscovite. Under a standard reflection microscope the mineral also shows more diffraction from air and water pockets under the surface. The average measured root mean squared roughness of unetched Phlogopite mica is 5 nm, but this is measured with the LCM. The decreased resolution coupled with the noisy modulations produced by the laser incorporate decent error into this measurement even after proper data processing. The near perfect basal cleavage of micas allows for a very smooth surface, so it is expected that the roughness of unetched micas would be consistent amongst different types.

Phlogopite mica was included in plasma etching experiments alongside Mus-

covite. Knowing the experimental parameters that revealed tracks in Muscovite, we replicated the experiment for Phlogopite at argon plasma conditions of 100 W/0.2 mbar/10 minutes. There were only a handful of tracks revealed in Phlogopite, and it was not enough to conduct an accurate track density and length analysis (Fig. 4.21). The lack of tracks measured is most likely a coupling of less imaging time compared to other minerals, and inadequate etching conditions. Although the two kinds of micas can be etched with the same chemicals, rarely is it for the same concentration and etching time. Thus, it would be a reasonable assumption that the plasma etching conditions for Phlogopite would differ to Muscovite. We expect that the natural crystal defect etch pits arising in Muscovite will also arise similarly in Phlogopite, thus the same procedure and assumptions can be made in the future analysis of etched Phlogopite. In addition, we can follow the same methodology of calculating an etching rate and track volume density as Muscovite.

Even if we cannot compute a detected track density in Phlogopite, we can still produce a theoretical track length spectrum to help guide the future researchers of this project. The theoretical track length spectrum of Phlogopite can be seen in Figure 4.22.

Although we could not conduct an accurate analysis of Phlogopite as a paleodetector mineral due to time constraints, low track density, and lack of literature to guide plasma etching experiments, the mineral warrants further study in the future work of the project. Phlogopite, if under the proper etching conditions *and* if extracted under the same conditions as Muscovite, should contain more tracks than Muscovite and thus

Fig. 4.21: Laser image of plasma etched (100 W/0.2 mbar/10 minutes) Phlogopite mica with a track etch pit in the center. Imaged with the Keyence VK-X1000 at MSERF at a magnification of 150x.

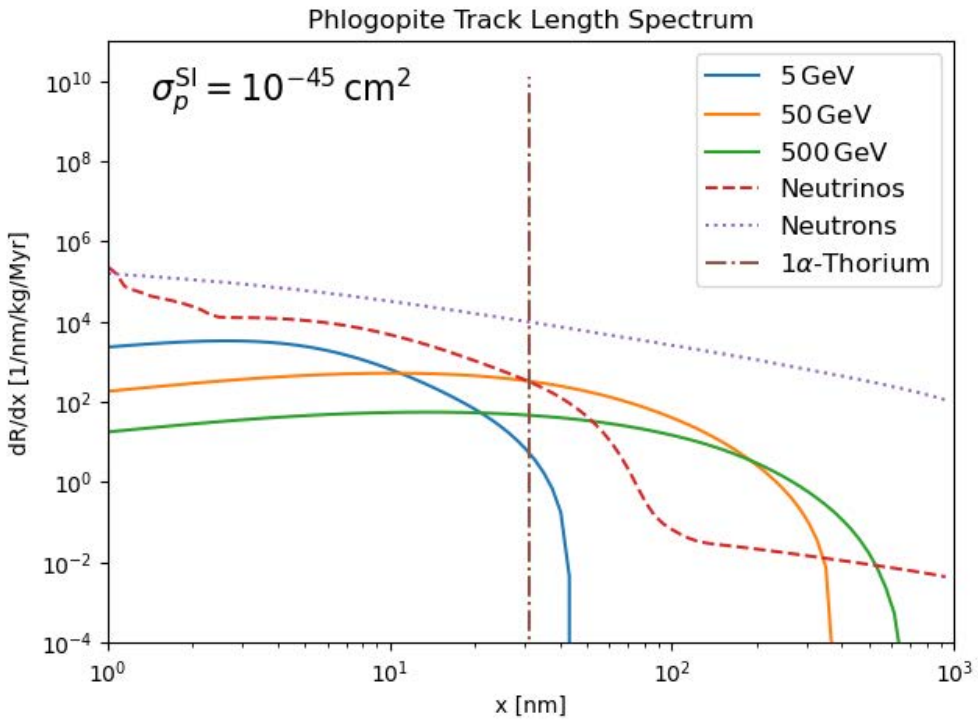

Fig. 4.22: Plot of the theoretical track length spectrum of Phlogopite mica, represented as an interaction rate dependent on track length (nm), target mass (kg), and exposure time (Myr). Blue, orange, and green solid lines are dark matter of masses of 5, 50, and 500 GeV. Red dashed line is all background and target neutrino signals (including CC SNe). Purple dotted line is the spontaneous nuclear fission background from the surrounding radioactive environment. Brown dotted-dashed line is the characteristic 72 keV decays of ^{238}U $\rightarrow$ ^{234}Th $+\alpha$ at a track length of $\sim$31 nm.

statistically speaking, there should be more data collected to increase the accuracy of theoretical track length spectra comparisons. However, as a paleo-detector target mineral, Muscovite could still potentially be preferable, under the right conditions, because of its ability to lower the impact of the neutron background due to larger hydrogen content.

Chapter 5

Conclusion

Our overall goal with this thesis research was to take a theoretical proposal and construct a feasible experimental direction. I believe we have accomplished such a feat. The paleo-detector technique was proposed only a short amount of time ago, and currently is still a theoretical idea with no experimental results to validate it. What we have shown is the ability to take experimental techniques extensively studied in similar research fields, and apply them along with new etching techniques and readout technologies, and produce very promising results. Not only were tracks revealed in all minerals, they were revealed with an alternative plasma etching technique that has not been applied, but once, to solid state nuclear track detector minerals. Plasma etching is relatively fast and nondestructive, and alongside the high throughput of a laser confocal microscopes these techniques present a unique opportunity for quick imaging and analysis. We also present some of the first ever results showing nuclear recoil tracks in halite. In addition to revealing and imaging tracks in these minerals, we have constructed an automatic track detection code that can be applied to any ordinary image of a sample surface. There is minimal user input required and the code speeds up the

identification and measurement of tracks. This code can be continuously improved and modified as this project evolves into more selective and tedious track identification.

One of the goals in this research was to test whether our chosen methodology of chemical/kinetic etching coupled with optical readout methods has the sensitivity to detect track lengths within the ranges needed to differentiate between background and signal. In halite, our methodology is successful at revealing tracks at lengths between 1-1000 nanometers. We have provided the first results of background characterization in halite, a crucial step in advancing towards supernova neutrino and dark matter detection. We have created a mathematical model to relate our experimentally collected track count in halite to the theoretical track length spectrum for the mineral. We have furthermore verified a decent fit of this model using the chi-square test. The mathematical model we have developed yields promising results that help refine the possibility of future work. Mathematical models can vary depending on the target mineral but overall the process of developing a model is consistent and can be applied regardless of the target in this research. This mathematical relationship between experimental and theory produces not only the first experimental results of paleo-detector research, but the first efforts to refine the theoretical studies produced by Refs. [5, 15, 16, 17, 18, 19, 20]. This relationship is a key component of making paleo-detector research experimentally feasible in the future.

Chapter 6

Future Work

Although this research has set a promising precedent for future experimental paleodetector studies, there are many aspects of this research that can be refined and improved in the future. The plasma etching of halite was a successful experiment that we hope evolves into future study using similar methodology. Even though this method is successful, it would be important to replicate another chemical etching experiment using ferric chloride and glacial acetic acid. We originally thought that the specific enchants were not performing properly, but now that it has been discovered to be an accidental acetone/water etch, it opens this possibility up again. The chemical etching of halite would establish a basis for density comparison. If track geometries and densities are consistent amongst plasma and chemical etching, it would further support that the etch pits identified and measured in Section 4.1 are indeed nuclear recoil damage tracks.

Another important experiment that can be included in the future work of this project is the chemical etching of Phlogopite and Muscovite mica with hydrofluoric acid, under the strict advisory and safety conditions of an experienced chemist. There is

an extensive history of etching micas with this chemical, and if it is possible to conduct such an experiment here at the University of North Florida, it will aid in determining the true density of tracks in our mica samples. This density can then be compared to the density of tracks detected in plasma etching micas. Although plasma etching has proven to work, it is not yet determined that plasma etching is revealing tracks, and in addition, tracks intersecting and on the basal plane of mica. Furthermore, our LCM readout technology potentially does not have the resolution to detect the ~30 nm ^{238}U to ^{234}Th tracks revealed with the current parameters of plasma etching. However, HF acid greatly attacks the surface of mica, so pits can be enlarged even more so than the effects of plasma etching. The immense amount of mathematical models developed for HF acid etching of mica will allow for a proper etching rate calculation and conversion. Even if just one hydrofluoric acid experiment is done, we can determine an exposure time of our Muscovite mica sample batch and thus our track length spectra predictions will be much more accurate, lessening the need for a greater number of tracks to be revealed with plasma etching.

In terms of track detection and readout technology, there are many other techniques to pursue that would achieve better resolution, higher throughput, and greater efficiency. Eventually, once a solid basis and characterization is established for our target minerals and tracks, one could evolve to test different readout technology, like the proposed small angle x-ray scattering (SAXs) in Ref. [5]. Argonne National Laboratory (ANL) has a synchrotron source beam line to conduct SAXs. To conduct an

experiment at ANL, one must submit a thorough proposal and reach out to the guiding technician on the project. It is a rigorous and competitive process, but it would be the first project using SAXs to detect nuclear recoil damage tracks. Furthermore, the AFM can be integrated back in as a primary track readout technology if sample surfaces are not too rough, and imaged beforehand to identify the locations and densities of tracks present. The AFM would yield better resolution (atomic-scale) than the LCM, and could reveal more information about the geometry of tracks, but the rendering process is incredibly slow and low throughput (upwards of ~20 minutes to render one image, 20 μm $\times$ 20 μm in area). However, if track locations and densities are known beforehand, the AFM can be used as a follow up analysis to refine track length and dimension. It could also be a useful tool is conducting an accurate etching rate.

The automatic track detection code also has important implications in the efficiency and accuracy of measuring tracks. This code can be improved to automate through multiple images during a single run, and the filtering parameters can be refined to detect tracks of all orientations, ranging from a linear geometry to a point-like circle. Understanding how to filter tracks on geometry is a key component in verifying that one is measuring the true length of a recoil track, rather than partial lengths.

Furthermore, our mathematical model can be better fit to future experimental data by minimizing the chi-square test statistic, and future research can elaborate on the theoretical work by Refs. [5, 15, 16, 17, 18, 19, 20] to refine the theoretical track length spectra for various backgrounds. Due to this field of research being new and

currently understudied, there is much room for theoretical models to be improved. The addition of our first experimental results opens the opportunity to elaborate on this past theoretical research. The addition of new samples of halite with known radioactive concentrations, mineral age, and depth of extraction would significantly help in the improvement of both our experiment and mathematical models. Including new minerals, such as micas, in such an analysis (given the track density is high enough to measure) would elaborate on the applicability of our model going forward as well as report on the feasibility of other paleo-detector minerals.

Lastly, our ability to detect tracks within the full observable (1-1000 nanometers) in halite allows us to set a new upper limit for the interaction cross-section of WIMP dark matter, setting a standard for future paleo-detector research. This limit may not be yet competitive with current direct detect experiments but would set an upper threshold that future experimental paleo-detector work can keep refining.

Bibliography

[1] Dino Aquilano, Fermín Otálora, Linda Pastero, and Juan Manuel García-Ruiz. Three study cases of growth morphology in minerals: Halite, calcite and gypsum. *Progress in Crystal Growth and Characterization of Materials*, 62:227–251, 6 2016.

[2] Gaokuo Zhong and Jiangyu Li. Muscovite mica as a universal platform for flexible electronics. *Journal of Materiomics*, 6:455–457, 6 2020.

[3] Rosenr M Hezen and Cnnnres W Bunnnlvr. The crystal structures of one-layer phlogopite and annite. *American Mineralogist*, 58:889–900, 1973.

[4] Raymond Jonckheere, Carolin Aslanian, Bastian Wauschkuhn, and Lothar Ratschbacher. Some geometrical properties of fission-track-surface intersections in apatite. *American Mineralogist*, 105:1355–1364, 9 2020.

[5] Sebastian Baum, Thomas D. P. Edwards, Bradley J. Kavanagh, Patrick Stengel, Andrzej K. Drukier, Katherine Freese, Maciej Górski, and Christoph Weniger. Paleo-detectors for galactic supernova neutrinos. *Physical Review D*, 101, 6 2020.

[6] John F. Beacom. The diffuse supernova neutrino background. *Annual Review of Nuclear and Particle Science*, 60:439–462, 11 2010.

[7] *Keyence VK-X1000 Series User Manual*. KEYENCE.

[8] *Dimension 3100 Manual*. Veeco Instruments Inc., 2004.

[9] Ricardo Garcia and Rube Perez. Dynamic atomic force microscopy methods. *Surface Science Reports*, 47:197–301, 2002.

[10] Alexander De la Vega, Alice C. Quillen, Jeffrey L. Carlin, Sukanya Chakrabarti, and Elena D'Onghia. Phase wrapping of epicyclic perturbations in the wobbly galaxy. *Monthly Notices of the Royal Astronomical Society*, 454:933–945, 11 2015.

[11] E S Gadelmawla, M M Koura, T M A Maksoud, I M Elewa, and H H Soliman. Roughness parameters. *Journal of Materials Processing Technology*, 123:133–145, 2002.

[12] Spencer Brucks. Bruker atomic force microscope standard operating procedure.

[13] Shunsaku Horiuchi, Kohsuke Sumiyoshi, Ko Nakamura, Tobias Fischer, Alexander Summa, Tomoya Takiwaki, Hans-Thomas Janka, and Kei Kotake. Diffuse supernova neutrino background from extensive core-collapse simulations of 8-100 m progenitors. *Monthly Notices of the Royal Astronomical Society*, 1:1363–1374, 9 2018.

[14] Norman M D Brown and Zhi Hui Liu. The etching of natural alpha-recoil tracks in mica with an argon rf-plasma discharge and their imaging via atomic force microscopy. *Applied Surface Science*, 93:89–100, 1996.

[15] Sebastian Baum, William Derocco, Thomas D.P. Edwards, and Saarik Kalia. Galactic geology: Probing time-varying dark matter signals with paleodetectors. *Physical Review D*, 104, 12 2021.

[16] Sebastian Baum, Thomas D. P. Edwards, Katherine Freese, and Patrick Stengel. New projections for dark matter searches with paleo-detectors. *Instruments*, 5:21, 6 2021.

[17] Sebastian Baum, Patrick Stengel, Natsue Abe, Javier F. Acevedo, Gabriela R. Araujo, Yoshihiro Asahara, Frank Avignone, Levente Balogh, Laura Baudis, Yilda Boukhtouchen, Joseph Bramante, Pieter Alexander Breur, Lorenzo Caccianiga, Francesco Capozzi, Juan I. Collar, Reza Ebadi, Thomas Edwards, Klaus Eitel, Alexey Elykov, Rodney C. Ewing, Katherine Freese, Audrey Fung, Claudio Galelli, Ulrich A. Glasmacher, Arianna Gleason, Noriko Hasebe, Shigenobu Hirose, Shunsaku Horiuchi, Yasushi Hoshino, Patrick Huber, Yuki Ido, Yohei Igami, Yoshitaka Itow, Takenori Kato, Bradley J. Kavanagh, Yoji Kawamura, Shingo Kazama, Christopher J. Kenney, Ben Kilminster, Yui Kouketsu, Yukiko Kozaka, Noah A. Kurinsky, Matthew Leybourne, Thalles Lucas, William F. McDonough, Mason C. Marshall, Jose Maria Mateos, Anubhav Mathur, Katsuyoshi Michibayashi, Sharlotte Mkhonto, Kohta Murase, Tatsuhiro Naka, Kenji Oguni, Surjeet Rajendran, Hitoshi Sakane, Paola Sala, Kate Scholberg, Ingrida Semenec, Takuya Shiraishi, Joshua Spitz, Kai Sun, Katsuhiko Suzuki, Erwin H. Tanin, Aaron Vincent, Nikita Vladimirov, Ronald L. Walsworth, and Hiroko Watanabe. Mineral detection of neutrinos and dark matter. a whitepaper. 1 2023.

[18] A.K. Drukier, Ch. Cantor, and M. Chonofsky. New class of biological detectors for wimps. 2013.

[19] Andrzej K. Drukier, Sebastian Baum, Katherine Freese, Maciej Górski, and Patrick Stengel. Paleo-detectors: Searching for dark matter with ancient minerals. *Physical Review D*, 99, 2 2019.

[20] Thomas D.P. Edwards, Bradley J. Kavanagh, Christoph Weniger, Sebastian Baum, Andrzej K. Drukier, Katherine Freese, Maciej Górski, and Patrick Stengel. Digging for dark matter: Spectral analysis and discovery potential of paleo-detectors. *Physical Review D*, 99, 2 2019.

[21] B. W.H. Hendriks. *Analytical Methods: Fission Track Analysis*. Elsevier Inc., 1 2004.

[22] Airton Natanael Coelho Dias, Carlos Alberto Tello Saenz, Carlos José Leopoldo Constantino, Cleber José Soares, Felipe Ponciano Novaes, and Ana Maria Osório Araya Balan. Micro-raman spectroscopy and sem/edx applied to improve the zircon fission track method used for dating geological formations. *Journal of Raman Spectroscopy*, 40:101–106, 1 2009.

[23] L. Tommasino, G. Zapparoli, P. Spiezia, R. V. Griffith, and G. Espinosa. Different etching processes of damage track detectors for personnel neutron dosimetry. *Nuclear Tracks and Radiation Measurements (1982)*, 8:335–339, 1984.

[24] Michael L'Annunziata. *Handbook of Radioactivity Analysis*, volume 2. Academic Press, 4 edition, 2020.

[25] Hameed A Khan, Naeem A Khan, P O Nilore, and Reimar Spohr. Scanning electron microscope analysis of etch pits obtained in a muscovite mica track detector by etching in hydrofluoric acid and aqueous solutions of naoh and koh. *Nuclear Instruments and Methods*, 189:577–581, 1981.

[26] J D Macdougall. Fission-track dating. *Scientific American*, 235:114–123, 1976.

[27] Claire Ansberque, David M Chew, and Kerstin Drost. Apatite fission-track dating by la-q-icp-ms imaging. *Chemical Geology*, 2020.

[28] Pieter Vermeesch. Statistics for la-icp-ms based fission track dating. *Chemical Geology*, 456:19–27, 5 2017.

[29] Andrew J.W. Gleadow, David X. Belton, Barry P. Kohn, and Roderick W. Brown. *Fission track dating of phosphate minerals and the thermochronology of apatite*, volume 48. De Gruyter Mouton, 2 2019.

[30] P. B. Price and R. M. Walker. Fossil tracks of charged particles in mica and the age of minerals. *Journal of Geophysical Research*, 68:4847–4862, 8 1963.

[31] Shi-Lun Guo, Sheng-Fen Sun, Xiu-Hong Hao, Yong Luo, Yu-Hua Zhao, Yu-Lan Wang, Guoxiao Ren, Yinzao Zhou, Rongqing Zhou, and Zuoxiu He. Fission track dating of muscovite mica for searching for magnetic monopoles. *Nuclear Tracks and Radiation Measurements*, 15:703–705, 1988.

[32] S R Hashemi-Nezhad and S A Durrani. Registration of alpha-recoil tracks in mica: The prospects for alpha-recoil dating method. *Nucl. Tracks*, 5:189–205, 1981.

[33] Jason E. French and David F. Blake. Discovery of naturally etched fission tracks and alpha-recoil tracks in submarine glasses: Reevaluation of a putative biosignature for earth and mars. *International Journal of Geophysics*, 2016, 2016.

[34] E. G. Garrison, C. R. McGimsey, and O. H. Zinke. Alpha-recoil tracks in archeological ceramic dating. *Archaeometry*, 20:39–46, 1978.

[35] R Craig, E Mamidzhanian, and A W Wolfendale. Ancient cosmic ray tracks in mica? *PHYSICS LETTERS*, 26, 1968.

[36] D P Snowden-Ifft, E S Freeman, and P B Price. Limits on dark matter using ancient mica. *Physical Review Letters*, 74, 1994.

[37] Snowden-Ifft and Chan. A new track etch model for mica. *Nuclear Instruments and Methods*, 101:247–251, 1995.

[38] Weidong Li, Ryan Chornock, Jesse Leaman, Alexei V. Filippenko, Dovi Poznanski, Xiaofeng Wang, Mohan Ganeshalingam, and Filippo Mannucci. Nearby supernova rates from the lick observatory supernova search - iii. the rate-size relation, and the rates as a function of galaxy hubble type and colour. *Monthly Notices of the Royal Astronomical Society*, 412:1473–1507, 2011.

[39] Enrico Cappellaro, Roberto Barbon, and Massimo Turatto. Supernova statistics. 2003.

[40] Alessandro Strumia and Francesco Vissani. Neutrino masses and mixings and chapter 1. 2010.

[41] Gianfranco Bertone and Dan Hooper. History of dark matter. *Reviews of Modern Physics*, 90, 10 2018.

[42] Sebastian Baum, Andrzej K. Drukier, Katherine Freese, Maciej Górski, and Patrick Stengel. Searching for dark matter with paleo-detectors. *Physics Letters, Section B: Nuclear, Elementary Particle and High-Energy Physics*, 803, 4 2020.

[43] N. Soppera, M. Bossant, and E. Dupont. Janis 4: An improved version of the nea java-based nuclear data information system. *Nuclear Data Sheets*, 120:294–296, 2014.

[44] Brain J. Skinner. The system of mineralogy of james dwight dana and edward salisbury dana. *Science*, page 821, 3 1963.

[45] Ontario mineral inventory, 7 1981.

[46] Hugo K. Christenson and Neil H. Thomson. The nature of the air-cleaved mica surface. *Surface Science Reports*, 71:367–390, 6 2016.

[47] Hiroshi Sakuma and Shigeru Suehara. Interlayer bonding energy of layered minerals: Implication for the relationship with friction coefficient. *Journal of Geophysical Research: Solid Earth*, 120:2212–2219, 4 2015.

[48] Jin Ho Lee, Soo Jeong Park, and Jeong Woo Choi. Electrical property of graphene and its application to electrochemical biosensing. *Nanomaterials*, 9, 2 2019.

[49] M W Chaudhari. Inclusions in muscovite of iron oxides and hydroxides. *Lithos*, 3:295–305, 1970.

[50] A R Patel and S Ramanathan. Etching of mica cleavages. *Acta Crystallographica*, 15:860, 1962.

[51] Konstanze Stübner, Helmholtz-Zentrum Dresden-Rossendorf, Lothar Ratschbacher, and Raymond Jonckheere. The densities and dimensions of recoil-track etch pits in mica. *Chemical Geology*, 404:52–61, 2015.

[52] S. R. Hashemi-Nezhad. The geometry of etched heavy ion tracks in phlogopite mica; a clear dependence on energy deposited. *Nuclear Instruments and Methods in Physics Research, Section B: Beam Interactions with Materials and Atoms*, 234:533–547, 7 2005.

[53] M. Lang, U. A. Glasmacher, R. Neumann, and G. A. Wagner. Etching behaviour of alpha-recoil tracks in natural dark mica studied via artificial ion tracks. volume 209, pages 357–361, 8 2003.

[54] Perrin. Walker and William H. Tarn. *CRC handbook of metal etchants*. CRC Press, 1991.

[55] H. A. Khan. Etching characteristics of muscovite mica and feldspar crystalline track detectors. *Radiation Effects*, 32:49–53, 1977.

[56] Naeem Khan, H A Khan, N A Khan, K Jamil, and R Brandt. Annealing of heavy ion latent damage trails in muscovite mica and cr-39 plastic track detectors. *Nuclear Tracks and Radiation Measurements*, 8:377–380, 1984.

[57] Shawn D. Thornton. Reaction of sodium hydroxide with silicate minerals. 1986.

[58] M. Sugawara. *Plasma Etching: Fundamentals and Applications*. OUP Oxford, 5 1988.

[59] I. Horcas, R. Fernández, J. M. Gómez-Rodríguez, J. Colchero, J. Gómez-Herrero, and A. M. Baro. Wsxm: A software for scanning probe microscopy and a tool for nanotechnology. *Review of Scientific Instruments*, 78, 2007.

[60] David Nečas and Petr Klapetek. Gwyddion: An open-source software for spm data analysis. *Central European Journal of Physics*, 10:181–188, 2 2012.

[61] M. D. Rodriguez, W. X. Li, F. Chen, C. Trautmann, T. Bierschenk, B. Afra, D. Schauries, R. C. Ewing, S. T. Mudie, and P. Kluth. Saxs and tem investigation of ion tracks in neodymium-doped yttrium aluminium garnet. *Nuclear Instruments and Methods in Physics Research, Section B: Beam Interactions with Materials and Atoms*, 326:150–153, 5 2014.

[62] LearnOpenCV. Blob detection using opencv (python, c++).

[63] E. Freeman and D. Snowden-Ifft. A new technique to measure the etch rate of mica. *Nuclear Instruments and Methods*, 1995.

[64] P. B. Price and R. M. Walker. Chemical etching of charged-particle tracks in solids. *Journal of Applied Physics*, 33:3407–3412, 1962.

[65] S Guedes, J C Hadler, J E S Sarkis, K M G Oliveira, M H Kakazu, P J Iunes, M Saiki, C A Tello, and S R Paulo. Spontaneous-fission decay constant of 238 u measured by nuclear track techniques without neutron irradiation. *Journal of Radioanalytical and Nuclear Chemistry*, 258:117–122, 2003.

[66] Raymond Jonckheere. Alpha recoil track dating of mica. 2022.

[67] W H Huang and R M Walker. Fossil alpha-particle recoil tracks: a new method of age determination. *Science*, 155:1103, 3 1967.

[68] Robert L. Fleischer, P. Buford Price, and Walker Robert M. *Nuclear Tracks in Solids: Principles and Applications*. University of California Press, 1975.

[69] James F. Ziegler. Stopping range of ions in matter, 1983.

[70] Carlotta Giusti and Martin V. Ivanov. Neutral current neutrino-nucleus scattering: Theory. *Journal of Physics G: Nuclear and Particle Physics*, 47, 1 2020.

[71] Weidong Li, Ryan Chornock, Jesse Leaman, Alexei V. Filippenko, Dovi Poznanski, Xiaofeng Wang, Mohan Ganeshalingam, and Filippo Mannucci. Nearby supernova rates from the Lick Observatory Supernova Search – III. The rate–size relation, and the rates as a function of galaxy Hubble type and colour. *Monthly Notices of the Royal Astronomical Society*, 412(3):1473–1507, 04 2011.

[72] G. S. Dmitriev, L. N. Zanaveskin, T. E. Shorina, and M. N. Makhin. Isolation of chloride sodium from concentrated wastewater in chemical productions. *Russian Journal of Applied Chemistry*, 92:1239–1243, 9 2019.

[73] Miyi Li, Dana Constantinescu, Lisheng Wang, André Mohs, and Juürgen Gmehling. Solubilities of nacl, kcl, licl, and libr in methanol, ethanol, acetone, and mixed solvents and correlation using the liquac model. *Industrial and Engineering Chemistry Research*, 49:4981–4988, 5 2010.

[74] S. Mendelson. Dislocation etch pit formation in sodium chloride. *Journal of Applied Physics*, 32:1579–1583, 1961.

[75] Some typical observations on etch pits and the morphology of etched surfaces. In Keshra Sangwal, editor, *Etching of Crystals*, volume 15 of *Defects in Solids*, pages 265–301. Elsevier, 1987.

[76] K. C. Benison. Acid saline fluid inclusions: Examples from modern and permian extreme lake systems. *Geofluids*, 13:579–593, 11 2013.

[77] J. D. Livingston. Etch pits at dislocations in copper. *Journal of Applied Physics*, 31:1071–1076, 1960.

[78] Dongzhu Lu, Quantong Jiang, Xiumin Ma, Qichao Zhang, Xiaole Fu, and Liang Fan. Defect-related etch pits on crystals and their utilization. *Crystals*, 12:1549, 10 2022.

[79] J H Auld R I Garrod. Screw dislocations in mica. *Nature*, 169:580, 1952.

[80] Swarnal1 Ghosh, Atul Saxena, and K K Dwivedi. Channeling of 1.65 gev 132-xe in mica. *Nuclear Tracks and Radiation Measurements*, 15:349–352, 1988.

[81] Clemens Scheuner, Steffen Jankuhn, Jürgen Vogt, Sébastien Pezzagna, Christina Trautmann, and Jan Meijer. Nanometer collimation enhancement of ion beams using channeling effects in track-etched mica capillaries. *Scientific Reports*, 7, 12 2017.

[82] F M Russell. Rare cosmological events recorded in muscovite mica. 2019.

Appendix A

Standard Operating Procedures

In this appendix section you can find the standard operating procedures for all etching experiments and readout technologies used as part of this research.

A.1 Crystal Cleaving and Preparation for Etching

Before minerals are etched, a clean surface must be sought. Depending on the mechanical properties of the minerals, samples can be cleaved in different ways. The minerals we use are halite - or rock salt - which comes in a bulk cubic form, and micas, which are extremely brittle, layered minerals that come in sheets only a few millimeters thick. Our mica sheets are multiple inches in length and height, and you can use a clean pair of ordinary scissors to cut out a smaller section to use as a sample. Cleaving of minerals should always be done with gloves and clean equipment, with readily available sample containers and a good set of tweezers.

To cleave halite, you can use a razor blade and rock hammer. A razor blade is used to precisely determine where on the sample you want it to split. It is an efficient method of preferentially cleaving halite. Otherwise, using just a rock hammer, the crystal with naturally break on the crystal planes with the lowest potentially energy. The razor blade method is similar in concept to using a pick to split rocks or ice down a designated plane. To cleave samples of halite for this research, take a chunk of the crystal and put the razor blade directly on the surface where you want the mineral to split. Using a rock hammer (the blunt end), lightly tap the top of the razor blade and the crystal should cleave easily. If it doesn't cleave right away, re-tap the razor blade but with more force.

To cleave mica, you can use a variety of different methods including scotch tape or a razor blade. The low interlayer bonding energy of mica allows for a smooth and easy cleave between sheets. If you are only interested in analyzing one cleave of mica, scotch tape is the most efficient method. The ability for the tape adhesive to grab almost the entire back surface of the sheet creates a much cleaner cleave (verified through many experiments). To cleave mica with scotch tape, lay the cut sample on a clean surface, and add enough pieces of tape to the sample so that the tape covers the entire back of the sample with tape hanging off the edge to be able to pull up. Then, grabbing the excessive tape, gently and slowly peel the mica layers off one another. To ensure that a

Supplies and Personal Protective Equipment for Ferric Chloride and Glacial Acetic Acid Etch
Scale, scoop
Fume hood
Tweezers
Sample containers
Parafilm
Beaker(s)
Pure acetone or isopropanol
Ferric Chloride powder
Glacial Acetic Acid
Gloves
Goggles
Close-toed shoes

Table A.1: Etching supplies and personal protective equipment for chemically etching halite with ferric chloride and glacial acetic acid.

whole layer was removed, and did not leave big flakes or pieces behind, you can look at the material still stuck on the tape and it will be obvious if there are holes.

To cleave mica with a razor blade, align the blade on the side of atomic sheets (normal to the surface) and find a weak point of split. These layers are extremely brittle, thus layers can naturally start to come apart and it is easiest to follow these routes. Align the razor blade between to sections of sheets and slowly cut down into the sample about $\frac{1}{4}$". Once samples are separately on one end, take a pair of tweezers and grab onto one section of sheets, using a finger and the blade to hold down the other, and slowly peel back the chunk of layers. Sometimes this process results in uneven cleaves, where a sheet of mica might flake or split into pieces while cleaving, If this is the case, re-do the cleave until a smooth surface is revealed.

A.2 Ferric Chloride and Glacial Acetic Acid Etch of Halite

A solution of ferric chloride and glacial acetic acid can be used to chemically etch halite [54]. To handle these chemicals, normal latex gloves can be used, along with safety goggles, a lab coat, and closed toed shoes. The solution does not have to be made under a fume hood, but it is also a good idea to designate a clean space.

A ratio of 4g of ferric chloride powder, to 1 liter of glacial acetic acid is used. Ferric chloride powder will quickly dissolve with moisture in the atmosphere, so anytime ferric chloride powder is removed from the canister, one must operate quickly. A fume hood might help with the quickly dissolving ferric chloride powder. The required equipment includes beakers for solution making, a scale to weigh the ferric

chloride powder, sample container(s), tweezers, and the proper PPE. Our glacial acetic acid came in three separate 1.5 mL containers, and due to the small size of our halite samples, we modified the ratio of ferric chloride to meet the 1.5 mL of glacial acetic acid.

Take the following steps to prepare the solution and etch samples of halite:

1. Put on the proper personal protection equipment, including gloves, goggles, a lab coat, and close-toed shoes.

2. Designate a clean lab space, under a fume hood if accessible, and wash all sample containers, tweezers, and beakers with pure acetone or isopropanol. Prepare a beaker of *pure* acetone or isopropanol to rinse samples in after etching.

3. Using a scale, weigh out the necessary amount of ferric chloride powder, following the 4g:1L ratio by Ref. [54]. If using a bulk container of glacial acetic acid, measure the necessary amount of acid in a graduated cylinder or beaker.

4. Combine the ferric chloride power and glacial acetic acid, while gently swirling the beaker to mix the solution. The ferric chloride will easily dissolve and the solution should become amber-brown in color.

5. Using a prepared sample of halite, drop the sample gently into the solution - taking into account what side of the sample is freshly cleaved - and agitate the beaker containing the sample and solution softly by swirling the beaker until the the etching time is finished.

6. Remove the sample with tweezers and gently drop into the beaker of acetone or isopropanol, and rinse, while agitating, for approximately 30 seconds.

7. Remove the sample with clean tweezers and let the sample dry on a clean surface, preferable a rack to dry both sides of the sample efficiently. Once dry, secure in a clean container.

The etching time of halite in this solution can vary based on the sought results. A time as little as 15 seconds can be used to reveal tracks. We used a range of times, from 15 seconds to 2 minutes. To either match tracks together or determine the efficiency of etching, an etched or unetched matching cleave of the sample can be used. It is always a good idea to determine the amount of surface roughness of samples after etching to determine the best readout technology, as the AFM is not suitable for rough surfaces (on the order of microns).

Supplies and Personal Protective Equipment for Sodium Hydroxide Etch
Scale, scoop
Fume hood
Thermometer x2
Magnetic stirrer and hot plate
Tweezers x2
Water bath
Sample containers
Parafilm
Beakers with lids
Pure acetone or isopropanol
NaOH pellets
Deionized water
Gloves
Goggles
Close-toed shoes

Table A.2: Etching supplies and personal protective equipment for chemically etching mica with aqueous NaOH solution.

A.3 Sodium Hydroxide Etch of Muscovite Mica

Muscovite mica can be etched while an aqueous solution of sodium hydroxide. The solution, 6N to be exact, needs to be kept heated throughout the experiment. Our 6N aqueous NaOH solution, experimentally, equation to approximately 11.964 grams of NaOH pellets and 50 mL of deionized water. In addition, the beakers should be lidded to prevent evaporate of water, which will result in the precipitation of NaOH in the solution. The supplies and PPE for this experiment are listed in Table A.2.

The chemical reaction of NaOH with water is highly exothermic, therefore it is very important to keep the solution agitated when mixing to prevent hot spots. A thermometer can be placed in the solution while dissolving to monitor the temperature and determine when it reaches room temperature again. The maximum temperature detected in our experiments when mixing NaOH and water was 59 °C. In addition to keeping the solution agitated, only 80% of the water needed for the solution should be initially added with the NaOH. Once that first solution reaches room temperature, then the additional 20% of water can be added, still keeping the solution agitated. Once the final solution reaches room temperature, it can be heated again to the desired etching temperature. Samples of mica can be cleaned with deionized water in a water bath, which will agitate the water allowing a greater cleanliness to be achieved.

To etch samples of mica with sodium hydroxide, follow the steps below:

1. Put on the proper personal protection equipment, including gloves, goggles, a lab coat, and close-toed shoes.
2. Designate a clean lab space, under a fume hood if accessible, and wash all sample containers, tweezers, and beakers with pure acetone or isopropanol.
3. Fill a water bath with deionized water and heat to the desired etching temperature.
4. Prepare an ultrasonic water bath full of deionized water to clean the samples afterwards.
5. Using a scale, measure the necessary amount of sodium hydroxide pellets. Put the pellets in a cleaner beaker along with the magnetic stirrer bit, and place onto a stirrer platform.
6. In a separate graduated cylinder or beaker, measure **80%** of the necessary amount of deionized water. Put the remaining **20%** in a separate beaker for later.
7. Turn on the magnetic stirrer at a slow setting, and slowly add 80% of the water. Monitor the temperature with a thermometer, and wait until the solution peaks and reaches room temperature again, keeping the stirrer going.
8. Once the solution has reached room temperature, add in the remaining 20% of water and wait until the final solution reaches room temperature.
9. Transfer the beaker(s) to a water bath heated at the desired temperature of etching, and keep a lid on the beakers.
10. Check the temperature periodically with a thermometer and once the solution has reached the temperature of the water bath, drop in a sample of freshly cleaved mica and wait for the desired etching time.
11. Remove samples of mica with tweezers and immediately place in the ultrasonic water bath for approximately one minute. Remove with clean tweezers when done and place on a rack for drying.
12. Once dry, store sample in a clean container.

A.4 Plasma Etching: Diener Pico Plasma Cleaner

The steps to operate and initiate a plasma etching process with the Diener Pico plasma cleaner are as follows:

1. After preparing your sample for etching, load into the chamber while wearing gloves. There is no pump down needed before this.

2. Turn on the Controller. Only use the appropriate stylus provided with the touch screen interface. There will be a loud switch coming from the mechanical pump turning on and getting ready for the pump down process.

3. Locate the Program tab, and navigate to the Plasma Process subsection. Here is where you can manually input the designated power and etching time. In the gas flow sections, you can manipulate the flow rate and process gases used. Click save when the recipe is completed. Take note of what program number you are on.

4. Navigate back to the home interface, and if needed, set the designated pressure of the plasma run. The default is 0.2 mbar. Ensure that the program number selected is the proper recipe.

5. Open the gas valves for argon, oxygen, and/or CF_4. There are two valves - ensure they are both open.

6. Click the program Start, and ensure that recipes are correct, following prompts on the screen. Once the plasma process begins, there will be a very loud motor noise coming from the mechanical pump initiating the pump down process to reach vacuum.

7. Log plasma cleaner session in the log book accompanying the equipment. Reach out to Dr. Daniel Santavicca with any issues, concerns, or help with the equipment.

The plasma cleaning/etching process is a relatively simple interface to operate, and will clearly show on the home screen the real time measurements of pressure, gas flow, power, time elapsed, and any other parameter a user could be interested in monitoring. It's important to log any abnormal behaviors during the etching time in the log book. The plasma process has multiple steps: a pump down (to reach vacuum), a gas supply period (to reach designated pressure with gas of choice), a plasma process period (when plasma is sparked and etching/cleaning the samples in chamber), a purging session (to release gas in chamber), and a venting session (to reach atmospheric pressure). For now, the venting session uses the air within Lab 1522, rather than pure oxygen. This is important to note, in case contamination on the surface of samples needs to be precisely avoided.

When a plasma run is completed, take the following steps to finish a session:

1. Turn off the Controller. This will turn off the mechanical pump.

2. Close both gas valves, on all tanks used.

3. Wearing gloves, remove the sample(s) with tweezers and place in a designated container.

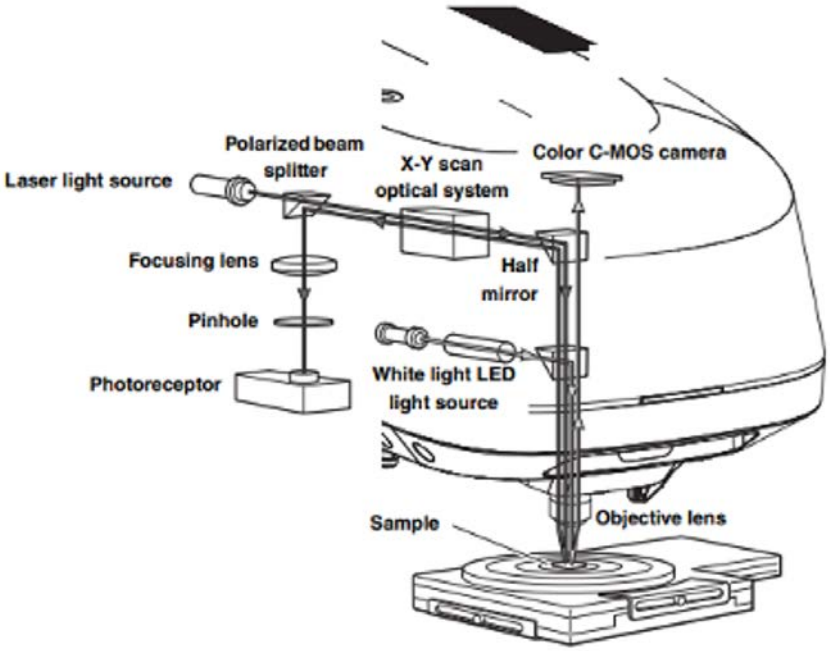

Fig. A.1: Schematic diagram of the Keyence VK-X1000 laser confocal microscope, from the Keyence manual [7].

4. If a recipe was changed, reset it back to the original parameters in place before the etching.

5. Log any last minute items in log book.

A.5 Keyence VK-X1000 Laser Confocal Microscope

The Keyence VK-X1000 is located at the Materials Science and Engineering Facility at UNF. It is a powerful laser confocal microscope with a maximum magnification of 150x, and the capability to retrieve height information using the intensity of reflected light from a laser. It also has a color camera for purely optical imaging. A schematic diagram of the Keyence VK-X1000 microscope setup can be seen in Figure A.1. The Keyence is capable of capturing an optical image (color) and laser image (black and white based on intensity). In addition, a composite optical+laser image can be rendered, as well as a depth map based on height data, and a C-Laser DIC image. The C-Laser image is a Differential Interference Contrast (DIC) imaging method that makes it much easier to visualize edges, bumps, or scratches on the surface [7]. It can enhance the contrast of laser images using the basis of interferometry. More information on the microscope specifications will be discussed in the next section.

To initiate a session on the Keyence VK-X1000, follow the steps listed below:

1. Manually drop the sample stage by moving the outermost wheel on the right of the microscope clockwise. Load sample onto stage, careful not to touch or disrupt the lens.

2. Turn on the monitor and microscope (power button is on the right upper side).

3. Log starting time in log book.

4. Open the VK Viewer software. This is how to control the microscope. Click 'reset XY position', ensuring the stage has been lowered to avoid a lens collision. The microscope will then realign itself.

5. The sample will be out of focus. Manually move the lens up using the outermost wheels on the right of the microscope, watching both the sample stage and the monitor screen as the sample approached the lens. Move the sample up to the lens with the outermost wheel until just barely in focus on the monitor display. Then use the software to reach a more exact focus onto the sample surface.

6. Register a navigation image to have an overall sample map to record and conserve coordinate positions with.

In our studies, focusing with the laser is done manually. The initial focus on the sample is done with the optical system and C-MOS camera. There is an Autofocus command that works efficiently but for the sake of measurement control, we opted to focus ourselves. A manual focus is done by manually moving the sample closer and farther from the lens, causing the intensity of light from the laser to decrease as you get farther from focus. Once no scattered light is detected from the laser on the photoreceptor, you set an upper or lower *limit* at that point. The distance between the upper and lower limits is the distance in Z the laser will focus on, at a certain pitch (discussed more in the next section).

During imaging, you might find that switching between lens causes your sample to be extremely out of focus, or there might be artifacts present in multiple images at a certain magnification. If this is the case, it's likely that there is something unaligned in the microscope. The technicians at MSERF will realign the microscope depending on the symptoms experienced. Any issues should be directly reported to MSERF faculty.

To conclude a session on the Keyence VK-X1000:

1. Switch to the lowest magnification, and save all remaining data.

2. Close the viewer software and turn off the microscope.

3. Manually lower the stage using the outermost wheel on the right side of the microscope, and remove and store the sample(s) with tweezers and gloves, carefully avoiding the lens.

4. Record end time in log book.

5. Transfer all collected data to a flash drive.

The data collected with the Keyence will be stored as .vk4 or .vk6 files, which are direct imports into the Multi-File Analyzer software designed for the Keyence. This software has the capability of visualizing, processing, and analyzing data. For our research, there were cases where individual tracks needed to be directly measured. This was done with the Multi-Analyzer software. However, any image processing such as plane subtraction (flattening), Fourier transforms, and smoothing was done separately in Python, in the Automatic Track Detection Code discussed in Section 3.3.

A.5.1 Laser Specifications

The laser on the Keyence VK-X1000, specifically a blue laser with a wavelength of 404 nanometers, raster scans across the sample surface, collecting a single peak intensity of reflected light at every pixel with a photoreceptor [7]. This peak intensity will occur when the lens and surface of the sample are exactly the working distance apart. Thus a shift in the intensity will directly relate to a change in Z. A diagram of this peak intensity measured is in Figure A.2. The contrast (intensity compared to neighbors) is graphed, yielding an intensity or height value for each pixel, creating a shape and roughness measurement of the surface. The laser will scan from left to right (x-direction) for a total number of rows, depending on the user-set pixel size. The maximum amount of pixels an image can have is 2048 x 1536 - any pixel size below that will average data across multiple pixels.

The spot size (beam width) of the laser is 0.4 μm, corresponding to its 404 nm wavelength. The microscope is accurate at measuring defects much larger in width than the width of the laser beam, but limited in accurately detecting defects that have widths close to or less than the beam width. The 50x magnification lens can achieve a maximum resolution of 139 nm/pixel in XY with a standard of 278 nm/pixel, whereas the 150x magnification lens (the lens used for all track measurement) can achieve a maximum resolution of 45.5 nm/pixel with a standard of 91 nm/pixel. The pitch, or distance between focal planes measured in Z (the distance between the sample and the lens), varies per image, per magnification. The average pitch for 50x magnification images is 0.10 μm whereas the average pitch in 150x magnification images is 0.08 μm. A smaller pitch, if keeping the Z-distance the same, will yield higher resolution in Z.

A.6 Atomic Force Microscope

In our research we use the Bruker Dimension 5 atomic force microscope supplied by the physics department at UNF (diagram in Figure A.3). We use amplitude modulation AFM in our imaging. Amplitude modulation AFM (AM-AFM, ”tapping” or contact

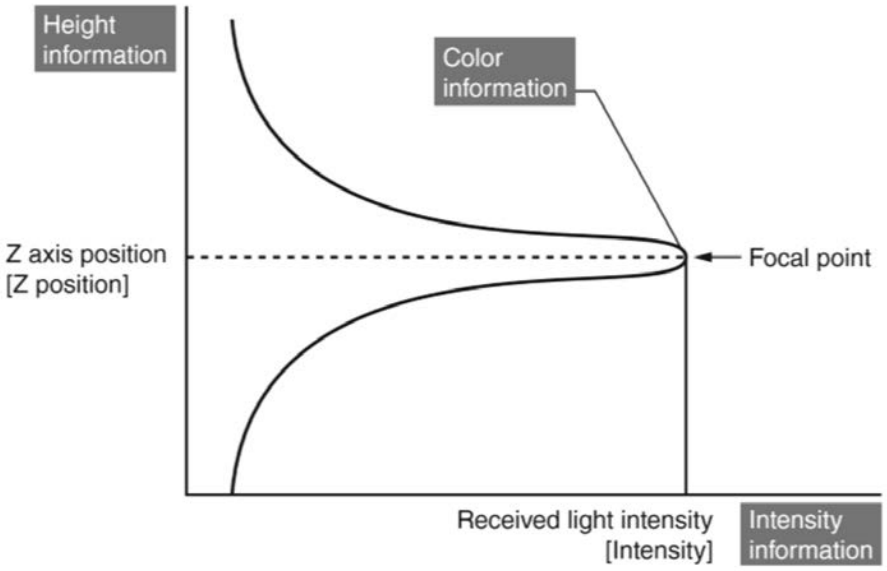

Fig. A.2: Schematic diagram of the peak intensity measured by the photoreceptor in the Keyence VK-X1000, from the Keyence manual [7].

mode) is a dynamic force microscopy mode where a cantilever-tip (probe) ensemble is excited at a fixed frequency, usually near or at the free resonance frequency [9]. The oscillation amplitude of the probe is used as a feedback parameter to map the sample topography [9]. The probe of an AFM is constructed from a flexible cantilever and a sharp tip (Fig. A.4) with a laser focused on top of the cantilever. [9]. The van der Waals forces between the sample surface and the probe of an AFM will change the oscillation of the cantilever, causing a deflection of the laser, which in turn correlates to a change in topography (Appendix Section B, Figure B.10).

The AFM has five main components to the system: the actual AFM (schematic diagram in Figure A.3), the controller, the air compressor, the oscilloscope, and the laser cooler. The controller controls the vacuum, air supply, and optics illumination [8]. Gauges on the controller will indicate vacuum and positive pressures - a schematic diagram of the controller can be seen in Appendix Section B, Figure B.9. The air compressor creates the suction/vacuum. The oscilloscope allows the user to read the real time amplitude of the cantilever. The laser cooler minimizes heat produced by the laser.

An AFM can reach atomic resolution, and thus its role as a paleo-detector readout technology is quite sufficient in the sense of track resolution [9, 17]. However, the AFM is not a high throughput tool, making it very inefficient at measuring surface area on the order of cm^2. In addition, the use of the AFM is limited depending on the sample properties, one of the most important being roughness. In our studies, there have been samples we could not image with the AFM due to the roughness after chemical or

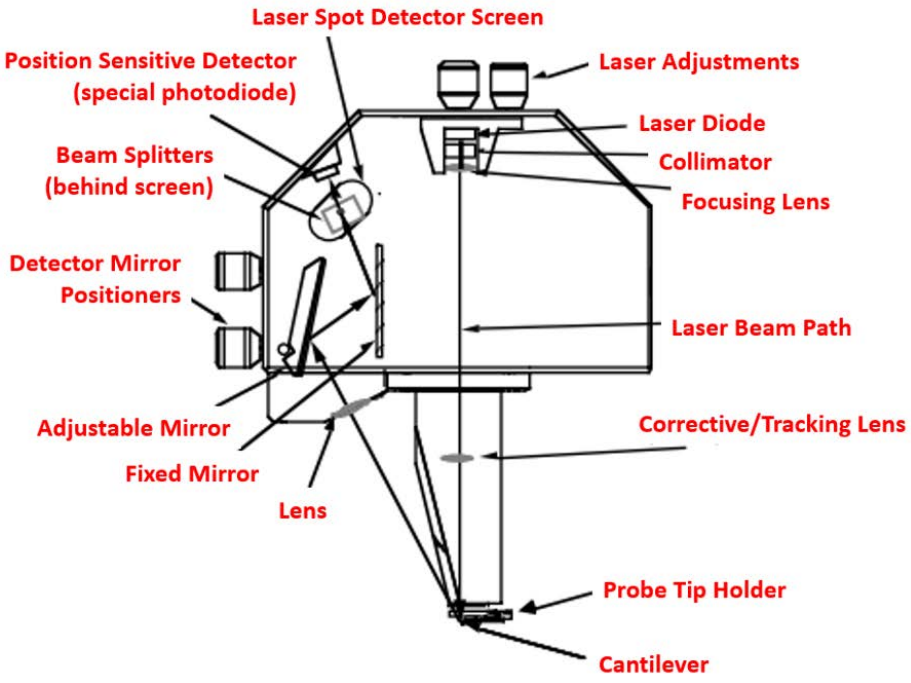

Fig. A.3: Schematic diagram of a Bruker Dimension 5 with Nanoscope 5 atomic force microscope (head), from Reference [8].

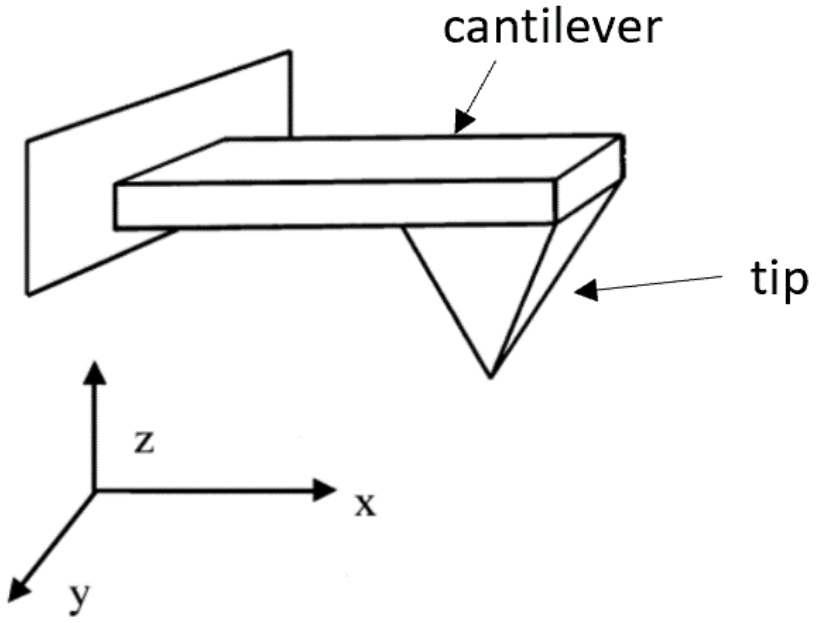

Fig. A.4: Diagram of a cantilever-tip (probe) setup from Ref. [9]. Probe will oscillate in the z-direction.

kinetic etching. For unetched sample characterization the AFM serves as an efficient measurement tools for surface roughness and atomic step analysis.

To initiate a session of the AFM, follow the steps below:

1. Turn on the controller, air compressor, oscilloscope, and computer monitors (in that order). Open the '7.30 Nanoscope' software. Turn off the laser cooler in the back of the room. The system will need approximately 45-60 minutes to warm up and reach a resonance RMS amplitude (the amplitude of the tip oscillating in free space).

2. Move the stage away from the head of the AFM and insert sample. There is a small amount of suction coming from the center hole that should hold down small samples, avoiding shift during imaging. If this suction is not holding down the sample, use a small glue pad. Carefully move the stage back to where the sample is under the head.

3. Align the laser onto the cantilever by manually moving the head. The laser is aligned when a red reflected light is seen in the small laser window (Figure B.8).

4. Bring the sample into focus, slowly, using the camera and manual controls. It is best to focus on the edge of a sample first. Record coordinates of edges to preserve image locations.

5. Set the offsets to zero, and determine an image size of the scan.

6. Once sample is in focus, engage the probe to see if the sample is within range. The piezoelectric quartz with automatically regulate the distance between the tip and sample based on the amplitude feedback.

7. If the sample is in range, the probe will starting scanning immediately, tracing and retracing every line on a given image area, rendering an image in the software window.

8. Adjust the amplitude set point as necessary to bring the trace and re-trace signal lines together such that they are equal and noise is at a minimum.

9. Render an image by selecting 'Capture'. It is also best to start the scanning again from either the top or bottom to minimize the noise that originates at the beginning of the scan.

10. Images will automatically save in the 'CAPTURE' folder.

11. To image at another location you can either set the X and/or Y offsets (if the distance is within +/- 40 μm) or disengage the probe and use the navigation pane to move in the X and Y direction.

AFM images have three separate data files: topography, phase (phase lag from the drive), and error (the difference between the amplitude and the set point at each point in the scan). The error and phase files map the measured values across each scan, corresponding directly with each location on the topography map. For measurement and image processing, the topography image is always used. Flattening almost always must occur before any processing as the AFM will average the plane across each linear scan. This results in facets (like step faces) to be tilted and untrue to their actual orientation. You can flatten images in MATLAB, Gwyddion, or WSxM [59, 60].

To end a session on the AFM:

1. Disengage the sample *twice* (at least). Manually move the stage down within a safe distance (a few centimeters below the head), and move it away from the head to safely remove it.

2. Reset all parameters to original values.

3. Turn off the controller, air compressor, oscilloscope, and initiate the laser cooler.

4. Save all data on a flash drive.

5. Close the software and turn off computer monitors.

Appendix B

Additional Figures

In this appendix section you can find additional figures collected as part of this research.

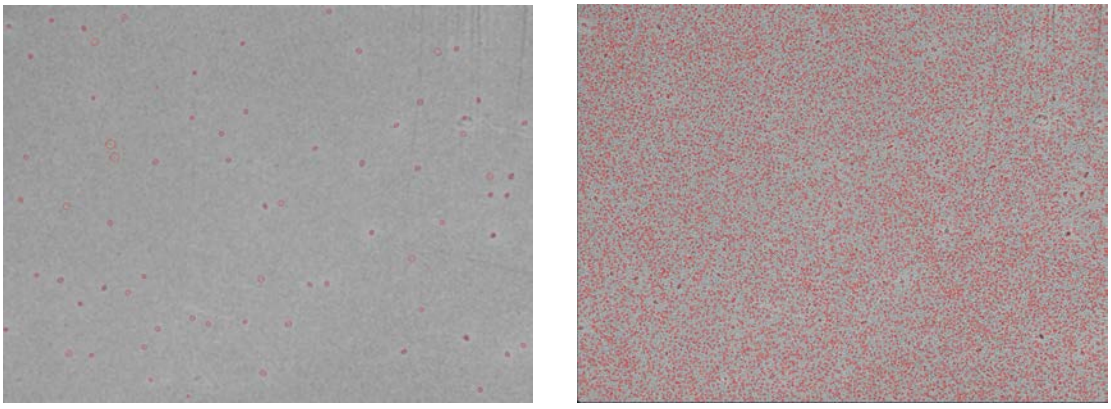

(a) **(b)**

Fig. B.1: (a) Laser image of halite with a Gaussian blur applied, and automatically detected nuclear recoil tracks circled in red and (b) the same laser image of halite without a Gaussian blur applied, with hundreds of incorrectly detected pits circled in red. All code parameters besides the Gaussian blur were kept constant. The code can be found on GitHub.

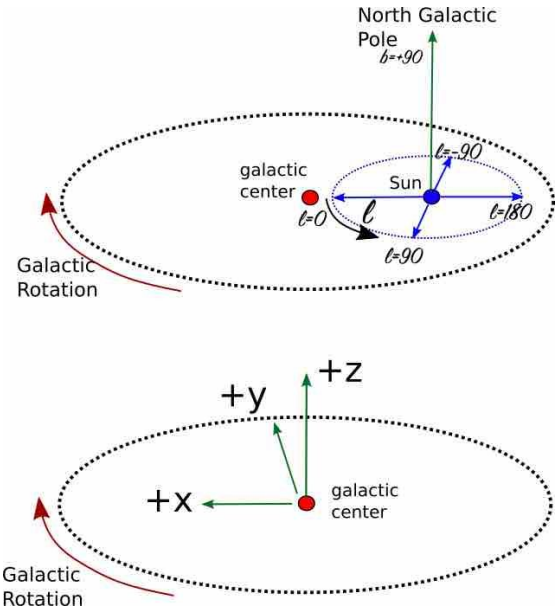

Fig. B.2: Schematic diagram of the position of the Sun with respect to the galactocentric radius of the Milky Way, from Reference [10]. *l* is the angular rotation of the Sun with respect to the center.

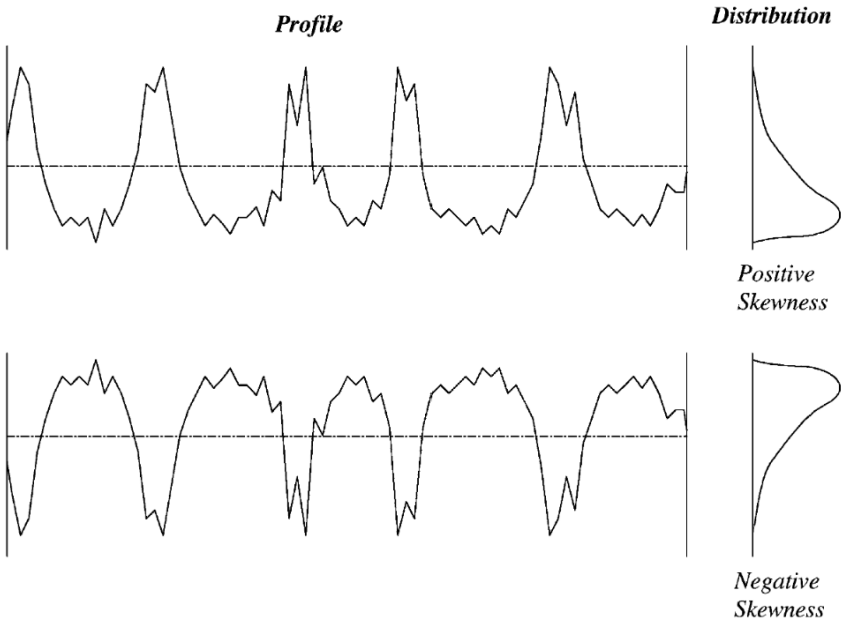

Fig. B.3: Definition of skewness and amplitude distribution curve by Ref. [11].

Fig. B.4: Laser image of argon plasma etched halite showing cubic and rectangular pits and/or fluid inclusions. Imaged with the Keyence VK-X1000 at MSERF at a magnification of 150x.

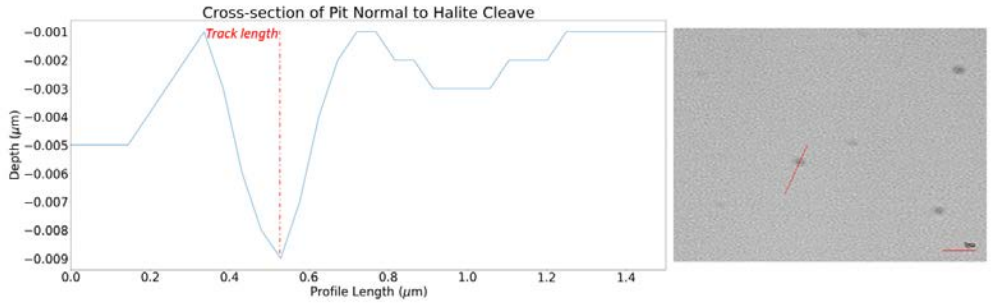

Fig. B.5: Profile and map of nuclear recoil track pit lying normal to the cleave plane of halite. Sample of halite was etched with argon plasma at 100 W/0.2 mbar/10 minutes.

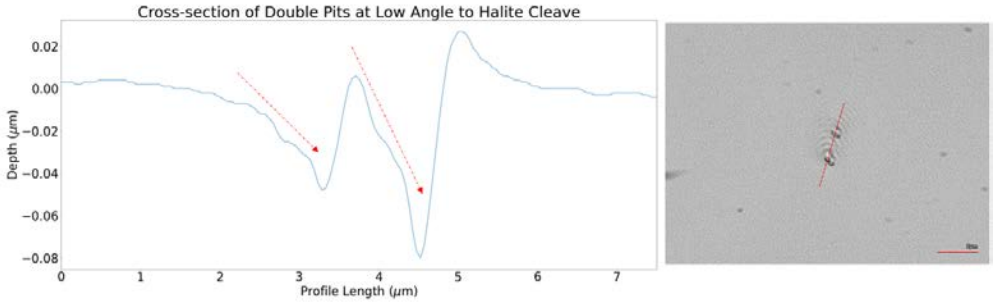

Fig. B.6: Profile and map of two nuclear recoil track pits lying at an angle to the cleave plane of halite. Sample of halite was etched with argon plasma at 100 W/0.2 mbar/10 minutes.

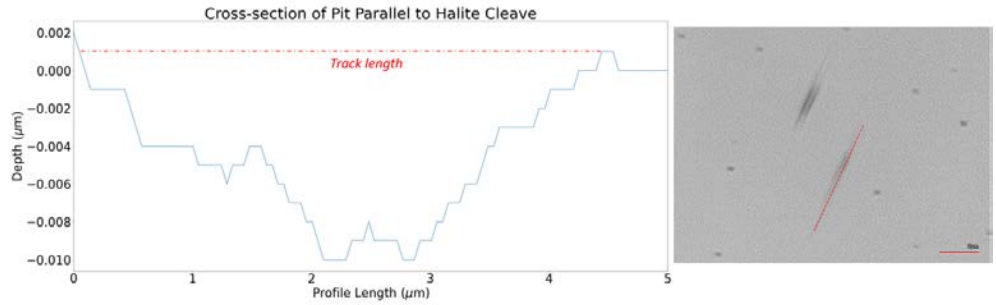

Fig. B.7: Profile and map of a nuclear recoil track pit lying in the cleave plane of halite. Sample of halite was etched with argon plasma at 100 W/0.2 mbar/10 minutes.

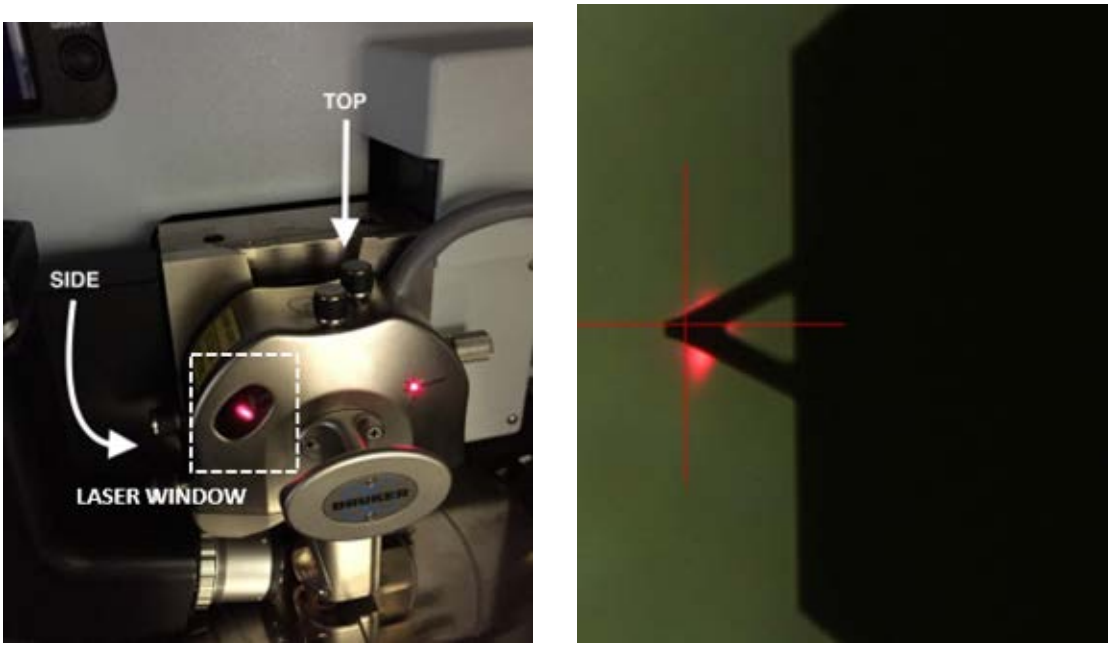

(a) **(b)**

Fig. B.8: (a) Reflected laser light shining through window on a Bruker AFM and (b) the aligned laser shining on top of the cantilever in optical view. Images are from Reference [12].

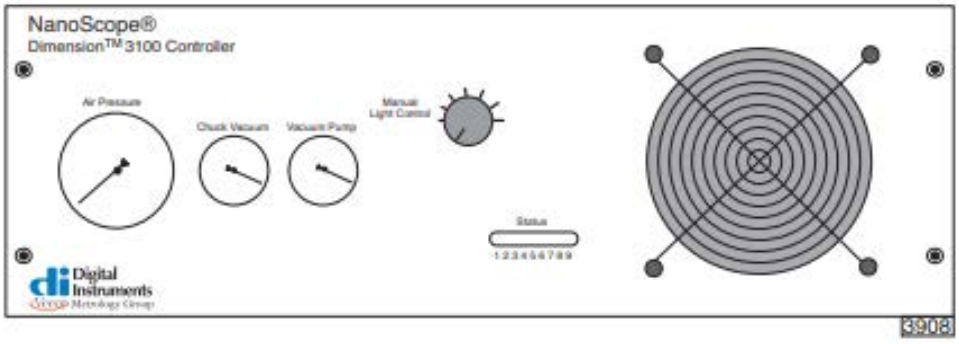

Fig. B.9: Schematic diagram of the AFM controller from the Bruker series manual [8].

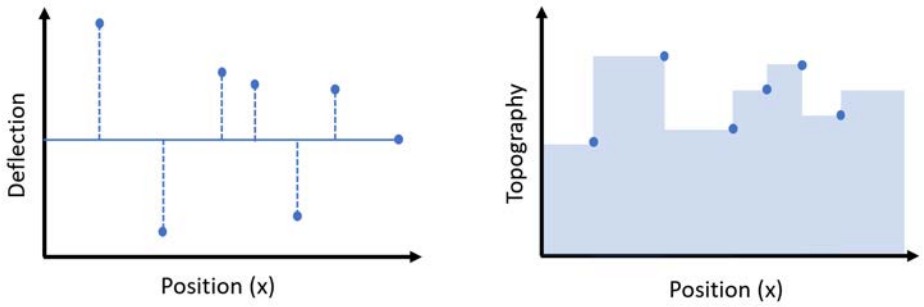

Fig. B.10: Graphs of (left) deflection of the laser versus position, and (right) topography of a corresponding surface over the same position.